Physical mechanisms of nutrient supply and controlling factors of phytoplankton growth in the Arafura Sea

Dissertation

with the aim of achieving a doctoral degree
at the Faculty of Mathematics, Informatics and Natural Sciences
Department of Earth Sciences
of Universität Hamburg

submitted by
Suliskania Nurfitri
from Bandung, Indonesia

Hamburg, 2021

Printed and/or published with the support of the German Academic Exchange Service

Accepted as Dissertation at the Department of Earth Sciences of the MIN Faculty

Day of oral defense:	14.12.2021
Reviewers:	PD Dr. Thomas Pohlmann Dr. Johannes Pätsch
Members of the Examination Commission:	Chair PD Dr. Thomas Pohlmann Depute chair Prof. Dr. Dirk Notz Prof. Dr. Corinna Schrum Prof. Dr. Gerhard Schmiedl Dr. Johannes Pätsch
Chair of the Subject Doctoral Committee Earth System Sciences:	Prof. Dr. Dirk Gajewski
Dean of the MIN Faculty:	Prof. Dr. Heinrich Graener

Abstract

The Arafura Sea is a relatively shallow basin (< 200 m deep) located in the eastern part of the Indonesian archipelago. Its border on the west is a deeper basin, the Banda Sea, with an average depth of ∼5000 m. Previous studies have shown that circulation in this particular region is mainly influenced by monsoonal winds, which are the northwest (NW) and southeast (SE) monsoons. In addition, previous studies have shown that upwelling is a characteristic phenomenon in this region, induced by the SE monsoon from June to August. During this period, the lower sea surface temperature and elevated chlorophyll-a concentrations are observed near the coast of Papua (northern Arafura Sea). Recent studies have suggested that these features are due to the upwelling of cold and nutrient-rich water masses originating from deeper layers of the Banda Sea.

The present study aims to investigate the mechanism of nutrient supply and its implication on phytoplankton distribution in further detail using a numerical model. A three-dimensional (3D) biogeochemical model ECOHAM (ECOsystem model HAMburg) is utilized in this study. The model domain extends from 122°–139°20' E and 1°48'–14°19' S, covering the Arafura and the Banda Sea regions. ECOHAM is forced by ocean current fields derived from HAMSOM (HAMburg Shelf Ocean Model), river run-off, atmospheric nitrogen deposition, wind stress, and solar radiation. Moreover, the initial and boundary values of biogeochemical variables are derived from WOA and GCOMS. Finally, the model results are validated against the in-situ nutrient measurements and satellite-derived chlorophyll-a concentration.

The simulated nutrient (i.e., nitrate and phosphate) concentrations show a good fit with observations, especially in the upper 200 m. Besides nutrients, the simulation overestimates surface chlorophyll-a concentrations in the northern Arafura Sea, but it still represents the seasonal variation quite well. Furthermore, the sensitivity test reveals that a 10% change in temperature factor Q_{10} for phytoplankton can significantly changes the Redfield net primary production by up to 25%.

This modeling study suggests a different mechanism of nutrient supply between the shallow region in the northern part (Sahul Shelf) and the continental slope area of the Arafura Sea. In the Sahul Shelf, nitrate is primarily transported to the near-surface layer via vertical mixing, which is stronger during the SE monsoon, compared to the NW monsoon. On the other hand, nitrate supply in the continental slope area is mainly regulated by advection. During the NW monsoon, the simulation reveals the horizontal intrusion of nitrate-rich water masses from the eastern Banda Sea in

the layer above the nitracline (a layer in which the nitrate concentration increases rapidly with increasing depth). By contrast, during the SE monsoon, the vertical advection transports nitrate to the layer above the nitracline, which is confirmed by nitrate budget analysis.

Furthermore, this study shows that phytoplankton growth is mainly regulated by nitrogen availability. In the Sahul Shelf, the seasonal variations of phytoplankton production and zooplankton grazing indicate the bottom-up control in June-August and top-down control in October-December in the zooplankton-phytoplankton system. In the continental slope area, nitrate concentration in the near-surface layer is depleted, suggesting a strong nitrate limitation, especially for diatoms. In this region, non-diatom production is higher than for diatom because non-diatoms take up ammonium more effectively.

Zusammenfassung

Das Arafura-Meer ist ein relativ flaches Meer (< 200 m tief) im östlichen Teil des indonesischen Archipels. Seine westliche Grenze ist die tiefere Bandasee mit einer durchschnittlichen Tiefe von ∼5000 m. Frühere Studien haben gezeigt, dass die Zirkulation in dieser speziellen Region hauptsächlich durch Monsunwinde beeinflusst wird. Diese sind der Nordwest-(NW) und Südostmonsun (SO). Darüber hinaus haben bisherige Studien gezeigt, dass Auftrieb ein charakteristisches Phänomen in dieser Region ist. Ausgelöst wird der Auftrieb durch den Südostmonsun von Juni bis August. Während dieser Zeit werden eine niedrigere Meeresoberflächentemperatur und erhöhte Chlorophyll-a-Konzentrationen nahe der Küste von Papua (nördliches Arafura-Meer) beobachtet. Neuere Studien haben gezeigt, dass diese Merkmale auf das Aufsteigen von kalten und nährstoffreichen Wassermassen zurückzuführen sind, die aus tieferen Schichten der Bandasee stammen.

Ziel der vorliegenden Studie ist es, den Mechanismus der Nährstoffversorgung und seine Auswirkungen auf die Phytoplanktonverteilung mit Hilfe eines numerischen Modells näher zu untersuchen. In dieser Studie wird ein dreidimensionales (3D) biogeochemisches Modell ECOHAM (ECOsystem model HAMburg) verwendet. Die Modelldomäne erstreckt sich von 122°–139°20' E and 1°48'–14°19' S, und deckt die Regionen Arafura- und Bandasee ab. ECOHAM wird durch Meeresströmungsfelder vorangetrieben, die aus HAMSOM (HAMburg Shelf Ocean Model), Fließgewässereintrag, atmosphärischer Stickstoffdeposition, Windeinfluss und Sonnenstrahlung abgeleitet wurden. Darüber hinaus werden die Anfangs- und Grenzwerte biogeochemischer Variablen aus WOA und GCOMS abgeleitet. Abschließend werden die Modellergebnisse gegen die in-situ-Nährstoffmessungen und satellitengestützten Chlorophyll-a-Konzentration validiert.

Die simulierten Nährstoffe (Nitrat und Phosphat) stimmen insbesondere in den oberen 200 m gut mit den Beobachtungen überein. Neben den Nährstoffen überschätzt die Simulation die Chlorophyll-a-Konzentrationen an der Oberfläche im nördlichen Arafura-Meer, dennoch bildet sie die jahreszeitlichen Schwankungen immer noch recht gut ab. Darüber hinaus zeigt der Sensitivitätstest, dass eine 10%ige Änderung des Temperaturfaktors Q_{10} für Phytoplankton die Nettoprimärproduktion von Redfield um bis zu 25% signifikant verändern kann.

Diese Modellierungsstudie legt einen anderen Mechanismus der Nährstoffversorgung zwischen der flachen Region im nördlichen Teil (Sahul-Schelf) und dem kontinentalen Hangbereich des Arafura-Meeres nahe. Im Sahul-Schelf wird

Nitrat hauptsächlich durch vertikale Vermischung in die oberflächennahe Schicht transportiert. Die vertikale Vermischung ist während des SO-Monsuns stärker als beim NW-Monsun. Andererseits wird die Nitratversorgung im Kontinentalhangbereich hauptsächlich durch Advektion reguliert. Während des NW-Monsuns zeigt die Simulation das horizontale Eindringen nitratreicher Wassermassen aus der östlichen Bandasee in die Schicht über der Nitraklin (eine Schicht, in der die Nitratkonzentration mit zunehmender Tiefe schnell ansteigt). Im Gegensatz dazu transportiert die vertikale Advektion das Nitrat während des SO-Monsuns in die Schicht über der Nitracline, was durch die Nitratbudgetanalyse bestätigt wird.

Darüber hinaus zeigt diese Studie, dass das Wachstum des Phytoplanktons hauptsächlich durch die Stickstoffverfügbarkeit reguliert wird. Im Sahul-Schelf weisen die jahreszeitlichen Schwankungen der Phytoplanktonproduktion und der Zooplankton-Beweidung auf die Bottom-Up-Kontrolle im Juni-August und die Top-Down-Kontrolle im Oktober-Dezember im Zooplankton-Phytoplankton-System hin. Im Kontinentalhangbereich ist die Nitratkonzentration in der oberflächennahen Schicht erschöpft, was auf eine starke Nitratlimitierung insbesondere bei Kieselalgen hindeutet. In dieser Region ist die Produktion von Nicht-Diatomeen höher als bei Diatomeen, da Nicht-Diatomeen Ammonium effektiver aufnehmen.

Contents

1 Introduction

1.1 Background

The Arafura Sea is located in the eastern part of the Indonesian archipelago with a relatively shallow depth (< 200 m). Its border on the west is the Banda Sea with an average depth of ∼5000 m. The Arafura Sea exhibits high primary productivity and abundant fishery resources (*Alongi et al.*, 2012; *Kämpf*, 2015; *Basit*, 2020). The ocean circulation in this particular region is mainly influenced by monsoonal winds, which are the northwest (NW) and southeast (SE) monsoons (*Wyrtki*, 1961; *Gordon and Susanto*, 2001; *Kida and Richards*, 2009). The NW monsoon occurs from December to February, when the wind blows from Asia, bringing a relatively humid air (*Wyrtki*, 1961; *Alongi et al.*, 2013a). During the NW monsoon, the Arafura Sea exhibits broad cloud coverage and high precipitation (*Aldrian and Susanto*, 2003; *Alongi et al.*, 2013a). By contrast, the SE monsoon occurs from June to August, when the wind brings relatively dry air from Australia (*Wyrtki*, 1961; *Alongi et al.*, 2013a). Consequently, the Arafura Sea region receives less precipitation and reaches its minimum precipitation in August (*Aldrian and Susanto*, 2003).

During the SE monsoon, the upwelling occurs in the Arafura and Banda Seas, indicated by a lower sea surface temperature (SST) and elevated chlorophyll-a (Chl-a) concentration. The observed SST is about 4°C cooler in the SE monsoon, compared to the NW monsoon (*Waworuntu et al.*, 2000). In addition, the satellite-derived observations also show a relatively high Chl-a concentration in the northern Arafura Sea during the SE monsoon (*Kämpf*, 2015). The mechanism for such Chl-a blooms was introduced by *Wetsteyn et al.* (1990), who postulated that the enrichment of the upper layer with the nutrient-rich deeper water by vertical mixing drives the Chl-a blooms. Furthermore, a recent study by *Kämpf* (2015) suggested the nutrient supply in the Arafura Sea is driven by undercurrent (advection) mechanisms. The modeling study demonstrated that the Banda Sea slope water is the principal source of nutrient-rich water (*Kämpf*, 2015, 2016).

Previous studies have suggested that most regions outside the shelf in the Arafura Sea are oligotrophic, especially in the southern part (*Alongi et al.*, 2011; *Condie*, 2011). The concentrations of nitrate and phosphate at the surface are relatively low, while silicate is relatively high (*Condie and Dunn*, 2006). However, the northern part of the Arafura Sea shows a distinct seasonal variation, particularly in the bordering region with the Banda Sea. In the SE monsoon, the nutrient concentrations in the upper 100 m are generally higher than the NW

monsoon (*Gieskes et al.*, 1988; *Adnan*, 1990; *Ilahude et al.*, 1990; *Wetsteyn et al.*, 1990). The availability of nutrients is vital to support phytoplankton growth, primarily diatoms, which is the dominant phytoplankton group (*Adnan*, 1990).

Although nutrients play an essential role in phytoplankton growth, they are not the only factor. In addition to nutrients, temperature and light also play a role in regulating phytoplankton growth. Temperature primarily influences the phytoplankton metabolism on a cell scale. Within the defined temperature limits, phytoplankton cells division generally increases with increasing temperature (*Goldman*, 1977). Additionally, temperature also modulates the ocean thermal stratification. The stratification often prevents the nutrient injections from the deeper layer to the upper layer (*Li et al.*, 2012; *Mignot et al.*, 2014). Hence, the vertical distribution of phytoplankton is affected.

The distribution of phytoplankton is also influenced by light penetration, particularly in the water column. The light available for photosynthesis has a spectral range of 400 to 700 nm and can account for up to 43% of the incoming solar radiation (*McCree*, 1972; *Baker and Frouin*, 1987; *Fasham et al.*, 1990; *Carruthers et al.*, 2001). It is referred to as the photosynthetically available radiation (PAR), which decreases with depth. The layer where only 1% of the surface PAR remains is referred to as the euphotic zone depth (*Kirk*, 1994; *Lee et al.*, 2007). Above the euphotic depth, phytoplankton production primarily occurs and it is not limited by light. However, in the shallow region with high turbidity, particularly near the coast, the phytoplankton is more likely light-limited (*Rothlisberg et al.*, 1994; *Burford and Rothlisberg*, 1999; *Condie and Dunn*, 2006).

Overall, physical and chemical factors (e.g., nutrients, light, temperature) are essential for phytoplankton growth. Additionally, biological factors such as the grazing pressure by zooplankton are also worth considering. However, despite the importance of these factors, no previous study has addressed these aspects in the Arafura Sea. Furthermore, relating to nutrient supply, previous studies have also suggested the essential role of the Banda Sea as the source of nutrient-rich water in the Arafura Sea during upwelling seasons (*Zijlstra et al.*, 1990; *Wetsteyn et al.*, 1990; *Kämpf*, 2015). Nevertheless, the amount of nutrient transport from the Banda Sea to the Arafura Sea remains unknown due to limited observations.

According to the background mentioned above, there remain some gaps in understanding the nutrient transport in the Arafura Sea and its implications on phytoplankton distribution. In addition, the controlling factors for phytoplankton growth remain poorly understood. To fill such gaps, relying on the limited observation data is insufficient, and therefore a comprehensive numerical study is required. In the present study, a three-dimensional ecosystem model ECOHAM (ECOsystem model HAMburg) version 5 is utilized.

1.2 Research questions and outline

The present study aims to answer the following research questions:

1. How do advection and mixing affect the nutrient supply in the Arafura Sea?
2. Which processes control the nutrient budget in the Arafura Sea?
3. What are the controlling factors for phytoplankton growth in the Arafura Sea?

The present study is organized as follows. In Chapter 2, a review of the available research is presented. In Chapter 3, the methods, data, and the numerical model used in this study are described. In addition, Chapter 4 covers the model validation and model sensitivity tests. Furthermore, in Chapter 5 the discussion is focused on the nutrient dynamics, comprising nutrient fluxes and nutrient budget. Moreover, the phytoplankton limitation factors and the processes affecting the phytoplankton growth will be discussed in Chapter 6. Finally, Chapters 7 and 8 provide the final discussion and conclusion, respectively.

2 General circulation and marine ecosystem of the Arafura Sea

2.1 General circulation

The Arafura Sea is located in the eastern part of the Indonesian archipelago. It borders the Banda Sea on the east, Torres Strait on the west, the Gulf Carpentaria of Australia on the south, and the Timor Sea on the southwestern side (Figure 2.1). It comprises mostly a large shelf (about 650,000 km^2) called the Sahul Shelf, with a depth of less than 200 m (*Van Andel and Veevers*, 1965; *Basit*, 2020). The deep part of the Arafura Sea is located on the east of the Banda Sea, called the Aru Basin, with a depth down to 3650 m (*Ilahude et al.*, 1990; *Basit*, 2020).

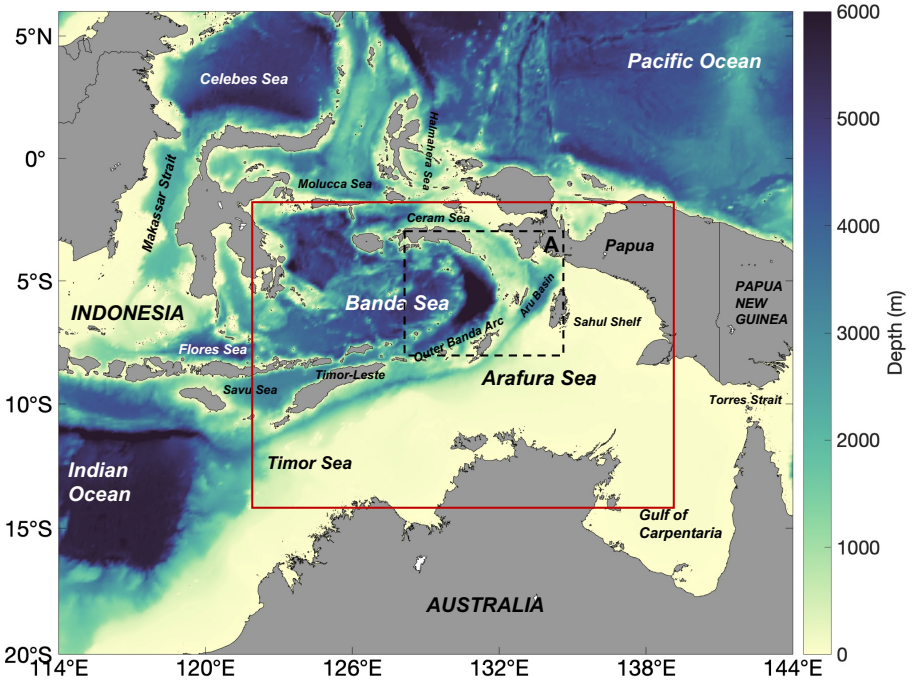

Figure 2.1: Bottom topography of the eastern part of Indonesian Sea. The red square indicates the study area. The square within the dashed black lines indicates region A, which is the study area of *Wetsteyn et al.* (1990) (see Figures 2.3 and 2.4). The bottom topography was reproduced from GEBCO Sheet G.08 compiled by R.L. Fisher of the Scripps Institution of Oceanography and extracted from the GEBCO Digital Atlas published by the British Oceanographic Data Centre on behalf of the IOC and IHO, 2003.

Tides generally contribute to the circulation in the Arafura Sea, especially enhancing the vertical mixing (*Condie*, 2011). The circulation in the Arafura Sea is dominated by large tides increasing in amplitude from east to west (*Condie*, 2011). The tidal type in the Arafura Sea is mixed with predominantly semidiurnal tides (*Wyrtki*, 1961). Previous studies have revealed that the primary semidiurnal tidal component (M2 and S2) propagates to the Arafura Sea from the Indian Ocean (*Robertson and Ffield*, 2008; *Basit*, 2020). Semidiurnal tides with a smaller amplitude also propagate from the Pacific Ocean through the Makassar Strait, Molucca Sea, and Halmahera Sea (*Robertson and Ffield*, 2008).

The adjacent sea, the Banda Sea, plays an important role in affecting the Arafura Sea circulation. It is the largest and deepest ocean basin in Indonesia and it is separated from the Arafura Sea by the Outer Banda Arc, which is ∼1250 m deep (*Zhu et al.*, 2019). In addition, the Banda Sea is known as the pathway of the Indonesian throughflow (ITF) (*Ffield and Gordon*, 1996; *Alford et al.*, 1999; *Gordon et al.*, 2010; *Zhu et al.*, 2019). A previous study by *Liang et al.* (2019) suggested that up to 80% of the ITF passes through the Banda Sea. It is also estimated that the mean ITF transport is about 15 Sv (*Sprintall et al.*, 2009; *Liang et al.*, 2019).

The circulation in the Banda Sea is highly stratified. *Zhu et al.* (2019) showed a four-layer circulation, i.e., the surface, upper, intermediate, and deep layers. Their study showed a stronger circulation in the thermocline than in intermediate and deep ($>$ 2000 m) layers. The stratified circulation has also been shown by *Liang et al.* (2019), whose modeling study revealed a clockwise-counterclockwise-clockwise circulation in the upper ($<$ 500 m) - intermediate (500–2250 m) - deep (2250 m) layer (*Liang et al.*, 2019).

2.1.1 Monsoons

According to *Aldrian and Susanto* (2003), the Arafura Sea experiences a strong influence from monsoons. For example, the prevailing wind blows southeastward over the Arafura Sea from December to February, when the air pressure over Australia is lower than in Asia (*Wyrtki*, 1961; *Basit*, 2020). It is called the northwest (NW) monsoon, which is fully developed in January (see Figure 2.2). One observes a broad cloud coverage and a peak of precipitation in the Arafura Sea during this period (*Alongi et al.*, 2013b; *Wirasatriya et al.*, 2021). Hence, the NW monsoon is often referred to as the wet monsoon with a mean precipitation reaching up to 320 mm/month (*Aldrian and Susanto*, 2003).

Oppositely, the prevailing wind blows northwestward from June to August, because the air pressure over Australia is higher than in Asia (*Wyrtki*, 1961; *Basit*, 2020). The technical term used to describe this phenomenon is the southeast (SE) monsoon, which reaches its peak in July (see Figure 2.2). As a result, the precipitation during the SE monsoon is lower than the precipitation during the NW monsoon and reaches a mean below 100 mm/month around August (*Aldrian and Susanto*, 2003). Moreover, the wind speed during the SE monsoon is also higher than the

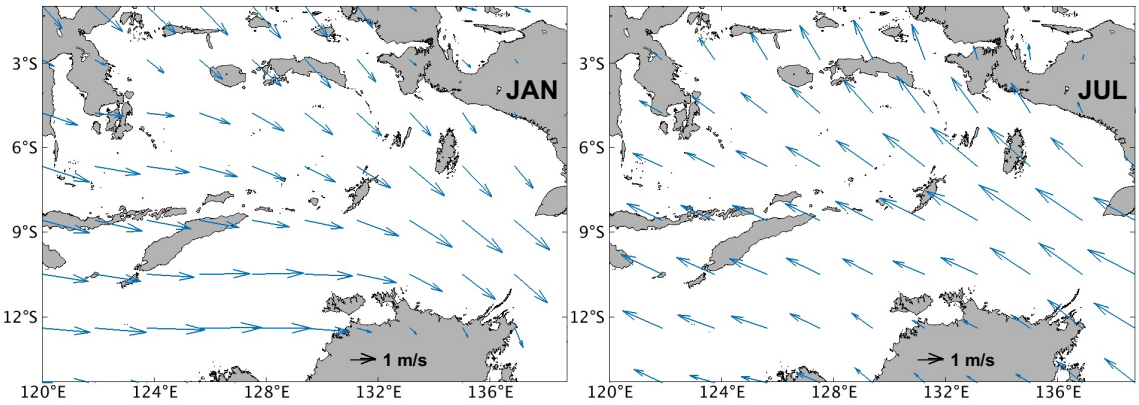

Figure 2.2: The 10-m wind distribution in January (left) and July (right) 2014 (see red box in Figure 2.1). The wind data was reproduced from NCEP Reanalysis dataset (*Kalnay et al.*, 1996).

wind during the NW monsoon (*Zijlstra et al.*, 1990). The transition between the NW and SE monsoon from March to May is referred to as the first transition monsoon. Meanwhile, the SE and NW monsoon transition is referred to as the second transition monsoon (September to November).

By contrast, the northern part of the Banda Sea shows a different precipitation pattern from the Arafura Sea. It is categorized as the anti-monsoonal region by *Aldrian et al.* (2007), which covers the northern Banda Sea, Ceram Sea, southern parts of the Molluca Sea, and the Halmahera Sea. The peak of precipitation takes place in June-July with a mean precipitation of about 300 mm/month (*Aldrian and Susanto*, 2003). The opposite precipitation pattern is expected due to strong Pacific Ocean influences in this region (*Aldrian and Susanto*, 2003). Previous studies have suggested that a small fraction of the ITF flows from the Pacific Ocean through the Molucca Sea and eastern Banda Sea (*Gordon and Fine*, 1996; *Aldrian and Susanto*, 2003).

2.1.2 Upwelling

Wyrtki (1961) postulated the occurrence of upwelling during the SE monsoon in the Arafura and Banda Seas, with a downwelling during the NW monsoon. The upwelling in the Arafura Sea has been studied based on both observations (*Zijlstra et al.*, 1990) and modeling (*Condie*, 2011; *Kämpf*, 2015, 2016; *Basit*, 2020). It is usually identified by sea surface temperature (SST) anomaly. For instance, SST is about 4 °C cooler in the SE monsoon than the NW monsoon (*Waworuntu et al.*, 2000).

The SST cooling is expected to result from upwelling and local evaporative cooling processes when the wind is blowing from the southeast bringing dry air (*Waworuntu et al.*, 2000). Part of the annual variation in SST could also be explained by seasonal changes in the net heat flux in the area, which is negative during the southeast monsoon and positive during the northwest-wind period (*Wyrtki*, 1961; *Zijlstra et al.*, 1990). SST also varies in response to vertical mixing.

A recent study has shown that the enhanced vertical mixing associated with the Madden-Julian-Oscillation (MJO) contributes more than surface heat flux (*Pei et al.*, 2021). Moreover, SST varies due to El Niño Southern Oscillation (ENSO) on the inter-annual time scale. The SST in the Arafura and Banda Seas is often cooler during El Niño and warmer during La Niña (*Gordon and Susanto*, 2001; *Pei et al.*, 2021).

The theory of the physical mechanisms of upwelling in the Arafura Sea has been developed during the last three decades. In the early-1990s, *Zijlstra et al.* (1990) hypothesized that during the SE monsoon the westward shift of the surface water would gradually remove the warm and saline surface water imported during the NW monsoon. The water was partly replaced by colder and more saline subsurface water (*Zijlstra et al.*, 1990). The study by *Zijlstra et al.* (1990) was further developed by *Kämpf* (2015) using a hydrodynamic model. The modeling study demonstrated that undercurrents flushed the northwestern Arafura Sea surface water with Banda Sea slope water on a time scale from 1 to 3 months (*Kämpf*, 2015). The undercurrent is a signature of the classic lee effect that develops in the Arafura Sea due to its bay-like configuration, shallow-water depth, and vicinity to the equator (*Kämpf*, 2015). The offshore winds lower the coastal sea level and lead to an opposing pressure-gradient force, which drives the near-bottom water shoreward and induces upwelling along the coast (*Kämpf*, 2015).

The upwelling intensity in the Arafura Sea during the SE monsoon is affected by tides and river run-off (*Basit*, 2020). A recent study by *Basit* (2020) showed that tidal forcing affects the area of the Arafura Sea with different mechanisms. For example, tidal forcing enhances the upwelling on the Sahul Shelf. The enhancement is associated with the modified horizontal pressure gradient due to tidal mixing. Subsequently, the onshore subsurface flow is identified between 50 and 200 m depth. However, tidal forcing weakens the upwelling over the continental slope of the Tanimbar Islands. It is caused by the relatively low residual offshore currents off the Papua Coast, induced by high viscosity due to tidal mixing. According to *Basit* (2020), the river run-off contributes to reducing the salinity and enhancing the westward offshore surface currents and the subsequent upwelling. The enhanced upwelling is related to increased stratification, which results in weaker vertical eddy coefficients and interfacial stress. Therefore, the vertical water movement is more pronounced.

2.2 Nutrient supply and phytoplankton dynamics

The Arafura Sea is rich in marine resources, including fisheries (*Wirasantosa et al.*, 2011). This region is one of the richest fishing grounds, fuelled by coastal upwelling and high primary productivity for some distance from the rivers (*Alongi et al.*, 2012). The primary productivity in the Arafura Sea reaches up to > 300 g C m^2 yr^{-1}, indicating a sustainable nutrient supply in this area (*Kämpf*, 2015).

Numerous research articles about the nutrients and phytoplankton in the Arafura Sea are available that were published over 30 years ago, in the 1980s and 1990s. Most of these research articles were based on observations encompassing the seasonal variation of nutrient and phytoplankton abundance related to upwelling. However, the mechanism of such nutrient enrichment remains poorly understood. The following section will discuss the available studies about plankton and nutrients in the Arafura Sea.

2.2.1 Nutrient supply

The Arafura Sea is considered to have a high productivity (*Kämpf*, 2015), even though most areas outside the shelf are oligotrophic (*Alongi et al.*, 2011; *Condie*, 2011). Both nitrate and phosphate concentrations are relatively low (< 0.3 μM) (*Condie and Dunn*, 2006). By contrast, the silicate concentration is generally high (*Condie and Dunn*, 2006), which is similar to the Banda Sea region (*Talley and Sprintall*, 2005). The high-silica water is the signature of the Banda Sea Intermediate Water (*Talley and Sprintall*, 2005).

Previous studies have suggested that the nutrient (nitrate, phosphate, and silicate) concentrations in the upper 100 m in the northern Arafura Sea are generally higher in the SE than NW monsoon (*Gieskes et al.*, 1988; *Adnan*, 1990; *Ilahude et al.*, 1990; *Wetsteyn et al.*, 1990). According to *Wetsteyn et al.* (1990), the nutrient enrichment during the SE monsoon is due to the vertical mixing with the water near the bottom, originating from the Aru Basin. Meanwhile, the nutrient enrichment in the southern Arafura Sea comes from the undercurrent-driven upwelling, which brings nutrients from the Banda Sea (*Zijlstra et al.*, 1990; *Kämpf*, 2015). The intrusion of high-nutrient Banda Sea slope water covered hundreds of kilometers, both north and south of the Aru Islands, providing enrichment along the coast of Papua (*Zijlstra et al.*, 1990).

A study by *Wetsteyn et al.* (1990) showed the nutrient distribution in the eastern Banda Sea and the northern Arafura Sea during the upwelling season in August 1984 (Figure 2.3). The mean nitrate concentration at the surface was about 0.3 μM in August (SE monsoon) and less than 0.1 μM in February (NW monsoon). The nitrate concentration was higher in deep layers, about 28.1 and 27.9 μM at 300 m depth in August and February, respectively. The upwelling was indicated by the lifting of the 1 μM nitrate layer in August. As shown in Figure 2.4, the depth distribution of the 1 μM nitrate layer in August was relatively shallower (up to 20 m) than in February.

In contrast to the SE monsoon, during the NW monsoon the nutrient supply along the coast of Papua is mainly dependent on riverine input (*Adnan*, 1990; *Ilahude et al.*, 1990). During the NW monsoon, the precipitation is high, which coincides with a high river discharge (*Ilahude et al.*, 1990; *Aldrian and Susanto*, 2003). Previous studies have indicated that the river run-off during the NW monsoon delivers nutrients and drives the high phytoplankton concentrations near the Digul River mouth (*Adnan*, 1990; *Ilahude et al.*, 1990; *Zijlstra et al.*, 1990).

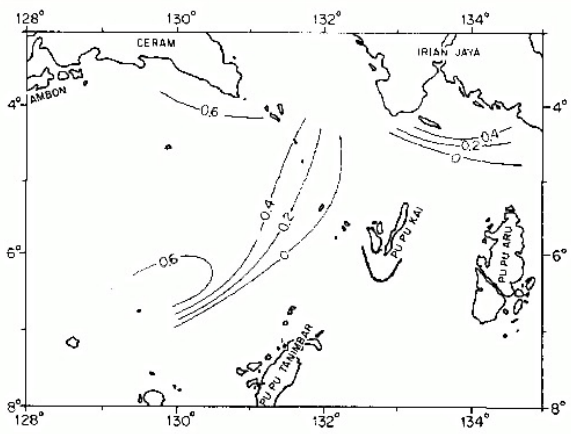

Figure 2.3: Nitrate concentration at the surface layer (0-5 m) in August 1984 (see region A in Figure 2.1). Zero lines indicate a detection limit. Figure reproduced from *Wetsteyn et al.* (1990).

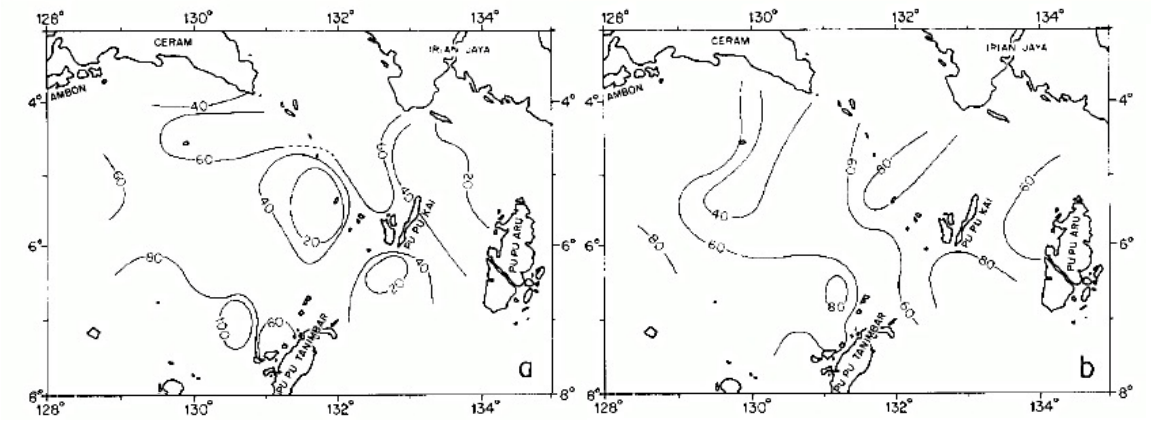

Figure 2.4: Depth distribution (m) of the nitrate 1 μM in August 1984 (left) and February 1985 (right) (see region A in Figure 2.1). Figures reproduced from *Wetsteyn et al.* (1990).

However, in August the influence of river run-off seems absent, at least for nitrate and phosphate (*Adnan*, 1990; *Ilahude et al.*, 1990).

Most of the freshwater flowing into the Arafura Sea region comes from ∼30 rivers of various sizes in Papua, delivering nutrients (*Alongi et al.*, 2013a). *Alongi et al.* (2013a) showed that dissolved inorganic carbon (DIC) is the main form of carbon discharged from all catchments in the Arafura Sea, which accounts for up to 248 t C km^{-2} yr^{-1}. Meanwhile, both particulate organic carbon (POC) and dissolved organic carbon (DOC) are small in both absolute and area-specific terms, accounting for 46 and 22 t km^{-2} yr^{-1}, respectively (*Alongi et al.*, 2013a). It contrasts with a typical carbon component discharged from other tropical rivers where DIC, POC, and DOC are usually within the same order of magnitude. Moreover, the loads of dissolved inorganic nitrogen (DIN) and dissolved inorganic phosphorus (DIP) exports from rivers in Papua to the Arafura Sea are 1.3 t N km^{-2} yr^{-1} and 0.1 t P km^{-2} yr^{-1}, respectively (*Alongi et al.*, 2013a).

In some oligotrophic regions, the nutrient inventories might be affected not

only by river input but also by atmospheric nitrogen deposition (*Duce et al.*, 2008; *Mackey et al.*, 2010). For example, it is estimated that dry nitrogen deposition could increase phytoplankton productivity in the upwelling region by up to 8% (*Mackey et al.*, 2010). In the Arafura and Banda Seas, the dominant nitrogen deposition is reduced nitrogen from agricultural activities (*Hegglin et al.*, 2016). However, it remains unknown to what degree nitrogen deposition plays a role in stimulating the phytoplankton production in these regions.

2.2.2 Phytoplankton dynamics

The dominant phytoplankton group in the Arafura Sea is diatoms (*Adnan*, 1990). During the SE monsoon, the mean abundance of diatoms can account for up to 968 cells dm^{-3}, while flagellates only account for up to 7 cells dm^{-3} (*Adnan*, 1990). In addition to phytoplankton, the dominant zooplankton group in the Arafura Sea is copepods (*Baars et al.*, 1990). In the deep area, copepods constitute 83% of the total number of animals, while on the shelf they account for 70% during the SE monsoon (*Baars et al.*, 1990). During the NW monsoon, copepods account for 77% and 57% of the total number of animals in the deep and shelf area, respectively (*Baars et al.*, 1990). Furthermore, the zooplankton biomass rapidly decreases from the SE to NW monsoons (*Baars et al.*, 1990).

A study by *Adnan* (1990) showed that the phytoplankton in the Arafura Sea is three times more abundant in August (SE monsoon) than in February (NW monsoon). During the SE monsoon, widespread phytoplankton blooms develop in a large area in the northwestern Arafura Sea or along the coast of Papua, as shown in Figure 2.5 (*Kämpf*, 2015). Satellite observations indicate that phytoplankton blooms exist in the Arafura Sea near-coastal waters all year round, probably due to continuous river discharges (*Kämpf*, 2015). However, high chlorophyll concentration in the Arafura Sea is evidently not caused by the river run-off but rather the enrichment of the upper, less saline layer by vertical mixing with the nutrient-rich deeper water (*Wetsteyn et al.*, 1990). The model findings by *Kämpf* (2015) also indicate that the undercurrents are the principal source of nutrient-rich Banda Sea slope water for the region.

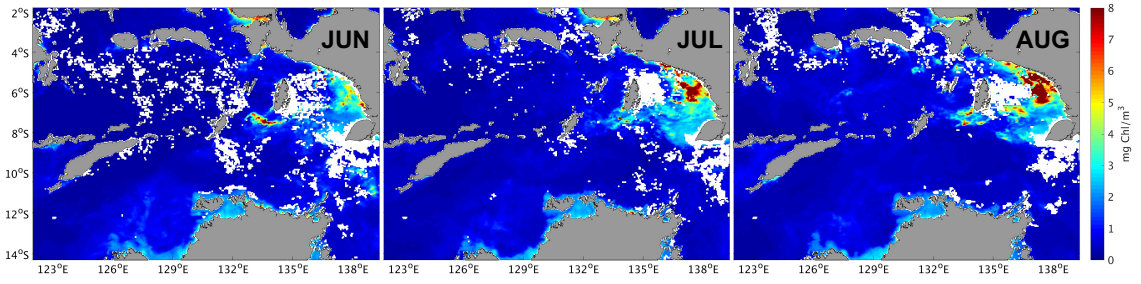

Figure 2.5: Satellite-derived chlorophyll-a at the surface during the SE monsoon (June-August) (see red box in Figure 2.1). Figures reproduced from the MODIS-Aqua dataset (*NASA Goddard Space Flight Center*, 2014).

Generally, phytoplankton dynamics are regulated by light, temperature, and nutrient availability. The light availability associated with the water clarity, plays a role in phytoplankton vertical distribution. The water clarity determines the amount of radiation or light that penetrates through the water column. The depth where only 1% of the surface photosynthetic available radiation (PAR) remains is called the euphotic zone depth (*Kirk*, 1994; *Lee et al.*, 2007). The latter often corresponds to the depth at which phytoplankton production approaches zero (*Luhtala et al.*, 2013). For example, the euphotic zone depth in the Banda Sea is 83 ± 29 m during the NW monsoon and 47 ± 16 m during the SE monsoon (*Kinkade et al.*, 1997). On the other hand, the euphotic zone depth in the Arafura Sea is shallower, which is ∼20 m during the SE monsoon (*Ilahude et al.*, 1990).

The second factor regulating phytoplankton growth is temperature. A main influence of temperature is changing the phytoplankton cells division rate (*Goldman*, 1977). Within the defined temperature limits, phytoplankton cells division generally rises with increasing temperature (*Goldman*, 1977). In addition to regulating the phytoplankton metabolism, temperature also modulates ocean stratification. The thermal stratification mainly prevents nutrient intrusion/exchange from the deeper layer to the euphotic zone in the upper layer (*Li et al.*, 2012; *Mignot et al.*, 2014). For this reason, thermal stratification indirectly relates to the third limitation factor for phytoplankton, which is nutrient availability.

In most marine ecosystems, nitrogen is commonly limiting the primary and secondary production (*Goldman et al.*, 1979; *Chen et al.*, 2004). Previous studies have suggested that based on observations, nitrogen is mainly low in concentrations and more rapidly depleted than other nutrients (*Glibert*, 1988; *Burford and Rothlisberg*, 1999). However, in some marine habitats, phosphorus occasionally replaces nitrogen as the first limiting nutrient (*Thingstad and Rassoulzadegan*, 1995; *Chen et al.*, 2004). Such change can affect the phytoplankton species structure. In the South China Sea, the phosphorus depletion near the surface during summer results in dominant phytoplankton species shifted from diatoms to dinoflagellates (*Ning et al.*, 2004).

However, in the Arafura Sea the effect of limiting factors on phytoplankton growth varies between onshore (0–20 m) and offshore regions (*Condie and Dunn*, 2006). The shallow part of the Arafura Sea (Sahul Shelf) tends to have higher turbidity, especially in the coastal or onshore region (*Rothlisberg et al.*, 1994; *Burford and Rothlisberg*, 1999; *Condie and Dunn*, 2006). Therefore, in this region, the phytoplankton growth during the SE monsoon tends to be light-limited (*Rothlisberg et al.*, 1994; *Burford and Rothlisberg*, 1999; *Condie and Dunn*, 2006). Nonetheless, the limiting factors might vary vertically in the deeper part, such as in the Aru Basin. In the euphotic zone, phytoplankton tends to be nutrient-limited because it receives abundant light but often lacks a nutrient. By contrast, the lower and the part below the euphotic zone show that phytoplankton is light-limited (*Mignot et al.*, 2014). Hence the phytoplankton growth is there not nutrient-limited.

The combined effect of light and nutrient limitations in a vertical direction is

mainly associated with the deep chlorophyll maximum (DCM). *Varela et al.* (1992) suggested that the DCM is a result of a balance between upward nutrient flux and light intensity. Hence, it usually appears between the nutrient-depleted upper layers and the light-limited lower layers of the euphotic zone (*Li et al.*, 2012). The DCM is also varying between low and high latitudes, associated with thermal stratification. For example, thermal stratification only occurs occasionally in the North Sea due to surface warming and weaker winds. In this particular region, the DCM only appears in summer (*Weston et al.*, 2005). However, the DCM might be found throughout the year in tropical water that has permanently stratified water (*Takahashi and Hori*, 1984).

The typical feature of DCM is high phytoplankton biomass and production (*Li et al.*, 2012). However, a study by *Mignot et al.* (2014) also indicated that the DCM might also be independent of the maximum phytoplankton carbon biomass. The reason is that the ratio of Chl-a to carbon biomass increases with depth due to photoacclimation (*Mignot et al.*, 2014). Furthermore, the DCM contributes substantially to the integrated Chl-a and primary production. For example, in the Western Mediterranean, the phytoplankton of the DCM contributes up to 30% of the total primary production over the water column (*Estrada*, 1985; *Li et al.*, 2012).

In addition to the physical properties of water, hydrodynamic processes also affect the phytoplankton distribution. Hydrodynamic processes comprise advection and mixing in both vertical and horizontal directions. The vertical advection is often the main driver of nutrient transport to the euphotic zone and it generates the phytoplankton blooms in wind-driven upwelling regions. In other upwelling areas affected by internal waves, vertical mixing is the primary driver of the nutrient supply to the euphotic zone (*Ma et al.*, 2021). This is the case with the northern part of the South China Sea. In addition, the internal waves play an important role in the resuspension of sediment and the exchange of nutrients (*Tuerena et al.*, 2019; *Ma et al.*, 2021). While vertical advection and mixing transport nutrients to the euphotic zone in most upwelling regions, in some upwelling regions the horizontal advection and mixing play a role in transporting the nutrient away before it is used for phytoplankton production. In the Benguela upwelling system, the horizontal stirring causes a reduction of phytoplankton production (*Hernández-Carrasco et al.*, 2014).

In the upwelling system, diatoms are usually more dominant during the peak of upwelling (*Bach et al.*, 2020), such as found in the Arafura Sea during the SE monsoon (*Adnan*, 1990). During the upwelling season, diatoms mainly contribute 50% to the Chl-a in the euphotic zone (*Gieskes et al.*, 1988). However, when upwelling relaxes, and nutrient concentrations decrease, flagellates are often more dominant (*Bach et al.*, 2020). Such typical changes in dominant phytoplankton species (succession) can be partially reset by any mechanism that weakens surface stratification and resupplies nutrients (*Estrada and Marrasé*, 1987; *Burger et al.*, 2020).

Additionally, the peak of wind-driven upwelling is not always associated with

the peak of chlorophyll concentration (*Manzer et al.*, 2019). A study by *Manzer et al.* (2019) suggests that the timing of high Chl-a events coincides with the relaxation of upwelling favorable wind conditions. Such mechanisms are fundamental in the shelf area. Wind relaxation can be an essential driver of localized high phytoplankton biomass on the inner shelf by advecting a recently upwelled water into the coastal embayments (*Manzer et al.*, 2019). In the Arafura Sea, a time gap between the high phytoplankton biomass (high Chl-a) and the peak of upwelling is also found. The peak of upwelling occurs in July–August, but the maximum of Chl-a is found in September, as shown in satellite-derived Chl-a observations (*NASA Goddard Space Flight Center*, 2014).

3 Methods and data

3.1 HAMSOM description

3.1.1 Model design

The hydrodynamic simulation was performed using the 3-D baroclinic numerical model HAMSOM (HAMburg Shelf Ocean Model). HAMSOM is based on the nonlinear primitive equations and formulated on the Arakawa-C grid (*Backhaus*, 1983, 1985; *Pohlmann*, 1996). The model has been applied to numerous shelf sea regions (*Liu*, 2016), including Indonesian waters, as undertaken by *Putri* (2005), *Mayer and Damm* (2012), and *Basit* (2020). The main equations employed in HAMSOM for the xy-coordinate direction are described as follows (*Putri*, 2005):

The momentum equation for x and y coordinate direction:

$$\frac{\partial u}{\partial t} + u\frac{\partial u}{\partial x} + v\frac{\partial u}{\partial y} + w\frac{\partial u}{\partial z} - fv = -\frac{1}{\rho}\frac{\partial p}{\partial x} + A_H \bigtriangledown^2 u + \frac{\partial}{\partial z}\left(A_v \frac{\partial u}{\partial z}\right) + F_x \tag{3.1}$$

$$\frac{\partial v}{\partial t} + u\frac{\partial v}{\partial x} + v\frac{\partial v}{\partial y} + w\frac{\partial v}{\partial z} + fu = -\frac{1}{\rho}\frac{\partial p}{\partial y} + A_H \bigtriangledown^2 v + \frac{\partial}{\partial z}\left(A_v \frac{\partial v}{\partial z}\right) + F_y \tag{3.2}$$

The vertical motion for z-coordinate direction:

$$\frac{\partial p}{\partial z} = -\rho g \tag{3.3}$$

The continuity equation:

$$\frac{\partial u}{\partial x} + \frac{\partial v}{\partial y} + \frac{\partial w}{\partial z} = 0 \tag{3.4}$$

Transport equation for temperature and salinity:

$$\frac{\partial T}{\partial t} + u\frac{\partial T}{\partial x} + v\frac{\partial T}{\partial y} + w\frac{\partial T}{\partial z} = K_H \bigtriangledown^2 T + \frac{\partial}{\partial z}\left(K_v \frac{\partial T}{\partial z}\right) + S_T \tag{3.5}$$

$$\frac{\partial S}{\partial t} + u\frac{\partial S}{\partial x} + v\frac{\partial S}{\partial y} + w\frac{\partial S}{\partial z} = K_H \bigtriangledown^2 S + \frac{\partial}{\partial z}\left(K_v \frac{\partial S}{\partial z}\right) + S_S \tag{3.6}$$

Equation of state:

$$\rho = \rho(S, T, p) = \rho_o + \rho \tag{3.7}$$

In Equations (3.1)-(3.4), u and v are the velocity components in the x and y direction, respectively; f is the Coriolis parameter; g is the gravitational acceleration; ρ is the seawater density; p is pressure at depth z; A_H and A_v are the horizontal and

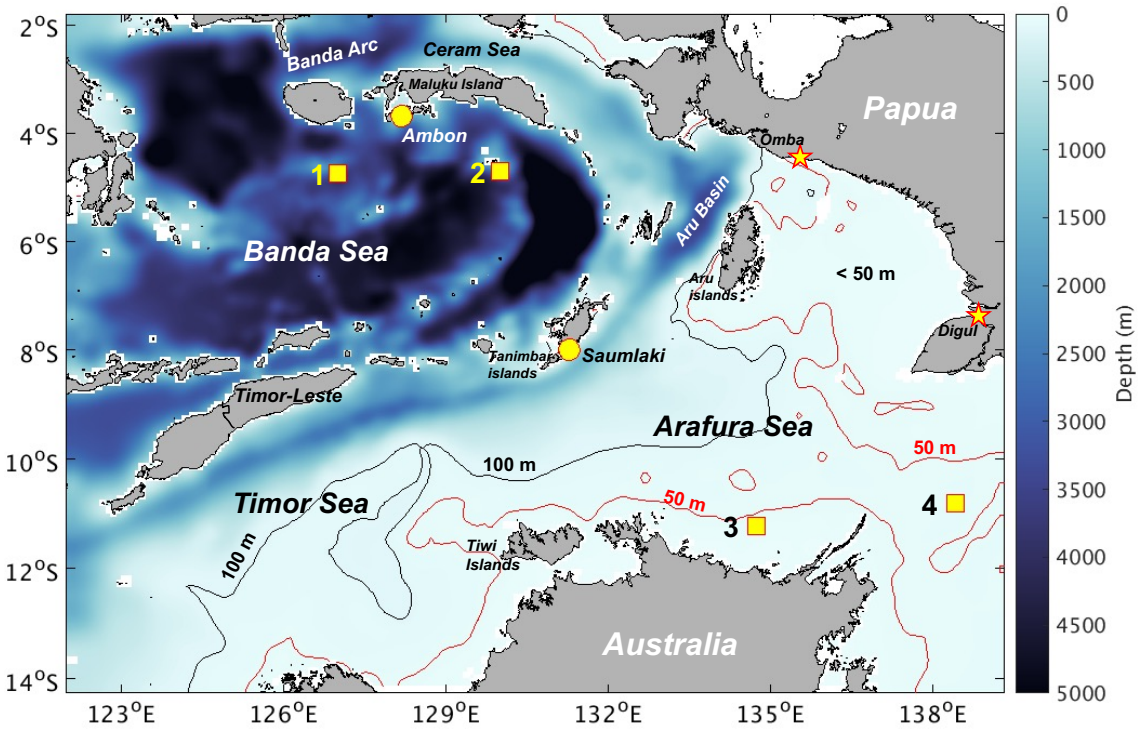

Figure 3.1: Model area and bottom topography. Yellow circles (◯) indicate the stations with sea level observations, i.e., Stations Ambon and Saumlaki. Yellow squares (□) indicate the stations with temperature observations. Yellow stars (★) indicate the locations of Omba and Digul Rivers. Red and black contours indicate the 50 m and 100 m depth, respectively.

vertical eddy viscosity coefficients; F_x and F_y are the external forces in the x and y direction, respectively. In addition, in Equations (3.5)-(3.7), T is temperature; S is salinity; K_H and K_v are the horizontal and vertical eddy diffusivities; S_T and S_S are the source terms for temperature and salinity; and ρ_o is the reference density.

The model domain extends from 121.9° to 139.3° E and from 1.8° to 14.3° S which covers the Arafura and Banda Seas (Figure 3.1). The bottom topography for the model was composed from ETOPO5 (Earth topography five-arcminute grid). The horizontal resolution of the model was 1/15° (∼7.42 km) in both latitude and longitude. The vertical grid resolution was based on the z-coordinate system with 45 layers of increasing thickness from 5 m for the upper layers to 500 m for the deep layers. The simulation was running for 30 years from 1985 to 2014 to capture the inter-annual variability. The model results in 2014 were used for the analysis and ecosystem model input.

3.1.2 Model input and forcing

At the initial state, the sea surface height (SSH) and velocity field were set to zero. Meanwhile, the initial values of temperature and salinity were derived from the MPI-OM (Max-Planck Institute Ocean Model) output of January 1985. MPI-OM is the

ocean-sea ice component of the MPI-ESM (Max-Planck Earth System Model) which is also based on the primitive equations (*Marsland et al.*, 2003).

HAMSOM is forced by different variables, namely:

1. meteorological forcing at the sea surface;
2. temperature and salinity (TS) fields along the lateral open boundaries;
3. tides along the lateral open boundaries;
4. river discharges at the river mouths.

The meteorological forcing was provided by the NCEP Reanalysis dataset (*Kalnay et al.*, 1996). Seven atmospheric parameters were used for the HAMSOM simulation, i.e., 2-m air temperature, 2-m dew point temperature, 10-m zonal (u) wind component, 10-m meridional (v) wind component, total cloud cover, total precipitation, and mean sea level pressure. The reanalysis data has a spatial resolution of 1.875° and a temporal resolution of 6 hours. The meteorological data was linearly interpolated in space and time for each time step onto the model grid.

Along the lateral open boundaries, the TS fields were prescribed as the model forcing. The daily TS fields were derived from the above-mentioned global model MPI-OM (*Mayer and Damm*, 2012). These datasets were interpolated to the model domain and applied daily.

In addition to the TS fields, tidal forcing was also applied along the lateral open boundary. Tidal forcing is one of the essential components when simulating the circulation of the Arafura Sea. Based on previous studies, the Arafura Sea is dominated by strong tides that generally increase in amplitude from east to west (*Wolanski*, 1993; *Condie*, 2011). In the present model forcing, the tidal forcing comprises thirteen constituents, i.e., Q1, O1, P1, K1, N2, M2, S2, K2, Mf, Mm, M4, MS4, and Mn4. The tidal data was derived from TPXO Global Tidal Solution (*Egbert and Erofeeva*, 2002).

According to the study by *Basit* (2020), the Arafura Sea circulation is affected by a significant upwelling that is influenced by river input. Therefore, the daily river discharge was implemented as a model forcing. The river discharge rates were derived from the WaterGAP Global Hydrology Model (WGHM) (*Hunger and Döll*, 2008). A total of 191 rivers distributed across the entire model domain were used (see Appendix A). The present study focuses on the rivers located in Papua Island that deliver freshwater into the Arafura Sea, especially the Digul and Omba Rivers, constituting the two major rivers in this region. The monthly mean climatology of freshwater discharge of the Digul and Omba Rivers derived from the WGHM is shown in Figure 3.2. The data indicates that the river discharge of both rivers reaches the maximum in April and the minimum in November (Figure 3.2).

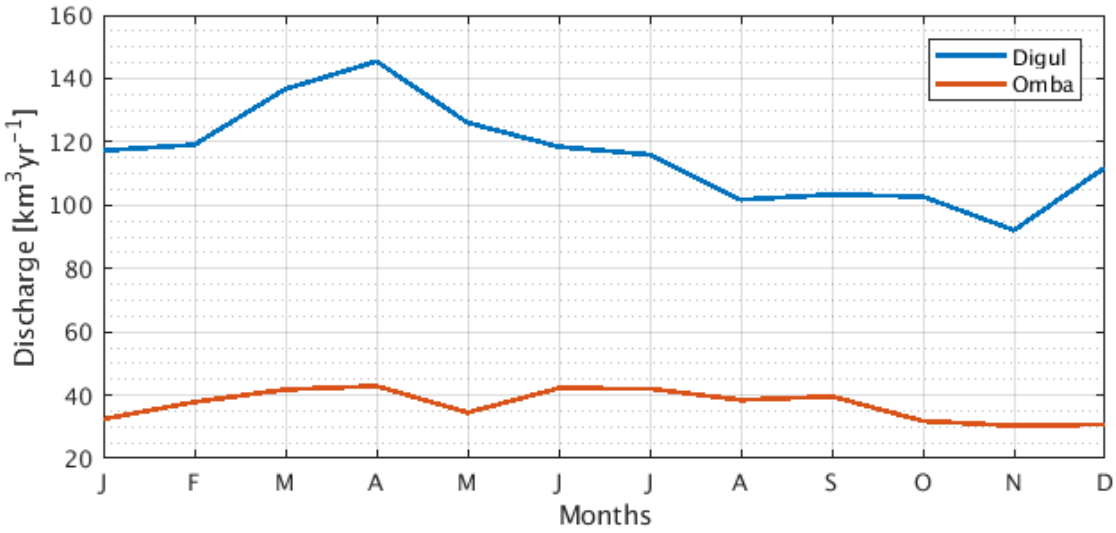

Figure 3.2: Monthly mean climatology (1990-2014) of the freshwater discharge of the Digul and Omba Rivers derived from WGHM (*Hunger and Döll*, 2008). Note that these discharge values are used as HAMSOM input. Thus, values are recalculated based on the grid size of the input cells at the specific river mouth.

3.2 ECOHAM description

3.2.1 Model design

ECOHAM (ECOsystem model HAMburg) is a lower trophic model based on the one-dimensional (1D) models by *Kühn and Radach* (1997) and *Pätsch et al.* (2001) (*Kühn and Radach*, 1997; *Pätsch et al.*, 2001; *Pätsch and Kühn*, 2008). At the initial development in the Institute of Oceanography, University of Hamburg, ECOHAM version 1 was applied to the North Sea ecosystem (*Moll*, 1998). In recent years, the model has been applied to several regions such as the Bohai Sea (*Liu*, 2016) and Indonesian Seas (*Mayer et al.*, 2018) to answer various biogeochemical questions. In the present study the latest ECOHAM version 5 was employed which is the updated version from ECOHAM version 4 described in *Lorkowski et al.* (2012) and *Pätsch et al.* (2018). The current ECOHAM version 5 is revised in major parts for application on new software and hardware platforms in order to provide a parallel processing, i.e., message passing interface (MPI) (*Große et al.*, 2018).

ECOHAM includes interactions between 31 state variables (see Table B.1). The state variables included are four nutrients (nitrate, ammonium, phosphate, and silicate), two functional phytoplankton groups (diatoms and non-diatoms), two zooplankton groups (microzooplankton and mesozooplankton), two fractions of detritus (slowly and fast sinking), bacteria, labile and semi-labile dissolved organic matter, DIC, total alkalinity, oxygen, calcite, and the benthic state variables calcite and particulate organic matter (C, N, P, Si) (*Lorkowski et al.*, 2012; *Große et al.*, 2018). The schematic illustration of the ECOHAM components is shown in Figure 3.3.

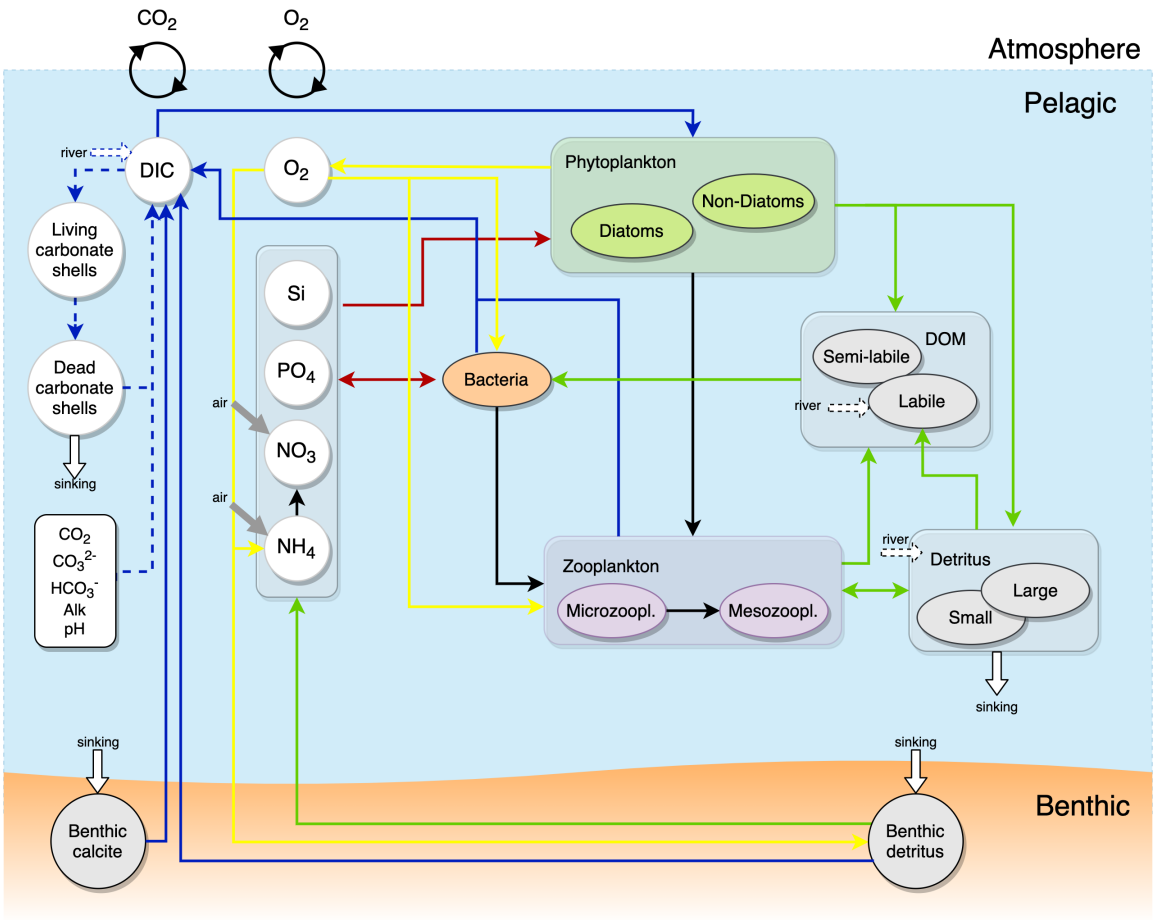

Figure 3.3: ECOHAM scheme shows how model components interact with each other. Black arrows represent predator-prey interaction, green represents fluxes of non-living organics, red represents nutrient fluxes, yellow represents oxygen, blue arrows represent DIC fluxes, and dashed represents the carbonate system. Figure adapted from *Lorkowski et al.* (2012) and *Große et al.* (2018).

The general equation of ECOHAM comprises SOURCES and SINKS terms: biological processes ($var1\_var2$), air-sea flux (air_var), atmospheric deposition (atm_var), benthic remineralization (var_brm), and fluxes from the sediment into the pelagic (sed_var) (*Große et al.*, 2018). The term $var1\_var2$ indicates a flux from variable $var1$ to variable $var2$. All pelagic variables are affected by river input (riv_var), precipitation (pev_var), restoring (res_var), and hydrodynamic processes (hyd_var) which involve horizontal and vertical advection (adh_var, adv_var) and mixing (mxh_var, mxv_var) (*Große et al.*, 2018). The restoring term (res_var) refers to the lateral boundary condition, which is described in Section 3.2.2. Furthermore, in this study the precipitation (pev_var) term was neglected. Therefore, the differential equation for the concentration of any pelagic state variable var is described as follows:

$$\begin{aligned} \frac{\partial var}{\partial t} = \; & SOURCES(var) - SINKS(var) \\ & + riv\_var + res\_var + hyd\_var \end{aligned} \tag{3.8}$$

The SOURCES and SINKS represent the sums of the source and sink processes

listed in the equations in Table B.2. Detritus is the only variable that experiences sedimentation (*var_sed*) among all pelagic state variables. It is being deposited into the sediment due to sinking. Therefore, for the detritus variable, the term $-var\_sed$ was added to Equation 3.8.

For the ecosystem model, the same domain and spatial resolution were used as for the HAMSOM hydrodynamic model (see Section 3.1). The simulation was conducted for 2014 with two years of spin-up. The ECOHAM simulation was carried out with a 30-minute time step.

3.2.2 Model input and forcing

For the initial condition, the values of all state variables were determined. The initial values of nitrate, phosphate, silicate, and oxygen were derived from the climatological dataset of the World Ocean Atlas 2018 (WOA18) (*Garcia et al.*, 2018). Meanwhile, the initial values for the rest of the state variables were derived from the regional model output generated by the Global Coastal Ocean Modelling System (GCOMS) (*Holt et al.*, 2009) provided by Susan Kay at Plymouth Marine Laboratory (pers. comm.). In the work of GCOMS, *Holt et al.* (2009) used the Proudman Oceanographic Laboratory Coastal Ocean Modelling System (POLCOMS) coupled with the European Regional Seas Ecosystem Model (ERSEM) (*Butenschön et al.*, 2016).

In addition to state variables, the extinction coefficient of water was also prescribed. The extinction coefficient of water (*extw*) was set between 0.1 m^{-1} to 0.2 m^{-1}, which varies spatially. The *extw* value was determined based on the bathymetry. It is assumed that the shallow sea has a higher *extw* value than a deeper sea. The shallow area with a depth less than 50 m has an *extw* value of 0.2 m^{-1}. The area with a depth between 50 m and 100 m has an *extw* value of 0.15 m^{-1}. Moreover, the *extw* of the area deeper than 100 m was assumed to be 0.1 m^{-1} (see Appendix C).

ECOHAM was running offline using the hydrodynamic fields generated by HAMSOM. The hydrodynamic forcing comprises a three-dimensional advective flow field, turbulent mixing, temperature, and salinity. In this study, the 24h averages of the hydrodynamic fields were used, interpolated for every time step of 30 minutes. Therefore, the daily variation of the hydrodynamic fields (e.g., tides) was omitted in the biogeochemical processes.

1) Meterological forcing

The meteorological forcing provided by the NCEP Reanalysis was used, which is the same as used in the hydrodynamics model (see Section 3.1). The meteorological forcing that is required for ECOHAM input is the 2-hourly short-wave radiation, calculated according to Budyko's model, which considers the astronomic insulation and cloudiness, including the effect of surface albedo (*Lorkowski et al.*, 2012). In addition to 2-hourly data, the daily mean short-wave radiation was also calculated

using the same method. The latter is used to determine an optimum irradiance (see Section 3.2.3.1).

2) Atmospheric nitrogen deposition

The atmospheric nitrogen deposition was included in the ecosystem model. There were two atmospheric nitrogen depositions, i.e., oxidized and reduced nitrogen. The nitrogen depositions are released from the atmosphere as gas, dry, and wet depositions. For this study, only dry and wet depositions were considered. The oxidized nitrogen (NOy) is coming from human activities, largely from fossil fuel combustion, but also from the increased use of nitrogen fertilizers (*Fowler et al.*, 1998). Besides, the reduced nitrogen (NHx) is coming from agricultural activities.

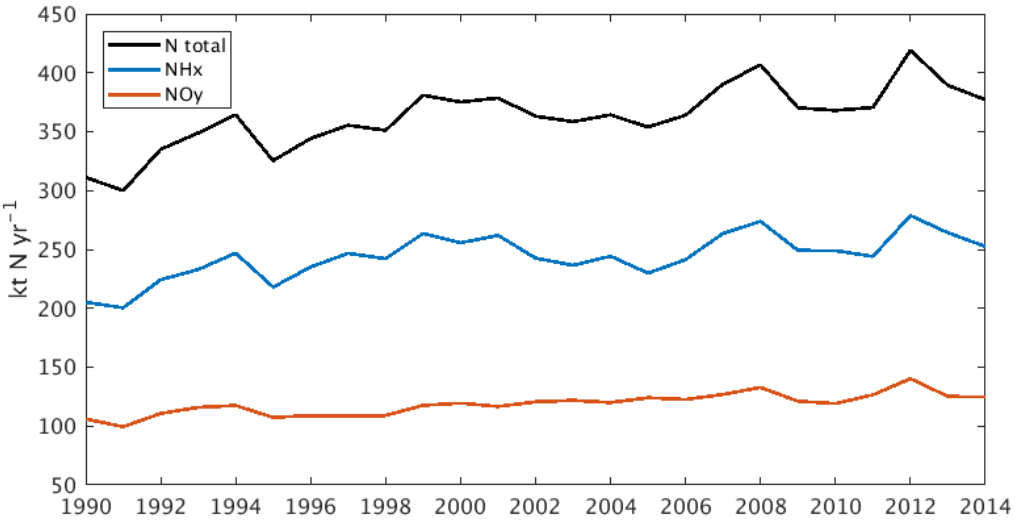

Figure 3.4: Atmospheric nitrogen deposition over region of the Arafura and Banda Seas provided by *Hegglin et al.* (2016). N total is the sum of NHx (reduced nitrogen) and NOy (oxidized nitrogen).

In the present study, the nitrogen deposition data was generated by the NCAR-CCMI-2-0 (National Center for Atmospheric Research - Chemistry Climate Model Initiative) model provided by *Hegglin et al.* (2016). This dataset is part of the "input4MIPs" forcing datasets and is used for the sixth phase of the Coupled Model Intercomparison Project (CMIP6) (*Sellar et al.*, 2020). The spatial resolution of the data is 2.5° in longitude and 1.89° in latitude. In addition, the data was linearly interpolated to the model grid of the Arafura and Banda Seas. Finally, the annual average of the nitrogen deposition is used for ECOHAM input.

The annual atmospheric nitrogen deposition over the model domain is presented by Figure 3.4. The data shows that the amount of reduced nitrogen in the Arafura and Banda Seas region is higher than oxidized nitrogen. Moreover, Figure 3.4 also shows an increasing trend of total nitrogen deposition from 1990 to 2014.

3) River

According to some studies, the riverine input plays a role in phytoplankton

blooms in the Arafura Sea (*Wetsteyn et al.*, 1990; *Kämpf*, 2016). As such, the river was affiliated to ECOHAM as forcing/boundary conditions. There were a total of 191 rivers distributed in the study area (see Appendix A).

The river freshwater discharge and river nutrient loads were prescribed. The river freshwater discharge was derived from WaterGAP, which is the same as the HAMSOM forcing (see Section 3.1). Meanwhile, the river nutrient loads were derived from the Global Nutrient Export from WaterShed 2 (GlobalNEWS2). GlobalNEWS2 is a global, spatially explicit, multi-element, and multi-form model of nutrient exports by rivers (*Mayorga et al.*, 2010). For ECOHAM forcing, the climatological nutrient loads from GlobalNEWS2 were used.

A total of 12 nutrient river loads was prescribed, comprising alkalinity, DIC, DOC, POC, POS (particulate organic silica), POP (particulate organic phosphorus), PON (particulate organic nitrogen), nitrate, silicate, phosphate, nitrite, and ammonia. The nitrate, silicate, ammonia, and phosphate value of each river is shown in Figure 3.4. It is found that a large amount of nutrients is delivered by the river located in Papua (River ID 176, 180, 183, 187, and 190, see Appendix A).

The river nutrient data from GlobalNEWS2 shows a relatively high fraction of organic materials at the Digul River mouth. These organic materials are considered a labile fraction used in the biological process in ECOHAM. After conducting some ECOHAM simulation experiments, it was found that this high fraction of organic materials leads to immediate remineralization. The remineralization process absorbs oxygen so that the oxygen in the Digul River mouth rapidly decreases, resulting in an ECOHAM simulation crash. Hence, adjusting the value of organic materials in river input is essential to overcome such rapid depletion of oxygen.

According to *Ittekkot* (1988), most of the measured organic material belongs to the refractory/semi-labile that is accumulated in marine sediments. Meanwhile, only 35% of the measured organic material belongs to the labile fraction globally. It indicates that around one-third of the measured organic material is being used in the biological process in the ecosystem model time scale (hours). For this reason, the concentration of organic material from rivers was reduced. After conducting some ECOHAM experiments, it has been shown that the labile fraction must be even lower for this application of the Arafura Sea. Therefore, the concentration of organic material from rivers was reduced by a factor of 100 to avoid the rapid depletion of oxygen.

4) Lateral boundary conditions

On the lateral open boundary, the values of all state variables were prescribed. In the present study, the boundary values are referred to as restoring (*res_var*). Boundary conditions of nitrate, phosphate, silicate, and oxygen were derived from the WOA18 climatological monthly datasets (*Garcia et al.*, 2018). In addition to WOA18, GCOMS monthly output was used for the rest of the pelagic state variables (pers. comm.). These monthly datasets were interpolated for each time step.

3.2.3 Ecosystem model parameterization

In general, the variation of phytoplankton concentration over time is determined by hydrodynamic and biogeochemical processes. Hydrodynamic processes comprise mixing and advection in both vertical and horizontal directions. Biogeochemical processes for phytoplankton comprise sources and sinks. Sources for phytoplankton are growth through nutrient uptake and C-fixation. Sinks for phytoplankton are mortality, grazing by zooplankton, and exudation.

3.2.3.1 Phytoplankton growth

Phytoplankton growth is affected by temperature, light, and nutrients. Temperature (T) plays a role in regulating the rate of phytoplankton growth to be faster or slower, but it does not stop phytoplankton growth. In this study, the effect of temperature on phytoplankton growth is expressed as a temperature factor. The following Equation 3.9 defines the temperature factor (f_T) in ECOHAM:

$$f_T(T) = Q_{10}^{\frac{T-10^\circ C}{10^\circ C}} \tag{3.9}$$

with $1 \leq Q_{10} \leq 2$ (*Sherman et al.*, 2016)

On the other hand, light and nutrients play a role in limiting the phytoplankton growth or even stopping it. Therefore, to express the effect of light and nutrients on phytoplankton growth, the terms light limitation factor and nutrient limitation factor were used. The light-depending growth rate for phytoplankton (F_{par}) is defined by the equation given below:

$$F_{par}(I, v_i, X_i) = v_i \cdot \frac{I_{par}(z)}{I_{opt}} \cdot \exp\left(1 - \frac{I_{par}(z)}{I_{opt}}\right) \tag{3.10}$$

with: $X_1 = p1c$, $v_1 = v_{p1}$ and $X_2 = p2c$, $v_2 = v_{p2}$

In Equation 3.10, v_{p1} is the maximum growth rate of diatoms (1.1 d^{-1}); v_{p2} is the maximum growth rate of non-diatoms (0.9 d^{-1}); z is depth (meter); $I_{par}(z)$ is the depth-depending PAR; and I_{opt} is the optimum irradiance (see Equation 3.13). The depth-depending PAR ($I_{par}(z)$) is influenced by silt, chlorophyll, and the extinction coefficient of water (see Equations 3.11 and 3.12).

$$I_{par}(z) = k_{par} \cdot I_0 \cdot \exp(\epsilon(z)) \tag{3.11}$$

$$\epsilon(z) = (extw + k_c \cdot phc + k_s \cdot silt) \cdot z \tag{3.12}$$

In the above Equations 3.11 and 3.12, k_{par} is the photosynthetic active fraction of solar radiation (dimensionless); I_0 is solar radiation/irradiance at the surface (W m^{-2}); $extw$ is the extinction coefficient of water (m^{-1}); k_c is the extinction coefficient for phytoplankton (m^2 (mmol C)$^{-1}$); phc is the phytoplankton concentration (mmol C m^{-3}); k_s is the extinction coefficient for silt (m^2 mg^{-1}); and $silt$ is the silt concentration (mg m^{-3}).

$$\begin{aligned}
&\frac{\partial I_{opt}}{\partial t} = rupli \cdot (actual_light - I_{opt}) \\
&rupli = 0.25 d^{-1} \\
&actual_light = k_{par} \cdot \bar{I}_0 \cdot \exp(\epsilon(z_a)) \\
&z_a = \min(z, z_{max}); z_{max} = 4 \text{ m} \\
&\bar{I}_0 = \text{daily mean irradiance at the surface}
\end{aligned} \tag{3.13}$$

The third factor for phytoplankton growth is the nutrient limitation. In ECOHAM, the nutrient limitation factor is formulated based on Michaelis-Menten kinetics (1913), which shows that the rate of an enzyme-catalyzed reaction is proportional to the concentration of the enzyme-substrate (*Johnson and Goody*, 2011). The nutrient limitation factor (lim_nut) is described by a hyperbolic function (Equation 3.14), which is referred to as Michaelis-Menten equation.

$$lim\_nut = \frac{N}{K_N + N} \tag{3.14}$$

In the above equation, N and K_N are nutrient concentrations and the half-saturation of nutrients, respectively. Equation 3.14 is adequate to describe the nutrient dependency of phytoplankton growth rate for a non-substitutable limiting nutrient, which is catalyzed by a single transport mechanism (*Morel and Prieur*, 1977; *Cullen et al.*, 1993). In this case, Equation 3.14 is suitable for the phosphate and silicate limitations of phytoplankton growth. In ECOHAM, the limitation factors of phosphate for diatoms ($lip1\_1p$) and non-diatoms ($lip2\_1p$) are defined by Equations 3.15 and 3.16. Moreover, the limitation factor of silicate ($lip1\_5s$) for diatoms is defined by Equation 3.17.

$$lip1\_1p = \frac{n1p}{K_P + n1p} \tag{3.15}$$

$$lip2\_1p = \frac{n1p}{K_P + n1p} \tag{3.16}$$

$$lip1\_5s = \frac{n5s}{K_S + n5s} \tag{3.17}$$

In the above Equations 3.15–3.17, K_P is the half-saturation constant of phosphate ($n1p$) uptake by diatoms/non-diatoms and K_S is the half-saturation constant of silicate ($n5s$) uptake by diatoms.

In ECOHAM, the source of nitrogen for phytoplankton growth is differentiated into two forms of DIN, i.e., nitrate and ammonium. Phytoplankton can use nitrate as well as ammonium as the source for their growth (*Soetaert and Herman*, 2008). However, phytoplankton will take up ammonium preferably compared to nitrate in the presence of these two nutrients (*Soetaert and Herman*, 2008). Nitrate has to be reduced so that it can be assimilated into phytoplankton biomass, and this reduction costs more energy (*Soetaert and Herman*, 2008). In this case, nitrate uptake by non-diatoms is inhibited by ammonium. To express the ammonium inhibition, the

Michaelis-Menten inhibition kinetics that combines both nitrate and ammonium is used (*Haney and Jackson*, 1996). The formulation of competitive inhibition of a single enzyme is expressed by Equations 3.18 and 3.19 (*Cullen et al.*, 1993; *Haney and Jackson*, 1996).

$$Q_n = \frac{N'_n}{1 + N'_n + N'_r} \tag{3.18}$$

$$Q_r = \frac{N'_r}{1 + N'_n + N'_r} \tag{3.19}$$

where $N'_n = [NO_3^-]/K_{NO_3^-}$ and $N'_r = [NH_4^+]/K_{NH_4^+}$

In ECOHAM, Equations 3.18 and 3.19 are adapted as the limitation factors of nitrate and ammonium for phytoplankton growth. The nitrate limitation factors for diatoms ($lip1\_n3$) and non-diatoms ($lip2\_n3$) are described in Equations 3.20 and 3.21. Additionally, the ammonium limitation factors for diatoms ($lip1\_n4$) and non-diatoms ($lip2\_n4$) are described in Equations 3.22 and 3.23.

$$lip1\_n3 = \frac{n3n/K_1}{1 + n3n/K_1 + n4n/K_{21}} \tag{3.20}$$

$$lip2\_n3 = \frac{n3n/K_1}{1 + n3n/K_1 + n4n/K_{22}} \tag{3.21}$$

$$lip1\_n4 = \frac{n4n/K_{21}}{1 + n3n/K_1 + n4n/K_{21}} \tag{3.22}$$

$$lip2\_n4 = \frac{n4n/K_{21}}{1 + n3n/K_1 + n4n/K_{22}} \tag{3.23}$$

In the above Equations 3.20–3.23, K_1 is the half-saturation constant of nitrate ($n3n$) uptake by phytoplankton (diatoms and non-diatoms), which is set to 0.5 mmol N m^{-3}. Moreover, K_{21} and K_{22} are the half-saturation constant of ammonium uptake by diatoms and non-diatoms, respectively. The value of K_{21} and K_{22} are 0.5 mmol N m^{-3} and 0.05 mmol N m^{-3}, respectively. Finally, total nitrogen limitations for diatoms ($lip1\_hn$) and non-diatoms ($lip2\_hn$) are expressed by Equation 3.24 and 3.25.

$$lip1\_hn = lip1\_n3 + lip1\_n4 \tag{3.24}$$

$$lip2\_hn = lip2\_n3 + lip2\_n4 \tag{3.25}$$

Net primary production (NPP) is the uptake of DIC by phytoplankton (minus respiration) (*Große et al.*, 2017). In other words, NPP is the rate at which the full metabolism of phytoplankton produces biomass via carbon fixation (*Sigman and Hain*, 2012). The carbon uptake rate is more likely not equal to the instantaneous growth rate due to the storage of nutrients and nutrient adaptation (*Droop*, 1973; *Hense*, 2018). Carbon fixation is the process of converting the inorganic carbon to organic compounds, and it is an integral part of photosynthesis. The following equation expresses the Redfield carbon fixation:

$$NPP_{red} = p1c \cdot f_T(T) \cdot F_{par}(I, v_{p1}, p1c) \cdot lim\_nps \tag{3.26}$$

The term *lim_nps* in Equation 3.26 represents the nutrient limitation factor for phytoplankton. In the case of diatoms, *lim_nps* depends on the availability of nitrate, ammonium, phosphate, and silicate (*Große et al.*, 2017). Nutrient limitation follows Liebig's law of the minimum (*Große et al.*, 2017).

In ECOHAM, the NPP, which is referred to as $NPP_{effective}$ for diatoms, is formulated in Equation 3.27. The term h_dic_p1c is the NPP diatoms without nutrient limitation, which is formulated by Equation 3.28.

$$NPP_{effective} = NPP_{red} + excess(h\_dic\_p1c - NPP_{red}) \tag{3.27}$$

$$h\_dic\_p1c = p1c \cdot f_T(T) \cdot F_{par}(I, v_{p1}, p1c) \tag{3.28}$$

with $0 \leq excess \leq 1$

The special feature of ECOHAM involves allowing for 'excess' production or 'carbon overconsumption' (*Lorkowski et al.*, 2012). Excess production or carbon overconsumption is defined as carbon fixation via photosynthesis when bioavailable nutrients (nitrate and phosphate) in the surface layers are depleted (*Toggweiler*, 1993; *Lorkowski et al.*, 2012). This excess carbon is released by phytoplankton and is immediately channeled into the pool of slowly degradable semi-labile DOC (SOC) (see Section 3.2.3.2) (*Lorkowski et al.*, 2012). Thus, this excess carbon does not increase the phytoplankton biomass (*Prowe et al.*, 2009). In ECOHAM, the excess carbon is formulated as follows:

$$NPP_{excess} = NPP_{effective} - NPP_{red} \tag{3.29}$$

When $excess = 0$, there is no carbon overconsumption. Meanwhile, $excess = 1$ means that the total DIC consumption by phytoplankton is only governed by temperature and light availability (Equation 3.28). The value of *excess* between 0 and 1 indicates less carbon overconsumption. In the present study, the *excess* value in ECOHAM was set to 0.5.

3.2.3.2 Phytoplankton loss

In ECOHAM, the phytoplankton losses occur via exudation, mortality, and grazing by zooplankton. The mortality depends on temperature f_T and is defined by the following equation:

$$M_{X_i} = f_T(\mu_{u,Y_i} \cdot X_i + \mu_{q,Y_i} \cdot X_i \cdot X_i) \tag{3.30}$$

with: $X_1 = p1c$, $Y_1 = p1$ and $X_2 = p2c$, $Y_2 = p2$

In Equation 3.30, $p1c$ and $p2c$ are the diatom and non-diatom concentrations; μ_{up1} and μ_{up2} are linear mortality rate for diatoms and non-diatoms, which are set to 0.035 d^{-1}; μ_{qp1} and μ_{qp2} are the quadratic mortality factor for diatoms and non-diatoms, which are set to 0.01 m^3 mmol $C^{-1}d^{-1}$.

In real conditions, phytoplankton may build aggregates. The phytoplankton aggregates are built from the combined processes of colliding and sticking (*McCave*,

1984; *Kriest and Evans*, 1999). Aggregates 0.5 mm or larger in diameter contribute to a very high phytoplankton concentration (*Kiørboe et al.*, 1990). For example, in nearshore, aggregates comprise large diatoms that can account for up to 30% of total chlorophyll-a (Chl-a) (*Kriest and Evans*, 1999). Furthermore, these aggregates are rapidly sinking, and it implies the mechanism of vertical transport of phytoplankton to the seafloor (*Kiørboe et al.*, 1990). In ECOHAM, the sinking of aggregates is represented by the quadratic mortality, as shown by the quadratic term in Equation 3.30 (right-hand side).

Furthermore, the grazing mortality of phytoplankton is defined based on the approach by *Fasham et al.* (1990). For example, the grazing rates of microzooplankton (G_{1i}) and mesozooplankton (G_{2i}) are defined by the following equations:

$$G_{1i} = f_T \cdot G_{1,max} \cdot \frac{p_{1i}.X_{1i}}{K_3 + \sum_j p_{1j} \cdot X_{1j}} \cdot z1c \tag{3.31}$$

with: $X_{11} = p1c$, $X_{12} = p2c$, $X_{13} = d1c$, $X_{14} = bac$

$$G_{2i} = f_T \cdot G_{2,max} \cdot \frac{p_{2i}.X_{2i}}{K_3 + \sum_j p_{2j} \cdot X_{2j}} \cdot z2c \tag{3.32}$$

with: $X_{21} = p1c$, $X_{22} = p2c$, $X_{23} = d1c$, $X_{24} = bac$, $X_{25} = z1c$

In the above Equations 3.31 and 3.32, $p2c$ refers to the non-diatom concentration; $d1c$ is the detritus-C concentration; bac is the bacteria-C concentration; $G_{1,max}$ is the maximum ingestion rate of microzooplankton (0.5 d^{-1}); $G_{2,max}$ is the maximum ingestion rate of mesozooplankton (0.4 d^{-1}); and K_3 is the half-saturation constant for zooplankton grazing (1 mmol N m^{-3}).

In addition to mortality, another sink pool of phytoplankton is the exudation of organic matter. Exudation is defined as the active release of excess photosynthates that accumulate when carbon fixation exceeds incorporation into new cell material (*Bjørrisen*, 1988). The exudation of dissolved ($p1c\_doc$) and 'excess' ($p1c\_soc$) organic carbon by diatoms is defined by the Equations 3.33 and 3.34, respectively. In Equation 3.33, γ_1 is the exudation fraction of diatoms, given as 0.05. The terms NPP_{red} and NPP_{exc} are defined in Equations 3.26 and 3.28.

$$p1c\_doc = \gamma_1 \cdot NPP_{red} \tag{3.33}$$

$$p1c\_soc = NPP_{excess} = NPP_{effective} - NPP_{red} \tag{3.34}$$

3.2.3.3 Chlorophyll-a

In the present study, Chl-a is used as a proxy of phytoplankton biomass as it is a pigment that is common to all planktonic autotrophs and can be remotely measured in bulk (*Wang et al.*, 2009). Chl-a is calculated based on the chlorophyll to carbon (Chl:C) ratio. A previous study by *Falkowski et al.* (1985) showed that Chl:C in phytoplankton grown in culture is highly variable, ranging from 0.003 to $\leq$ 0.1 mg Chl-a (mg C)$^{-1}$. Another study by *Riemann et al.* (1989) showed that chlorophyll

content of phytoplankton in eutrophic lakes and the coastal area mostly ranges from 1.5% to 3.7%, corresponding to Chl:C ratios of 0.015 to 0.037. However, the relationship between the chlorophyll and phytoplankton carbon biomass is non-linear due to the complex influences of light, nutrients, and temperature in the euphotic zone (*Armstrong*, 2006; *Wang et al.*, 2009). In general, the Chl:C ratio increases from high to low light under nutrient-replete conditions, called "photoacclimation" (*Wang et al.*, 2009).

To calculate the Chl:C ratio, the empirical approach from *Cloern et al.* (1995) was used. *Cloern et al.* (1995) described the Chl:C as a function of temperature (T), daily mean irradiance ($\bar{I}_{par}$), and nutrient-limited growth rate as shown in Equation 3.35. In ECOHAM, Equation 3.35 is used to calculate Chl-a for both diatoms and non-diatoms. In this approach, the Chl-a contributes to shading. Note that lim_nps in Equation 3.35 is the nutrient limitation factor of the most limiting nutrient. For diatoms, the limiting nutrients could be phosphate, nitrate, ammonium, or silicate.

$$Chl : C = 0.003 + 0.0154 \cdot \exp(0.05T) \cdot \exp(-0.059\bar{I}_{par}) \cdot lim\_nps \tag{3.35}$$

3.2.4 Nutrient budget plots

In this study, the nutrient budget is calculated for water columns with specific depth intervals. The nutrient budget for each grid cell comprises the biological and physical fluxes. The physical part is the difference of fluxes into and out of the cell through its interfaces. Those input and output fluxes change the nutrient concentration in each grid cell under the assumption of conservation of volume. However, ECOHAM considers the volume changes due to sea level variations (*Pätsch and Kühn*, 2008). Sea level variations depend on atmospheric pressure gradients, wind, and tides. Therefore, the volume of grid cells in the first layer is not conserved. For example, strong winds might shift a significant amount of water at the surface, producing a large change in grid cell volume in the first layer. In this case, some grid cells in the first layer might nearly fall dry. Based on this approach, the content difference of a specific nutrient in grid cells is divided into the content change due to the difference of the concentration and change of volume (details given in *Pätsch and Kühn* (2008)).

As previously mentioned in Section 3.1, the vertical grid used in ECOHAM consists of 45 layers of increasing thickness from 5 m for the upper layers to 500 m for the deep layers. For instance, the upper 25 m has five layers, with each layer thickness of 5 m. The nutrient budget, for example, nitrate, in the upper 25 m at one station is calculated as the sum of fluxes of each grid cell within the upper 25 m as follows:

1. The fluxes of processes affecting nitrate concentration within one grid cell are calculated. These processes comprise biological sources and sinks (see Table B.1 in Appendix B) and local physical processes (advection and mixing). The unit of these fluxes is nitrate concentration integrated over the cell thickness and time (mmol N m^{-2}).

2. Each calculated flux is plotted in a time-series line graph, represented by a black line. In addition, the red line in a time-series graph represents nitrate concentration integrated over the five vertical layers. It is equal to the sum of fluxes within the upper 25 m. For better representation, this value is sometimes multiplied or divided by a constant number.
3. The calculated fluxes at the end of the year represent the annual fluxes.

3.2.5 Ecosystem model scenarios

When simulating the marine ecosystem, people often find it challenging to determine the parameters such as the phytoplankton growth rate or a temperature factor. These parameters are primarily obtained from literature or empirically from experiments. However, it is often encountered that despite using the actual parameter value being obtained from the literature or measurement, the output lacks the accuracy to represent the actual conditions. Moreover, the model accuracy not only depends on the parameter value but also the combination of different parameter settings. Therefore, some ECOHAM experiments with different parameter settings were conducted to find an optimum parameterization. In addition, the sensitivity test is also conducted because it is the first ECOHAM application in the Arafura and Banda Seas region.

Within the whole dataset required for ECOHAM's input, silt is relatively difficult to determine because there is no available literature and observational dataset for silt in the Arafura and Banda Seas region. Previous literature has provided the sediment discharges from the rivers (*Milliman et al.*, 1999; *Alongi et al.*, 2012), but it has not addressed the silt fractions in the sediments. Therefore, due to the data unavailability, some ECOHAM experiments were performed with different silt concentrations from a constant to spatially varying silt concentrations. The value range for silt concentration was taken from the ECOHAM application for the North Sea (*Lorkowski et al.*, 2012). This ECOHAM application for the North Sea used the varying silt concentrations from 0.0 to 35.7 g m^{-3}, which decreases offshore (*Lorkowski et al.*, 2012). However, for ECOHAM experiments for the Arafura and Banda Seas, the silt concentration ranging from 1 to 10 g m^{-3} was used. For ECOHAM experiments with spatially varying silt concentrations, the silt concentration in the Arafura Sea is assumed to be higher than in the Banda Sea. Indeed, the Banda Sea is considered an open sea and is less turbid than the Arafura Sea.

The ECOHAM experiments showed an insignificant change in surface chlorophyll-a concentration between the simulation with spatially varying and constant silt concentrations of 1 g m^{-3}. These two experiments produced a rather similar spatial pattern of surface chlorophyll-a. Based on this result, this document only presents the ECOHAM experiments using constant silt concentration. The first simulation called "Scenario 1," assumes a constant silt concentration of 10 g m^{-3}. The second "Scenario 2" assumes a lower silt concentration of 1 g m^{-3}.

3.3 Observational data

3.3.1 Observational data for HAMSOM validation

The hydrodynamic model results were compared to observations to evaluate the model performance. The sea level and vertical temperature profiles were used to validate the HAMSOM results. More information and the measurement locations are shown in Table 3.1 and Figure 3.1.

Table 3.1: Observational data for HAMSOM validation

No	Parameter	Location	Time
1	Sea level (m)	Ambon and Saumlaki	2014
2	Vertical temperature (°C)	st 1	22 November 2013
		st 2	26 November 2013
		st 3	17 October 2012
		st 4	18 October 2012

The sea level data were used to evaluate the model performance in simulating the reaction of the ocean to wind and density variations. The latter governs the geostrophic component of ocean circulation. The observed hourly sea level data in 2014 was provided by the University of Hawaii Sea Level Center (UHSLC) (*Caldwell et al.*, 2015). As this study is not focusing on daily but seasonal time scales, the daily variations, such as tides, were omitted. Thus, for validation, the tidal signals were filtered out from the observed and simulated (HAMSOM) sea level (hourly) data. Afterward, these filtered sea level data from observations and simulations at Ambon and Saumlaki stations were compared (Figure 4.1).

In addition to sea level, the vertical temperature profile was also used to validate the model results. There were two temperature stations located in the Banda Sea (1 and 2) and two stations (3 and 4) in the Arafura Sea (Figure 3.1). The vertical temperature data in stations (st) 1 and 2 was measured by a conductivity, temperature, and depth (CTD) instrument. This dataset was obtained by the Center of Deep-Sea Research, Indonesian Institute of Science, as a part of the annual expedition in 2013. Additionally, the vertical temperature profiles at stations 3 and 4 were also measured by CTD (Figure 3.1). This dataset was obtained from WOD18 (*Boyer et al.*, 2018). These locations represent the important regions in association with the upwelling process. Therefore, despite limited observational data in both space and time, the validation of vertical temperature was considered to be representative for the model quality as a whole.

3.3.2 Observational data for ECOHAM validation

The simulated chlorophyll-a and nutrient concentrations (nitrate and phosphate) were compared with observational data to validate the ecosystem model output. The chlorophyll-a data was obtained from MODIS-Aqua satellite measurements (*NASA Goddard Space Flight Center*, 2014) (Figure 4.4). Additionally, the nutrient data was obtained from in-situ measurements conducted in 1998, 2012, and 2013 (*Boyer et al.*, 2018). More information and the measurement locations are shown in Table 3.2 and Figure 3.5.

Table 3.2: Location and date of nutrient measurements

Station	Date	Station	Date
A1 (Banda Sea)	3 March 1998	C1 (Timor Sea)	29 July 2013
A2 (Banda Sea)	2 March 1998	C2 (Timor Sea)	30 July 2013
A3 (Banda Sea)	1 March 1998	C3 (Arafura Sea)	30 July 2013
A4 (Banda Sea)	28 February 1998	C4 (Arafura Sea)	17 October 2012
A5 (Banda Sea)	28 February 1998	C5 (Arafura Sea)	18 October 2012

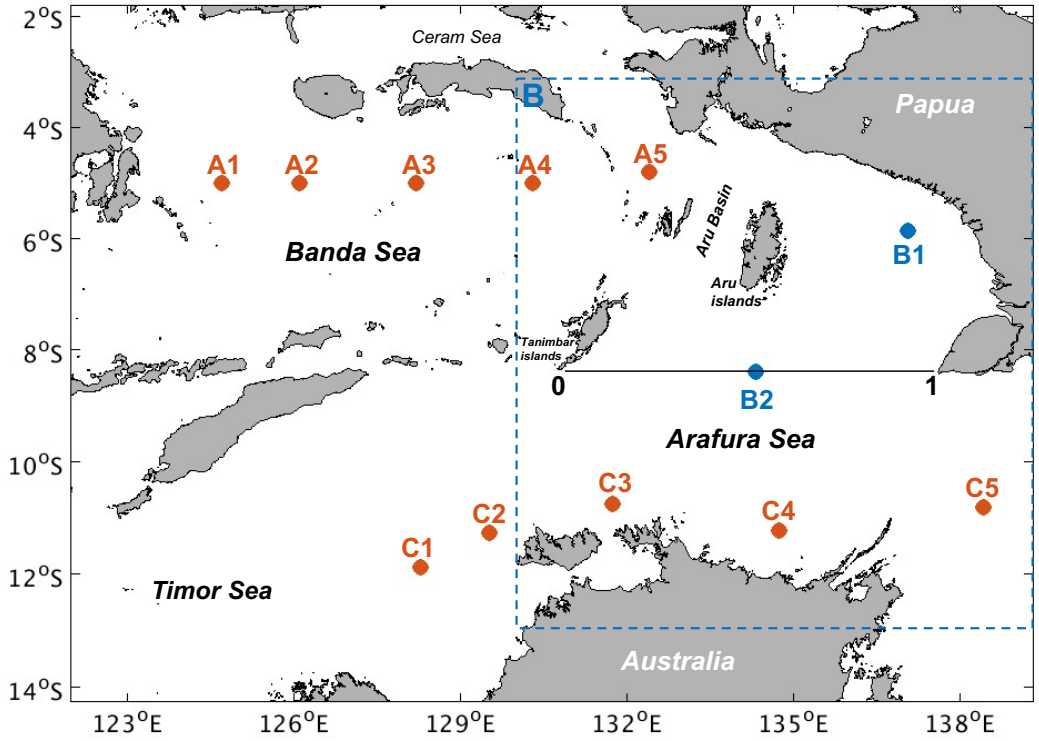

Figure 3.5: Location of nitrate and phosphate measurements indicated by red dots (•). The square within the dashed blue lines shows the region B.

4 Model validation and sensitivity tests

4.1 HAMSOM validation

4.1.1 Sea level

The measurement locations of sea level in Ambon and Saumlaki are located directly at the coast. However, these locations are not represented well by the model topography. For example, the tide gauge station in Ambon is situated inside the Outer Ambon Bay (OAB). The OAB, facing the Banda Sea, is approximately 4 km wide (*Basit*, 2020; *Salamena et al.*, 2021), while the model resolution is about 7.42 km. As a result, the topography in the HAMSOM model does not resolve the OAB correctly. For this reason, HAMSOM provides no simulation results at the exact location of the tide gauge station in Ambon. A similar problem is found at Saumlaki station, where the exact location of the tide gauge station is considered land in the HAMSOM model topography. Therefore, the validation points for Ambon and Saumlaki were taken several grid points away from the original location, in this case, three grids or ∼22 km from the coast.

In general, sub-tidal sea level variations are driven directly by atmospheric forcing (i.e., air pressure and winds) and indirectly by density (baroclinic compensation) (*Liang et al.*, 2019). Both observations and simulation show these sub-tidal sea level variations at Ambon and Saumlaki stations, i.e., lower during the SE than the NW monsoon (Figure 4.1). At Ambon station, these sea level variations are also related to mass divergence in the Banda Sea, as previously described by *Gordon and Susanto* (2001). The simulation underestimates the observed sea level at Ambon station, with a root mean square error (RMSE) of 4.24 cm. Nevertheless, the simulation represents the seasonal variation (wind-driven and density-driven) quite well, with a high correlation coefficient of 0.91.

Unlike at Ambon station, the simulated sea level at Saumlaki station does not fit the observations well (Figure 4.1), with a lower correlation coefficient of 0.69 and an RMSE of 6.54 cm. This discrepancy might occur due to the atmospheric forcing, which is not representable for Saumlaki station. As previously described in Section 3.1, the spatial resolution of atmospheric forcing is 1.875° or ∼208 km, which is about 29 times larger than the model resolution. Another factor may be the unrealistic representation of the local topography at this specific location, which has a strong

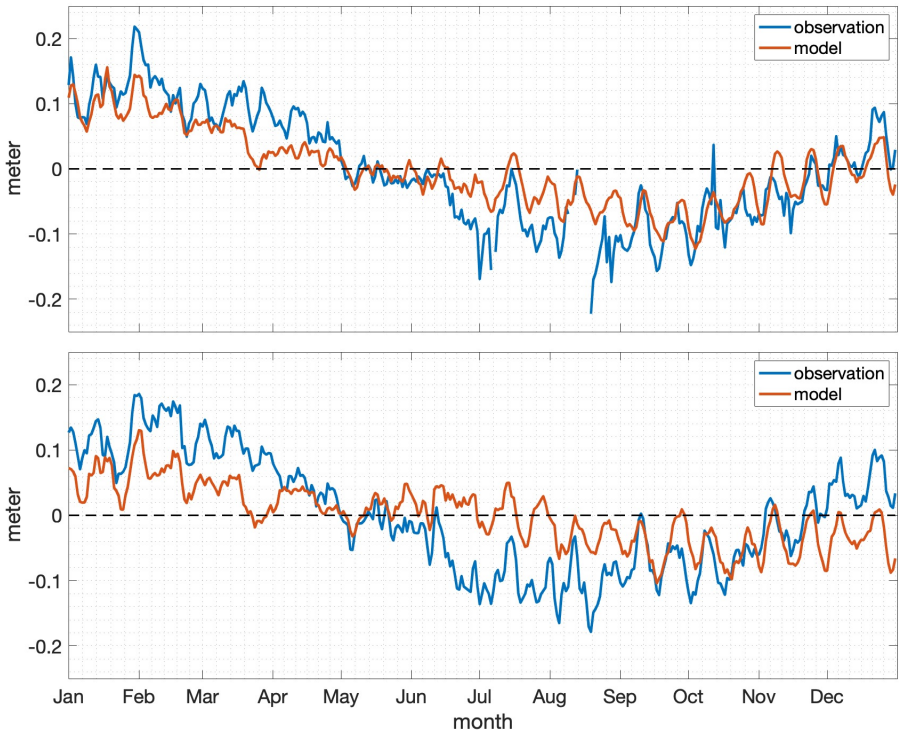

Figure 4.1: Time series of observed (blue) and simulated (red) sub-tidal sea level at Ambon (upper panel) and Saumlaki (lower panel) stations in 2014. The tidal and high frequencies ($\leq$ 24 hours) signals were filtered out. Note that the presented data were normalized to its annual mean.

impact on the bottom friction, which acts in the model. Since Saumlaki station is located in a shallower area than Ambon station, the wrong description of the bottom friction could have a stronger impact at this location. Consequently, the wind forcing is less effective at dragging water, and it produces a small change of sea level, for example, in July-August. Therefore, although the wind is stronger during this period (SE monsoon), the simulation underestimates the observed sea level.

4.1.2 Vertical temperature profile

In general, the vertical temperature profiles from the HAMSOM simulation in the Banda Sea represent real conditions reasonably well (Figure 4.2). The average correlation coefficient for stations 1 and 2 is 0.995. Furthermore, the average RMSE for both stations is 1.186°C, which is relatively small. According to the observed temperature at station 1 (blue dashed line in Figure 4.2 left), the thermocline layer in November is found between 100 and 300 m, where the temperature rapidly decreases from 25 to 9.8°C. Moreover, the temperature in the thermocline layer at station 2 is decreasing from 23.5 to 10.8°C. Overall, HAMSOM underestimates the temperature by 1–3°C within 200 and 1200 m depth, while it overestimates the temperature below 1200 m depth by 1–2°C. Additionally, the simulated temperature in the Banda Sea, specifically in the upper 200 m, shows a good fit with observations.

Unlike the Banda Sea, the observed vertical temperature profiles in the Arafura Sea in October are relatively homogenous. Figure 4.2 shows that the temperature at station 3 is about 0.5°C higher than at station 4. Moreover, despite the lack of observational data (less than ten samples), the vertical temperature profiles show the absence of stratification at both stations. The homogenous water column is related to the vertical mixing induced by tides. According to *Condie* (2011), the Arafura Sea is dominated by large tides that increase in amplitude from east to west.

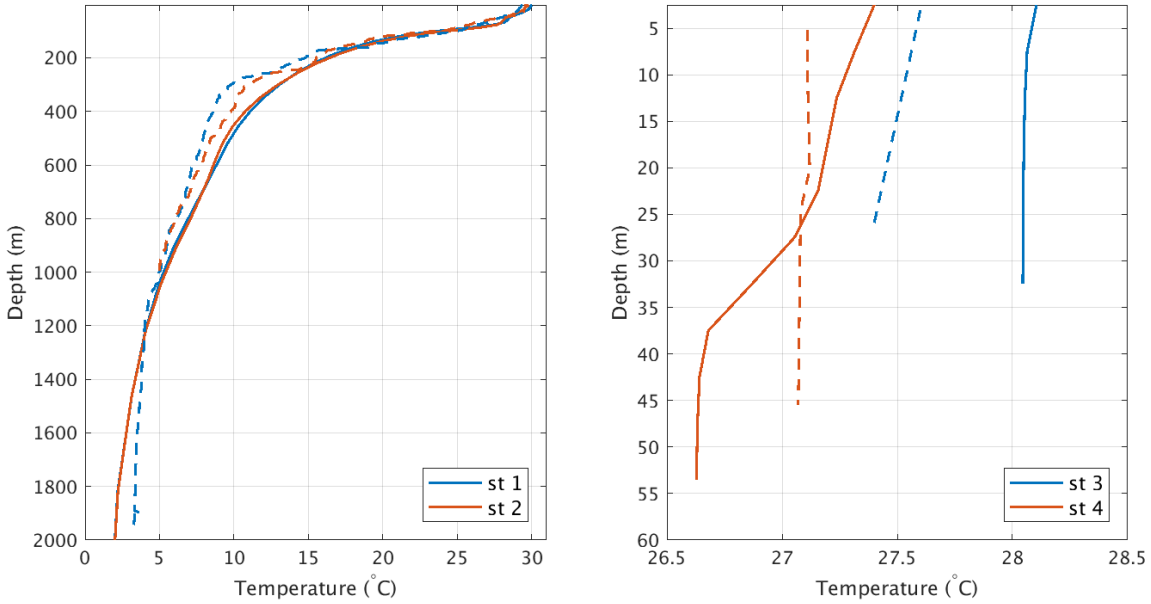

Figure 4.2: Comparison of vertical temperature profiles in the Banda Sea (left) in November 2013 and Arafura Sea (right) in October 2012. The thick and dashed line indicate the simulated and observed temperature, respectively. The location of stations 1–4 is shown by Figure 3.1.

Generally, HAMSOM simulation overestimates the temperature at station 3 by about 0.5°C (Figure 4.2). The simulated temperature at station 3 is 28.1°C at the surface and slightly decreases to 28.04°C at the bottom. On the other hand, the simulated temperature at station 4 is lower than station 3, with a more stratified profile (Figure 4.2). The temperature decreases from 27.4°C at the surface to 26.6°C at the bottom. Overall, the simulation overestimates the temperature by 0.3°C in the upper 25 m, while it underestimates the temperature by 0.5°C below a depth of 25 m.

4.2 ECOHAM validation

4.2.1 Spatial distribution of chlorophyll-a

The Chl-a observational data used in the present study is the monthly composite from MODIS-Aqua satellite measurements. In principle, the Chl-a measurements by satellite are based on the reflected radiance of visible light (400–700 nm), particularly

the blue and green spectrum from the sea surface (*Lalli and Parsons*, 1997). The Chl-a concentration is calculated from the relative change of seawater color from blue to green with a specific algorithm. For example, the algorithm of the MODIS-Aqua satellite is the OC3 v6 algorithm (*NASA Goddard Space Flight Center*, 2014). This standard algorithm is suitable for open waters but less suitable for coastal waters (*NASA Goddard Space Flight Center*, 2014).

According to *Morel and Prieur* (1977), the seawater is classified into case-1 and case-2 waters based on its optical properties. The variation in optical properties of case-1 waters is mainly influenced by phytoplankton and its accompanying biological origin material (*Sathyendranath et al.*, 2000). Moreover, the case-1 waters can range from oligotrophic (phytoplankton-poor) to the eutrophic (phytoplankton-rich) area, provided that the contributions from other substances are relatively small (*Sathyendranath et al.*, 2000). By contrast, the case-2 waters are not only influenced by the phytoplankton but also other substances such as suspended inorganic particles and yellow substances (*Sathyendranath et al.*, 2000). For example, open and deep sea, like the Banda Sea is classified as case-1 waters. Meanwhile, shallow and coastal area such as the Arafura Sea is classified as case-2 waters.

According to some studies, the OC3 algorithm is frequently inaccurate in estimating the Chl-a concentration in case-2 waters (*Abbas et al.*, 2019; *Lah et al.*, 2014; *Darecki and Stramski*, 2004). For example, the study in Malacca Strait (located between Malaysia Peninsula and Sumatra, Indonesia) by *Lah et al.* (2014) showed that the MODIS satellite overestimates the Chl-a concentration in the southern part, which is classified as case-2 waters. The southern part of Mallaca Strait is a relatively shallow region (less than 50 m), and it is relatively turbid due to the river discharge (*Tan et al.*, 2006; *Lah et al.*, 2014). By contrast, in the northern part of Mallaca Strait, which is classified as case-1 waters, the MODIS satellite underestimates the Chl-a concentration (*Lah et al.*, 2014). Another study by *Winarso and Marini* (2017) for case-1 waters in the west of Sumatra (Indian Ocean) and the north of Papua (Pacific Ocean) revealed that the satellite underestimates the Chl-a concentration by 4.8%. Despite the possibility of overestimated Chl-a concentrations, particularly near the coast and at the river mouth, satellite observation is beneficial for assessing the Chl-a concentration at large scales.

The model results are compared with satellite observations in January, April, July, and October. These months represent the northwest, first transition, southeast, and second transition monsoons, respectively. The satellite observations show that the high Chl-a concentration or the bloom near the coast of Papua is observed every season (Figure 4.3). However, the Chl-a concentration in January cannot be measured clearly due to broad cloud coverage. For example, the high Chl-a concentration in April is observed at the river mouth in Papua, where the highest concentration is found near the Digul River mouth (see river location in Appendix A). In July, the Chl-a bloom near the Digul River mouth decreases, and it is shifted offshore and

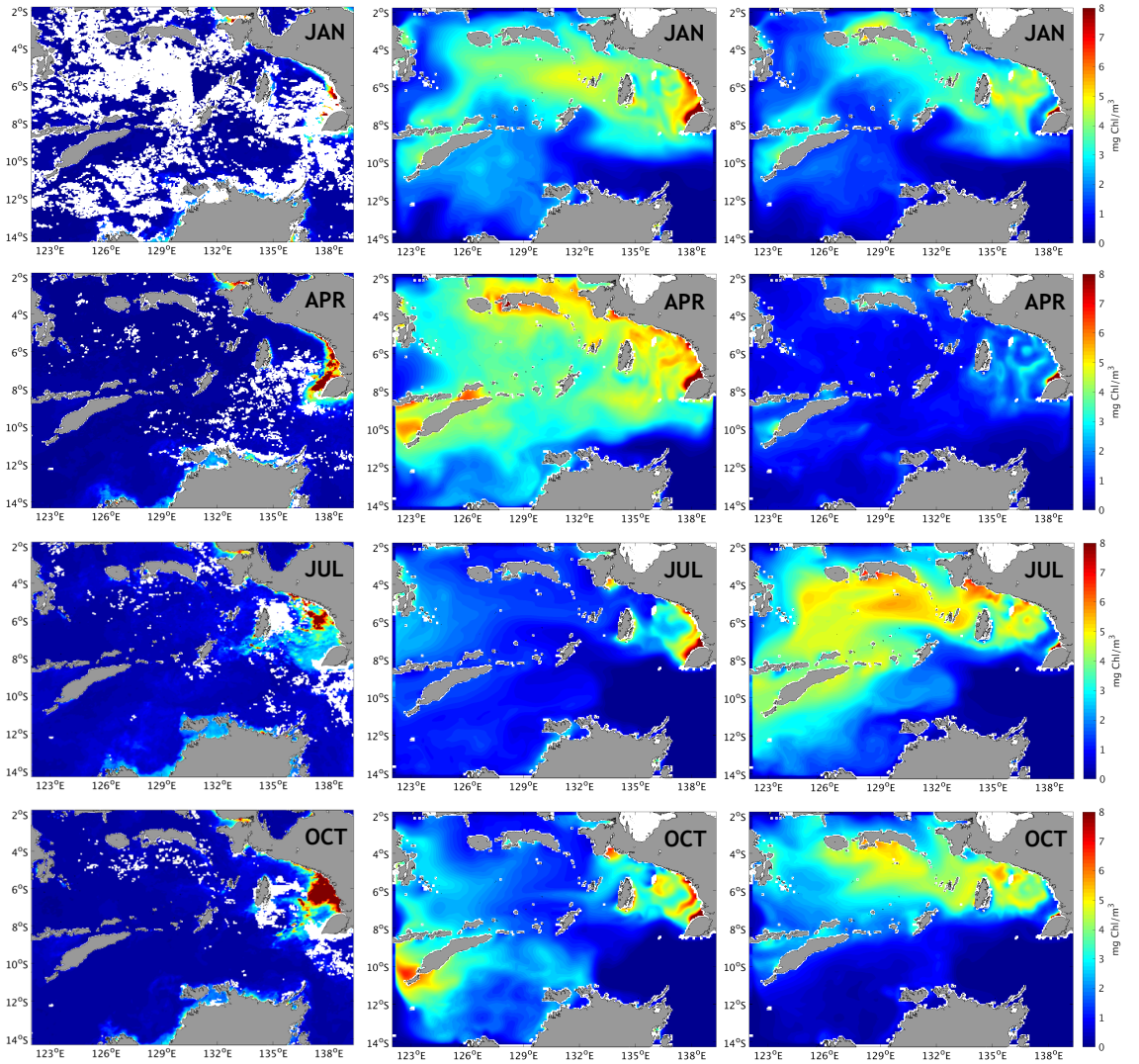

Figure 4.3: Spatial distribution of surface chlorophyll-a in January, April, July, and October 2014 from satellite observation (left), scenario 1 (middle), and scenario 2 (right).

northward. The northward Chl-a blooms are expected to be the result of upwelling in the northern Arafura Sea, as shown by *Basit* (2020). Furthermore, in October, the Chl-a concentration seems to increase in both magnitude and area coverage.

The simulations with scenarios 1 and 2 in January show an overestimated Chl-a concentration in the Arafura and Banda Seas. Additionally, both simulations show the bloom near the Digul River mouth, in which scenario 1 simulates a broader bloom coverage than scenario 2. Scenario 1 in April shows that high Chl-a not only spreads to the western Banda Sea but also to the Timor Sea (the location of Timor Sea is shown by Figure 3.1). Some blooms are also found on the northern coast of Papua, and in the Ceram and Savu Seas. By contrast, scenario 2 shows the only bloom found at Digul River mouth, which is confirmed by satellite observations (Figure 4.3).

In July, simulated Chl-a concentration from scenario 1 shows a similar spatial distribution to satellite-derived Chl-a concentration (Figure 4.3). The Chl-a bloom of scenario 1 is found in the Sahul Shelf, specifically along the Papua Coast.

Meanwhile, Chl-a concentration in the Banda Sea is very low. By contrast, scenario 2 overestimates the Chl-a concentration in both the Banda and Timor Seas. In October, the scenario 2 result also shows an overestimated Chl-a concentration in these regions.

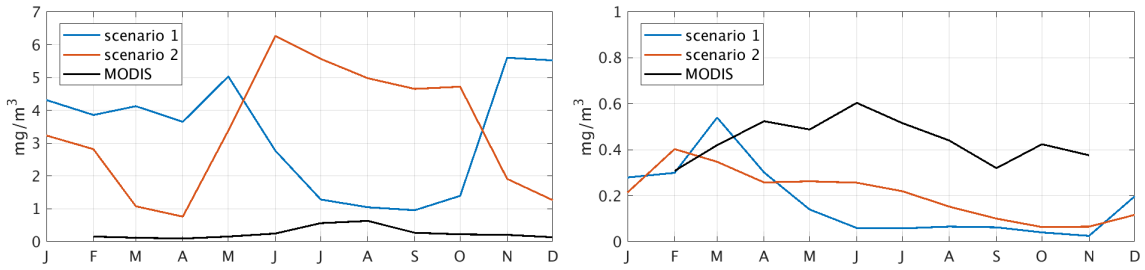

Figure 4.4: Monthly time series of surface chlorophyll-a at station A4 Banda Sea (left) and C4 Arafura Sea (right) from model results and satellite MODIS observation. The location of stations A4 and C4 is shown by Figure 3.5.

To investigate the seasonal variation, the monthly time series of surface Chl-a concentration at two stations are presented (Figure 4.4). In general, both scenario simulations overestimate Chl-a concentration at station A4 all year round. Figure 4.4 left shows that the observed Chl-a concentration in the Banda Sea is relatively low, less than 1 mg/m^3. The Chl-a concentration increases during the SE monsoon and reaches the maximum in August. A similar profile is shown by scenario 2. However, the Chl-a concentration increases earlier in April and decreases in October. The opposite profile is shown by scenario 1 where the Chl-a concentration decreases during the SE monsoon.

The monthly time series of satellite-derived Chl-a concentration at station C4 shows that the Chl-a concentration is relatively low for a whole year. The satellite-derived Chl-a concentration increases by 0.3 mg/m^3 from February to June. In June, the Chl-a concentration reaches the maximum, and from June to September the Chl-a concentration decreases. However, the time series of the satellite-derived Chl-a concentration is not represented well by the simulations. Both scenario 1 and 2 simulations underestimate the Chl-a concentration at station C4. Scenario 1 simulation shows that Chl-a concentration decreases from May to June, and is relatively constant until November. Furthermore, scenario 2 simulation shows the decrease of Chl-a concentration earlier in February until October.

Based on the validation of simulated Chl-a, it can be concluded that scenario 2 has a similar seasonal variation to observations. Even though scenario 2 overestimates surface Chl-a, it reproduces the seasonal cycle better than scenario 1 at both stations. Therefore, from this section onwards, the results of the scenario 2 simulation are used for further analysis. In the following sections onwards, the term 'simulation' refers to the scenario 2 simulation.

4.2.2 Vertical profile of nutrient

The nutrient output by ECOHAM, i.e., nitrate and phosphate, is compared to observational data from in-situ measurements. The nutrients data from in-situ measurements in the Arafura and Banda Seas in 2014 are available. However, the locations of in-situ measurement are outside the ECOHAM domain, so that it can not be used for model validation. Therefore, the monthly ECOHAM output of 2014 is compared to the available observations from another year. In this case, it is worth noting that the comparison between observations and model results will only focus on the specific month of interest.

Furthermore, the difference between the maximum and minimum nutrient concentration is calculated for the respective month, which is referred to as model *Range* (Equation 4.1). The model *Range* is calculated at each depth of the respective observational data. Accordingly, the nutrient variation in the specific month of interest can be analyzed.

$$Range(nut) = Max(nut) - Min(nut) \tag{4.1}$$

In the above Equation 4.1, *nut* refers to the simulated nutrient (nitrate or phosphate) concentration, $Max(nut)$ is the maximum nutrient concentration in one month, and $Min(nut)$ is the minimum nutrient concentration in one month. For example, the in-situ measurement at station C1 was conducted on 29 July 2013 (Table 3.2). Therefore, the model $Range(nut)$ is the maximum minus the minimum value of the simulated nutrient concentration in July 2014. For simplification, from this section onwards, the term $Range(nut)$ is replaced by *Range*.

1) Banda Sea

In general, the simulation results in the Banda Sea (Figure 4.6) show an increasing nitrate profile towards depth, confirmed by observations. For example, the observed nitrate concentration at station A1 measured on 3 March 1998, shows the rapid increase from 8 mmol N m^{-3} at the surface to 27 mmol N m^{-3} at 300 m depth. The nitrate concentration below 300 m slowly increases and reaches 32 mmol N m^{-3} at 1700 m depth. However, this observed nitrate profile is not well captured in the ECOHAM simulation results. At station A1, the simulation underestimates nitrate concentrations in the whole water column by 1–8 mmol N m^{-3}.

The model *Range* between 300 and 1700 m depth at station A1 is 1–5 mmol N m^{-3}, indicating relatively high variability in nitrate concentration. Moreover, the vertical profile of the simulated nitrate shows a minimum concentration between 300 and 400 m, implying nitrate being consumed/lost. Within this depth interval, where the light availability is low, the possibility of nitrate consumed by phytoplankton is also low.

The observational data at station A2 obtained on 2 March 1998, shows that nitrate concentration rapidly increases from ∼0.1 at the surface to 27 mmol N m^{-3} at 500 m. From 500 m to 1800 m, the nitrate concentration increases slowly. Figure 4.5 shows that the simulation slightly overestimates the nitrate concentration in the

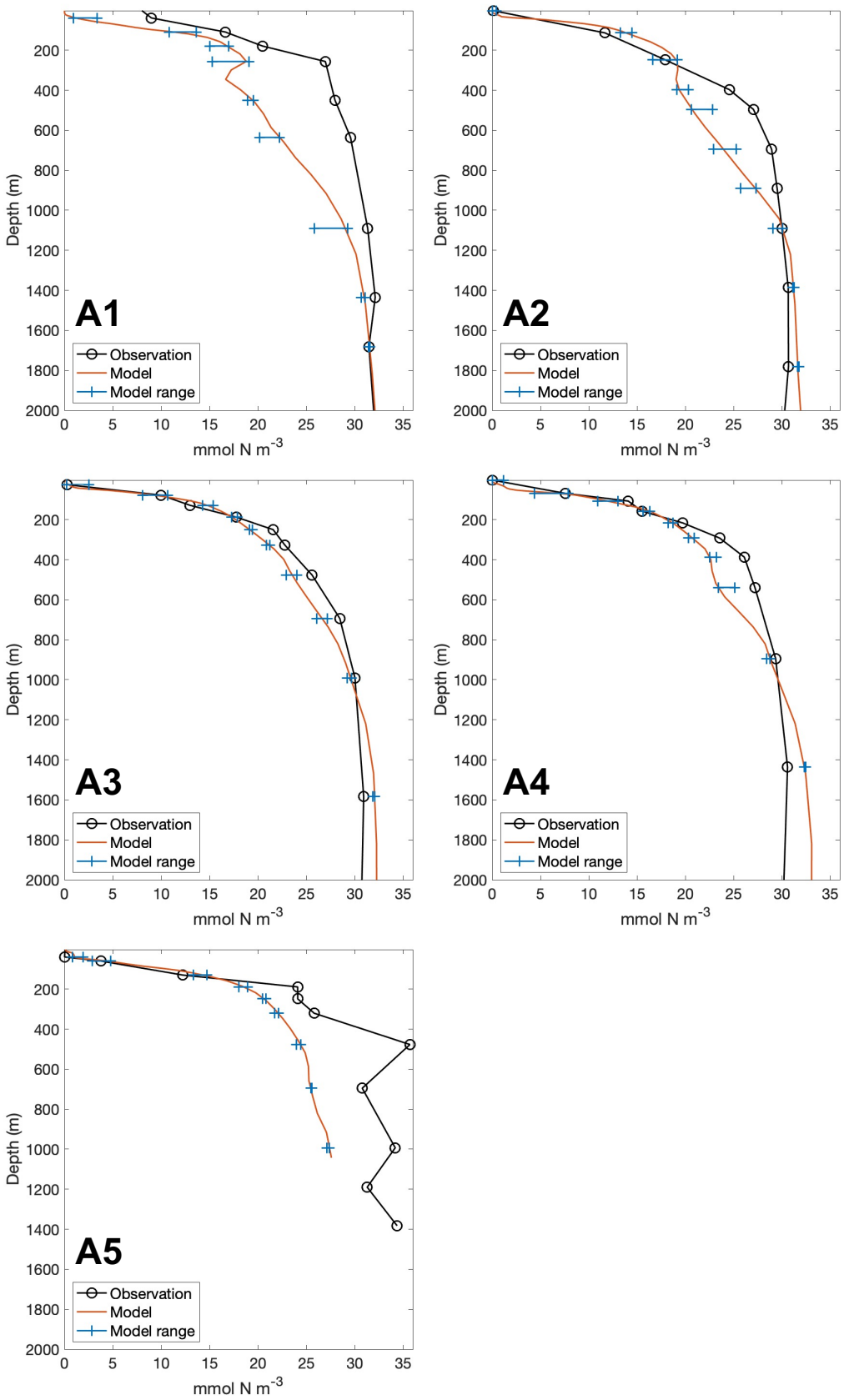

Figure 4.5: Comparison of the vertical profile of nitrate in the Banda Sea from observations and model results. The model *Range* is calculated from a one-month statistic of the respective month (Equation 4.1). The date of observation and location of stations A1–A5 are shown in Table 3.2 and Figure 3.5, respectively.

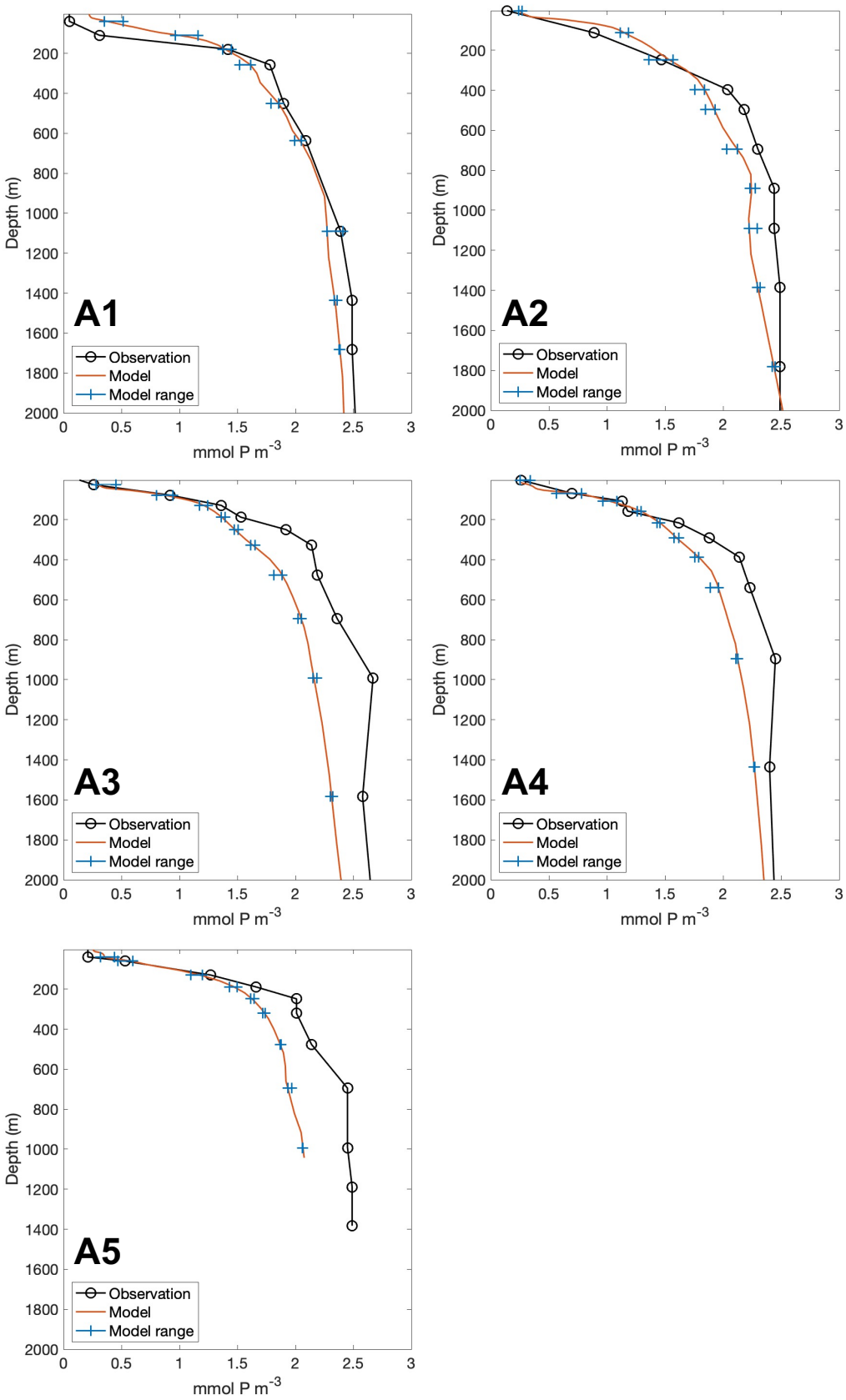

Figure 4.6: Comparison of the vertical profile of phosphate in the Banda Sea from observations and model results. The model *Range* is calculated from a one-month statistic of the respective month (Equation 4.1). The date of observation and location of stations A1–A5 are shown in Table 3.2 and Figure 3.5, respectively.

upper 300 m by 3 mmol N m^{-3}. Like station A1, the simulation also underestimates the nitrate concentration between 300 and 1100 m depth by 1–7 mmol N m^{-3}. Additionally, the model *Range* within these depth intervals is 1–3 mmol N m^{-3} which is smaller than at station A1, indicating a minor variation in nitrate.

Similar to station A2, the observational data at station A3 (obtained on 1 March 1998) also shows a low nitrate concentration at the surface, and it increases with depth. Compared to stations A1 and A2, the simulated nitrate concentration at station A3 fits the observation better, particularly in the upper 200 m (Figure 4.5). From 200 to 1000 m depth, the simulation underestimates the nitrate concentration by 1–2 mmol N m^{-3}. In this depth interval, the model *Range* is relatively small, reaching only 1 mmol N m^{-3}, indicating a less variable nitrate concentration than in the upper 200 m. Below 1000 m, the simulation overestimates the nitrate concentration by 2 mmol N m^{-3}.

At station A4, the in-situ measurement was conducted on 28 February 1998 (Table 3.2). Figure 4.5 shows that the simulation fits the observed nitrate concentration in the upper 200 m. However, from 200 m to 900 m depth, the simulation underestimates nitrate concentration by 1–4 mmol N m^{-3}. Similar to station A3, below 900 m, the simulation also overestimates the nitrate concentration by 3 mmol N m^{-3}.

Furthermore, the final station in the Banda Sea, station A5, is located close to the Aru Basin (Figure 3.5). Like station A4, the in-situ measurement at station A5 was also conducted on 28 February 1998. Figure 4.5 shows that the observed nitrate concentration below 200 m at station A5 shows a more variable concentration than other stations. The nitrate concentration very rapidly increases up to 36 mmol N m^{-3} from the surface to 500 m depth. However, below 500 m, the nitrate concentration decreases up to 30 mmol N m^{-3} at 700 m. Between 700 m and 1400 m depth, the observed nitrate concentration fluctuates between 30 and 35 mmol N m^{-3}. Additionally, the simulation at station A5 fits the observed nitrate concentration in the upper 200 m. Below 200 m, the simulation underestimates the nitrate concentration by 6–12 mmol N m^{-3}, which is the largest discrepancy among other stations. However, the model *Range* is small, less than 1 mmol N m^{-3}, indicating a less variable nitrate concentration in the whole water column.

Overall, the nitrate profiles in the Banda Sea show that the simulation underestimates the nitrate from 200 m to 1000 m depth, especially at stations A1 and A2. The nitrate concentration in the upper 200 m is more variable than in the layer below. Among all stations, station A5 shows the largest underestimated simulated nitrate concentration. Generally, the overall picture of a strong nitrate increase with depth can be reproduced by the simulation.

In addition to nitrate, the simulated phosphate concentration from ECOHAM is also compared to observations. Figure 4.6 shows that the observed phosphate concentration at all stations in the Banda Sea is found to be less than 2.5 mmol P m^{-3}. Figure 4.6 also shows that the observed phosphate concentration at station A1

is almost zero at the surface, and increases rapidly up to 1.8 mmol P m^{-3} at 300 m. From 300 m, phosphate concentration slowly increases to 2.5 mmol P m^{-3} at 1100 m depth. Below 1100 m depth, the observed phosphate concentration is relatively constant at 2.5 mmol P m^{-3}.

The simulation at station A1 overestimates the phosphate concentration by 0.2 mmol P m^{-3} in the upper 200 m. By contrast, below 200 m, the simulation underestimates the phosphate concentration by 0.1–0.3 mmol P m^{-3}. The previous discussion showed that the simulated nitrate concentration at station A1 has a minimum between 300 m and 400 m depth (Figure 4.5), implying nitrate being consumed/lost. However, this minimum is not found in the simulated phosphate profile (Figure 4.6). Moreover, the model *Range* in the upper 200 m is about 0.3 mmol P m^{-3}, which is larger than below 200 m (< 0.1 mmol P m^{-3}), indicating a more varying phosphate concentration.

The observed phosphate concentration at the surface at station A2 is about 0.2 mmol P m^{-3}, and rapidly increases to 2 mmol P m^{-3} at 400 m. Similar to station A1, the simulation also overestimates phosphate concentration in the upper 300 m by 0.2 mmol P m^{-3}. However, below 300 m, the simulation underestimates phosphate concentration by 0.1–0.3 mmol P m^{-3}. The model *Range* is about 0.1–0.3 mmol P m^{-3}, where the maximum is found at 300 m depth, indicating the highest variation in subsurface phosphate at this depth.

Other phosphate measurement stations are located in the central Banda Sea, represented by stations A3 and A4. The observed phosphate concentration at stations A3 and A4 at the surface is about 0.2 mmol P m^{-3}. Moreover, the observed phosphate concentration rapidly increases up to 2.1 mmol P m^{-3} at 300 m at station A3 and at 400 m at station A4, respectively. From 300 m, the observed phosphate concentration at station A3 slowly increases up to 2.7 mmol P m^{-3} at 1000 m. However, the observed phosphate concentration slightly decreases to 2.6 mmol P m^{-3} at 1600 m depth. Similar to station A3, the observed phosphate concentration at station A4 slowly increases to 2.5 mmol P m^{-3} in 900 m, and decreases to 2.4 mmol P m^{-3} in 1400 m depth. Overall, the simulation fits the observed phosphate in the upper 200 m at both stations and underestimates phosphate concentration below 200 m by 0.1–0.5 mmol P m^{-3}. Similar to station A1, the model *Range* in the upper 200 m is 0.1–0.3 mmol P m^{-3}, which is larger than below 200 m, indicating a stronger variability in phosphate.

Moving to the eastern Banda Sea, station A5 shows that the observed phosphate concentration rapidly increases to 2 mmol P m^{-3} at 200 m depth. From 200 m to 1400 m, the observed phosphate concentration increases slowly. Unlike the nitrate profile (Figure 4.5), there are no phosphate jumps between 500 m and 1400 m depth (Figure 4.6). Like stations A3 and A4, the simulation also shows a good fit with the observed phosphate concentration in the upper 200 m. Below 200 m, the simulation underestimates phosphate concentration by 0.1–0.5 mmol P m^{-3}. Additionally, the model *Range* below 200 m (< 0.1 mmol P m^{-3}) is smaller than in the upper 200 m (± 0.3 mmol P m^{-3}), indicating a minor variation in phosphate.

In general, according to the vertical profile of nutrients shown in Figures 4.5 and 4.6, ECOHAM simulation shows a good fit with the observations in the upper 200 m. Nevertheless, the simulation underestimates both nitrate and phosphate below 200 m depth. Furthermore, the simulation also shows that nitrate is more variable than phosphate. Notably, at stations A1 and A2, the model *Range* of the simulated nitrate concentrations for the whole water column are larger than at other stations, indicating that nitrate is highly variable.

Additionally, the phosphate concentration in the near-surface layer at station A1 is depleted, although the nitrate concentration is relatively high (8 mmol N m^{-3}). This condition indicates that the western Banda Sea near the surface is phosphate-limited because phosphate is consumed by phytoplankton while nitrate remains abundant. On the contrary, the phosphate concentration near the surface at stations A2–A5 is about 0.3 mmol P m^{-3} while nitrate vanishes, indicating that these locations are nitrate-limited. Thus, overall, the near-surface layer in the Banda Sea is nitrate-limited, which agrees with the study by *Zevenboom and Wetsteyn* (1990).

2) Timor and Arafura Seas

Unlike for the Banda Sea, the observed nutrient profiles in Timor and Arafura Seas at all stations are relatively homogenous (Figure 4.7 and 4.8). Homogenous nutrient profiles are related to shallow bathymetry and strong tidal mixing. According to *Condie* (2011), the Timor and Arafura Seas are dominated by large tides.

The in-situ measurements at stations C1–C3 and C4–C5 were conducted in July 2013 and October 2012, respectively (Table 3.2). In general, the nitrate concentrations in Timor and Arafura Seas in July and October are small (< 1 mmol N m^{-3}), indicating oligotrophic conditions in this area during SE and second transition monsoons, but possibly all seasons. At station C1, the observed nitrate concentration from the surface to 120 m depth slightly increases from 0.6 to 0.8 mmol N m^{-3}. Unlike observations, the simulated nitrate concentration shows a more stratified profile, in which the concentration increases to 1.5 mmol N m^{-3} from the surface to 80 m depth. The simulation underestimates nitrate concentration by 0.5 mmol N m^{-3} in the upper 30 m and overestimates it by about 1 mmol N m^{-3} in the layer below. Additionally, the model *Range* at station C1 is $\sim$1 mmol N m^{-3}, which is the largest among other stations.

At station C2, the in-situ measurement was conducted on 30 July 2013 (Table 3.2). Figure 4.7 shows that the observed nitrate concentration at station C2 is lower than at station C1. Moreover, the observed nitrate in the upper 10 m is relatively constant (0.1 mmol N m^{-3}), while from 10 to 20 m, it increases to 0.3 mmol N m^{-3}. On the other hand, the simulation shows a homogeneous nitrate concentration of 0.08 mmol N m^{-3} from the surface to 40 m depth with the model *Range* of 0.1 mmol N m^{-3}.

Like station C2, the nitrate measurement at station C3 was also conducted on 30 July 2013. The observed nitrate concentration shows a constant value of 0.38

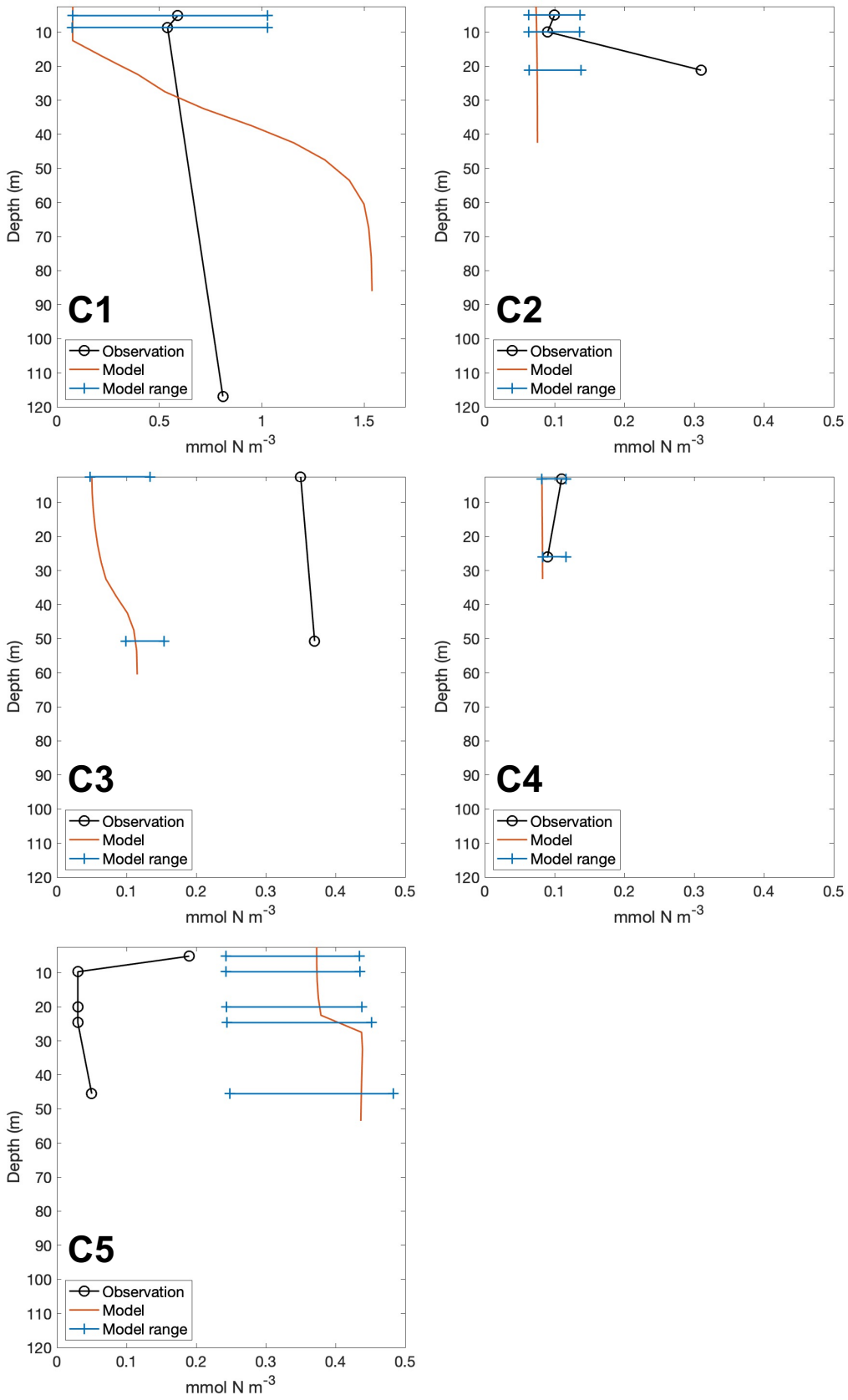

Figure 4.7: Comparison of the vertical profile of nitrate in the Timor and Arafura Seas from observations and model results. The model *Range* is calculated from a one-month statistic of the respective month (Equation 4.1). The date of observation and location of stations C1–C5 are shown in Table 3.2 and Figure 3.5, respectively.

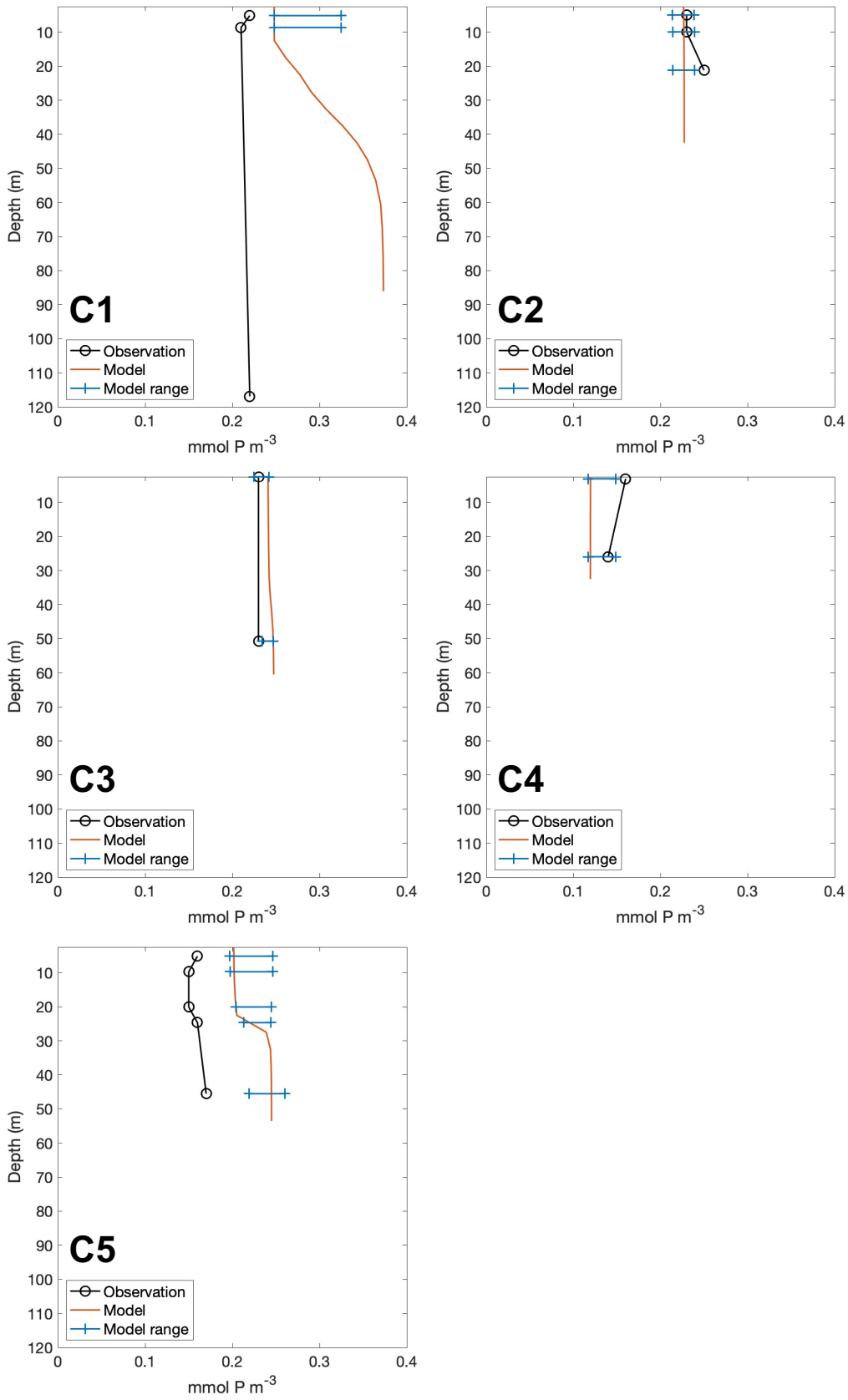

Figure 4.8: Comparison of the vertical profile of phosphate in the Timor and Arafura Seas from observations and model results. The model *Range* is calculated from a one-month statistic of the respective month (Equation 4.1). The date of observation and location of stations C1–C5 are shown in Table 3.2 and Figure 3.5, respectively.

mmol N m^{-3} from the surface to 50 m depth. The simulation underestimates nitrate concentration by 0.3 mmol N m^{-3} for the whole water column. Similar to station C2, the model *Range* at station C3 is 0.1 mmol N m^{-3}.

Other observational stations are located in the eastern part of the Arafura Sea, represented by stations C4 and C5 (Figure 3.5). The in-situ measurements at stations C4 and C5 were conducted on 17 and 18 October 2012, respectively (Table 3.2). The observed nitrate concentration at station C4 is about 0.12 mmol N m^{-3} at the surface and decreases slightly to 0.1 mmol N m^{-3} at 27 m depth. Additionally, the simulation slightly underestimates the nitrate concentration by 0.02 mmol N m^{-3}.

Furthermore, the observed nitrate concentration at station C5 is 0.2 mmol N m^{-3} at the surface and it decreases to 0.03 mmol N m^{-3} at 10 m depth. The observed nitrate concentration is constant until 25 m, and then it slightly increases to 0.05 mmol N m^{-3} at 46 m depth. Different from observations, the simulated nitrate concentration at station C5 shows an increasing profile towards depth, and it overestimates nitrate concentration by 0.2–0.4 mmol N m^{-3}. Additionally, the model *Range* is about 0.2 mmol N m^{-3} for the whole water column, indicating a higher variation in nitrate at station C5 than at stations C2–C4.

Like the nitrate profile, the observed phosphate in Timor and Arafura Seas is also homogeneous (Figure 4.8). Station C1 shows a constant phosphate concentration of 0.22 mmol P m^{-3} from the surface to 120 m depth. However, the simulation overestimates the phosphate concentration, and it shows a more stratified profile. The simulated phosphate concentration increases from 0.25 mmol P m^{-3} to 0.37 mmol P m^{-3} at 60 m depth. Below 60 m, the simulated phosphate concentration is constant.

Similar to station C1, the observed phosphate concentration at station C2 is about 0.23 mmol P m^{-3} at the surface, and it slightly increases to 0.25 mmol P m^{-3} at 20 m depth. The simulation fits the observed phosphate concentration in the upper 10 m. Below 10 m, the simulation underestimates phosphate concentration by 0.03 mmol P m^{-3}. Moving to the east, at station C3 the observed phosphate concentration is relatively constant of 0.23 mmol P m^{-3} for the whole water column. The simulation slightly overestimates phosphate concentration for the whole water column by 0.15 mmol P m^{-3}.

At station C4, the observed phosphate concentration is about 0.16 mmol P m^{-3} at the surface, and it slightly decreases to 0.14 mmol P m^{-3} at 27 m depth. The simulation underestimates the phosphate concentration at station C4 by 0.03–0.05 mmol P m^{-3}. The last station in the Arafura Sea, station C5 shows that the observed phosphate concentration is 0.16 mmol P m^{-3} near the surface, and it decreases to 0.15 at 20 m. However, the observed phosphate concentration increases to 0.17 mmol P m^{-3} at 47 m depth. The simulation overestimates the phosphate concentration at station C5 by 0.04–0.08 mmol P m^{-3}. The model *Range* is about 0.04 mmol P m^{-3}, indicating more variable phosphate than at station C4.

Overall, Figures 4.8 and 4.9 show that nutrient concentrations in Timor and

Arafura Seas are very low. Its vertical profiles are also relatively homogeneous and very low, indicating an oligotrophic area. The ECOHAM simulation reproduced this homogeneous profile quite well, except at station C1, where the simulation shows a stratified profile. Moreover, the nutrient concentrations (nitrate and phosphate) are much lower than in the Banda Sea.

4.3 ECOHAM sensitivity tests

As previously described in Section 3.2, ECOHAM was initially used for biogeochemical studies in the North Sea. ECOHAM has been mainly applied to areas at higher latitudes ever since. However, since ECOHAM is implemented at lower latitudes in this study, especially in tropical seas, some parameters need to be adjusted. Therefore, it is important to investigate how the simulation results change with the different parameters by conducting sensitivity tests. In principle, the sensitivity tests evaluate how "sensitive" the model is to variations in the parameters and data on which it is built (*Salciccioli et al.*, 2016).

Table 4.1: The parameters for the sensitivity tests.

Sensitivity runs	Parameter (p)	Unit	Standard value (p_s)	Plus 10%	Minus 10%
a, b	silt	g m^{-3}	1	1.1	0.9
c, d	Q_{10} for phytoplankton	dimensionless	1.1	1.2	1.0
e, f	Q_{10} for zooplankton	dimensionless	1	1.1	0.9
g, h	K_1	mmol N m^{-3}	0.5	0.55	0.45

Note: Sensitivity runs a and b refer to the sensitivity runs with silt concentrations of 1.1 and 0.9 g m^{-3}, respectively. The same rule applies to the second row, etc.

For the sensitivity tests, some parameters based on the limiting factors of phytoplankton growth are chosen (Table 4.1). There are three main factors, i.e., temperature, light, and nutrients. Temperature affects the rate of phytoplankton growth and it is expressed by temperature coefficient Q_{10} (Equation 3.9). In addition to phytoplankton, the temperature coefficient for zooplankton growth is also chosen for the sensitivity tests. The second limiting factor for the phytoplankton growth is light, which is affected by silt and chlorophyll concentrations, including by the extinction coefficient of water (Equations 3.11 and 3.12). For the sensitivity tests, the effect of light is represented by silt concentration. Finally, to investigate the effect of nutrients, the half-saturation constant for nitrate uptake by phytoplankton K_1 is chosen (Equations 3.20 and 3.22). There are eight sensitivity runs using four parameters, with ranges of plus-minus 10% around their standard value (Table 4.1).

The effect of the sensitivity parameter p is quantified by a normalized sensitivity function $S(p)$. The equation of normalized sensitivity is adapted from *Fasham et al.*

(1990) as shown in Equation 4.2. In the following section, the sensitivity analysis is focused on the Redfield carbon fixation (Equation 3.26). The latter will be referred to as NPP Redfield, which is the sum of NPP Redfield of diatoms and non-diatoms.

$$S(p) = \left(\frac{\bar{x}(p) - \bar{x_s}}{\bar{x_s}}\right) \Big/ \left(\frac{p - p_s}{p_s}\right) \tag{4.2}$$

In the above Equation 4.2, $\bar{x_s}$ is the annual mean NPP Redfield for a standard run with a standard parameter value p_s and $\bar{x}(p)$ is the annual mean NPP Redfield for the sensitivity run with the sensitivity parameter value p (+10 and -10%). Note that both the numerator and denominator terms in Equation 4.2 could be negative or positive. Therefore, the value of $S(p)$ could be negative or positive, depending on whether the sensitivity parameter p decreases or increases the NPP Redfield.

4.3.1 Temporal variation of NPP Redfield

The following section focuses on the NPP Redfield differences between the standard and sensitivity runs, primarily the temporal variation. The time series at three stations located in the Arafura and Banda Seas are presented to investigate the temporal variation of the NPP Redfield for each sensitivity run (Figure 4.9).

Station A4 in the Banda Sea shows the largest NPP Redfield value, whereas station C3 shows the lowest value. During the NW monsoon, NPP Redfield of the standard run at station A4 ranges from 30 to 78 mmol C m^{-2} d^{-1} in February. From February, the NPP Redfield decreases and reaches the minimum of 20 mmol C m^{-2} d^{-1} in April. From April, the NPP Redfield rapidly increases up to 80 mmol C m^{-2} d^{-1} in early June. The rapid increase of the NPP Redfield during this period indicates that the nutrients, light availability, and temperature are optimal to support phytoplankton production. From June to September, the NPP Redfield ranges from 70 to 90 mmol C m^{-2} d^{-1}. NPP Redfield at station A4 reaches the maximum of 103 mmol C m^{-2} d^{-1} in mid-October. However, from mid-October to the beginning of November, the NPP Redfield rapidly decreases to 40 mmol C m^{-2} d^{-1}.

At station B1, the NPP Redfield of the standard run is smaller than at station A4, ranging from 18 to 63 mmol C m^{-2} d^{-1}. At station B1, the NPP Redfield reaches the minimum at the end of April. From May to the end of June, the NPP Redfield increases up to 40 mmol C m^{-2} d^{-1}. In July, the NPP Redfield increases until it reaches the maximum of 63 mmol C m^{-2} d^{-1} in mid-October.

The final station C3 shows the lowest NPP Redfield for both standard and sensitivity runs. The low NPP Redfield may relate to low nutrient concentrations at station C3 as described in Section 4.2.2. At station C3, the NPP Redfield of the standard run ranges from 3 to 24 mmol C m^{-2} d^{-1}. The NPP Redfield is high during the SE monsoon and it reaches the maximum at the end of August. By contrast, the NPP Redfield is low during the NW monsoon, where the minimum is found in December.

In general, the NPP Redfield of each sensitivity run has the same temporal

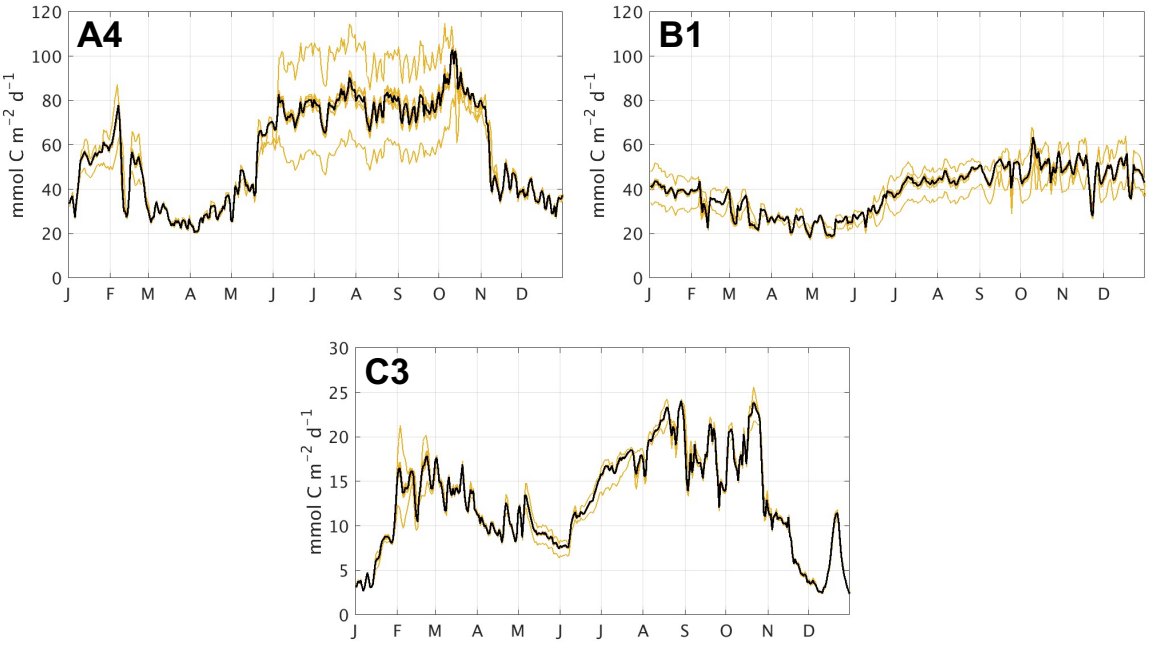

Figure 4.9: Time series of the vertically integrated NPP Redfield at stations A4, B1, and C3 (Figure 3.5). The black and yellow lines indicate the standard and sensitivity runs, respectively.

variation as the standard run. The sensitivity runs do not alter the temporal variation but rather the magnitude of NPP Redfield. Moreover, six out of eight sensitivity runs produced a relatively small deviation of the NPP Redfield from the standard run, while two sensitivity runs produced the highest deviation. The highest deviation of NPP Redfield results from sensitivity runs *c* and *d*, which is the simulation with different Q_{10} values for phytoplankton (Table 4.1). The maximum and minimum NPP Redfield values are associated with the +10% and -10% of Q_{10} phytoplankton, respectively.

Additionally, the deviation is related to the magnitude of NPP Redfield, where a larger magnitude has a larger deviation and vice versa. For example, at station A4, the largest deviation is found from June to mid-October, associated with the high NPP Redfield value. The deviation is ±20 mmol C m^{-2} d^{-1} during this period, which is about 25% from the NPP Redfield of the standard run. By contrast, the deviation is small from March to May, associated with the low NPP Redfield of the standard run. Moreover, the largest deviation of the sensitivity runs at station B1 is about 25% or ±10 mmol C m^{-2} d^{-1} from July to December and January to February. Meanwhile, at station C3, the largest deviation is found in February, which reaches up to ±5 mmol C m^{-2} d^{-1}.

Based on the temporal variation of the NPP Redfield, it is found that the 10% change in sensitivity parameters (Table 4.1) does not affect the temporal variation but affects the magnitude. The simulation reveals that the highest deviation of the NPP Redfield results from sensitivity runs *c* and *d*, with parameter Q_{10} for phytoplankton. Generally, a 10% change in Q_{10} for phytoplankton can significantly change the NPP

Redfield value by up to 25%.

4.3.2 Spatial distribution of normalized sensitivity

The effect of the sensitivity parameters on NPP Redfield is quantified by the normalized sensitivity function $S(p)$ as shown in Equation 4.2. The spatial distribution of $S(p)$ for each sensitivity run is presented by Figure 4.10. For example, Figure 4.10a shows that the $S(p)$ values for sensitivity run a are negative in most areas. It suggests that the numerator in Equation 4.2 is negative, while the denominator is positive. Therefore, a negative $S(p)$ indicates that the higher (+10%) silt concentration reduces the annual mean NPP Redfield. This is the expected result because a higher silt concentration will reduce the light penetration through the water column. Hence, phytoplankton production decreases, and phytoplankton growth is suppressed.

The same principle applied for sensitivity run b with -10% silt concentration. For -10% silt concentration, the denominator in Equation 4.2 is negative. However, the numerator is positive because a lower silt concentration leads to a higher phytoplankton production. As a result, $S(p)$ values are negative in most areas, as shown in Figure 4.10b. However, $S(p)$ values in the northern coast of Australia, the western coast of Papua, and the eastern Aru Islands, are positive (Figures 4.10a, b). In these areas, the decrease of silt concentration increases the annual mean NPP Redfield and vice versa.

The second sensitivity parameter is the temperature factor Q_{10} for phytoplankton growth, which is represented by sensitivity runs c and d (Table 4.1). As shown in Figure 4.10c, a higher Q_{10} phytoplankton increases NPP Redfield, indicated by positive $S(p)$ values in most areas. By contrast, a lower Q_{10} decreases NPP Redfield, which is also indicated by positive $S(p)$ values as shown in Figure 4.10d. In principle, a higher Q_{10} leads to a higher rate of phytoplankton growth. As a result, phytoplankton consumes more nutrients and increases production.

Additionally, the $S(p)$ values from sensitivity runs c and d are about ten times higher than the $S(p)$ value from the rest of the sensitivity runs. In fact, this is a reasonable result since the NPP Redfield from the sensitivity runs c and d have the highest deviation from the standard run (see Section 4.3.1). However, similar to $S(p)$ values of sensitivity runs a and b, some areas in the northern coast of Australia, the western coast of Papua, and the eastern Aru Islands, show an opposite $S(p)$ value. In these areas, $S(p)$ is negative, indicating that the higher Q_{10} for phytoplankton leads to lower NPP Redfield and vice versa.

The third sensitivity parameter is Q_{10} for zooplankton which exemplifies the impact of the grazing. It is represented by sensitivity runs e and f (Table 4.1). Compared to the last two parameters (silt and Q_{10} for phytoplankton), the $S(p)$ values of the sensitivity runs e and f, vary more spatially. Figures 4.10e and f show that the Arafura and Banda Seas exhibit different $S(p)$ values. For example, the +10%

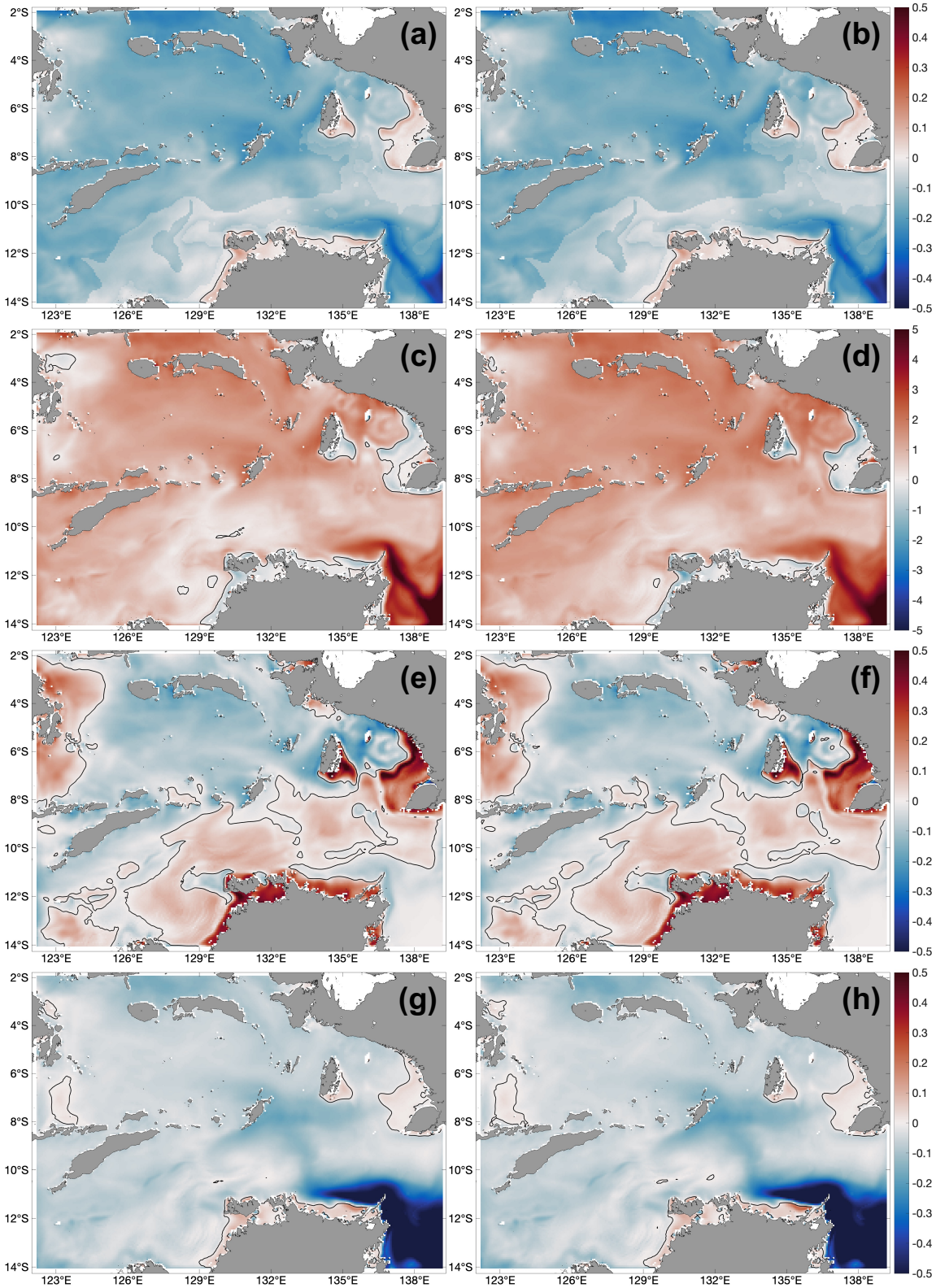

Figure 4.10: Spatial distribution of normalized sensitivity $S(p)$ for NPP Redfield with sensitivity parameter of (a) +10% silt; (b) -10% silt; (c) +10% $Q10$ for phytoplankton; (d) -10% $Q10$ for phytoplankton; (e) +10% $Q10$ for zooplankton; (f) -10% $Q10$ for zooplankton; g) +10% K_1; (h) -10% K_1 value (Table 4.1). Red and blue colors indicate positive and negative values. Black contours indicate zero values.

Q_{10} for zooplankton reduces NPP Redfield in the Banda Sea and the southeastern Arafura Sea, indicated by negative $S(p)$ values in Figure 4.10e. In principle, this is a reasonable result because a higher Q_{10} for zooplankton leads to a higher zooplankton growth rate. Hence, the zooplankton concentration also increases. Consequently, the increase in zooplankton grazing is reducing the phytoplankton concentration. However, positive $S(p)$ values in the Arafura Sea, the northern coast of Australia and the eastern Timor Sea indicate that a higher Q_{10} for zooplankton increases NPP Redfield and vice versa.

The final parameter for the sensitivity test is the half-saturation constant for nitrate or K_1, represented by sensitivity runs g and h (Table 4.1). Most areas show negative $S(p)$ values, indicating that a higher K_1 leads to a lower NPP Redfield and vice versa (Figures 4.10g, h). A higher K_1 indicates that phytoplankton requires a higher nitrate concentration to reach half of the maximum growth rate. As a result, in an environment with the same nitrate concentration, phytoplankton with a higher K_1 has a lower growth rate. Hence, the NPP Redfield also decreases. However, the northern coast of Australia, the western coast of Papua, the eastern Aru Islands, and a region in the west of Banda Sea show positive $S(p)$ values (Figures 4.10g, h). A positive $S(p)$ value indicates that a higher K_1 leads to higher NPP Redfield.

In general, each sensitivity parameter affects NPP Redfield differently. For example, a higher silt, K_1, and Q_{10} for zooplankton value mainly reduces NPP Redfield and vice versa. On the other hand, a higher Q_{10} for phytoplankton, represented by sensitivity run c, increases NPP Redfield. The $S(p)$ values of sensitivity runs c and d also show the largest values among other sensitivity runs. However, the northern coast of Australia, the western coast of Papua, and the eastern Aru Islands exhibit the opposite $S(p)$ values. For example, in these areas, the higher and lower Q_{10} for phytoplankton decreases and increases the NPP Redfield value, respectively. The following section will discuss the possible cause for such opposing behavior of $S(p)$ values.

Figure 4.11 shows the annual mean NPP Redfield (integrated vertically) from the standard run in region B (see square B in Figure 3.5). According to Figure 4.11, NPP Redfield is high in the northern Arafura Sea, the Aru Basin, and the Digul River mouth. However, NPP Redfield in the western coast of Papua (around 137–138° E and 6–8.5° S) and the eastern Aru Islands is very low throughout the year, indicated by the blue color.

In general, physical condition of the water body, such as light penetration and temperature, affects NPP Redfield. Notably, the western coast of Papua receives significant freshwater input from rivers. As a result, the surface density along the coast is very low, close to freshwater density, as shown in Figure 4.12a. Furthermore, Figure 4.12b shows that the temperature factor around the low-density area (137–138° E and 6–8.5° S) is higher than the value around it. However, the temperature factor decreases in the western part (134–137° E) and the south of the Aru Islands. Additionally, the light-depending growth rate for phytoplankton (F_{par}) is relatively higher in the northern Arafura Sea, as shown in

Figure 4.12c. The highest F_{par} value is found at the Digul River mouth, and it slightly decreases in the western part (134–137° E).

The simulation reveals that the river input slightly increases the Q_{10}, particularly on the western coast of Papua. It suggests that the temperature drives the phytoplankton growth rate to be faster. On the other hand, the light-dependent growth rate F_{par} is also higher on the western coast of Papua, specifically near the Digul River mouth. According to these results, it can be concluded that the river input changes the physical conditions but does not necessarily inhibit the phytoplankton growth and production. Therefore, the physical condition is not the main factor affecting the $S(p)$ values.

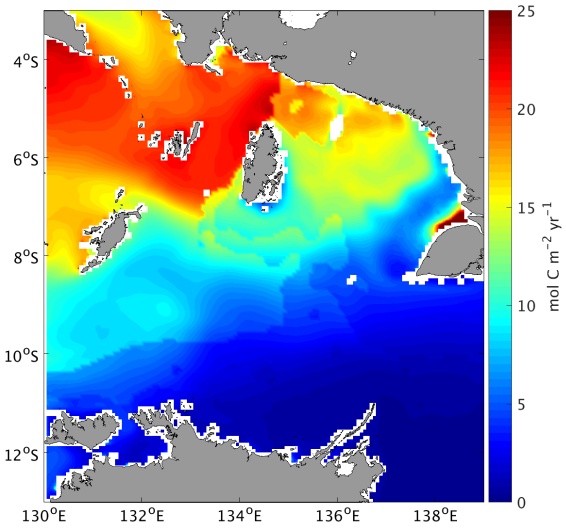

Figure 4.11: The annual mean NPP Redfield (integrated vertically) for the standard run in region B (Figure 3.5). Note that the unit is expressed in mol C m^{-2} yr^{-1}.

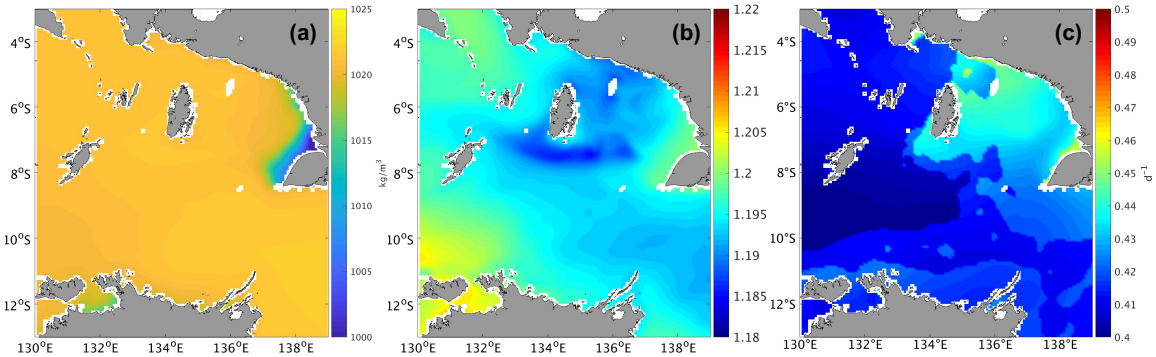

Figure 4.12: The annual mean of (a) density; (b) temperature factor Q_{10}; (c) light-depending growth rate F_{par} (Equation 3.10) at the surface in region B (Figure 3.5).

In addition to the physical condition, the nutrient concentrations of nitrate and ammonium, also affect NPP Redfield. As shown in Figures 4.13a and b, the limiting factors of nitrate ($lip1\_n3$) and ammonium ($lip1\_n4$) for diatoms are relatively low. For example, Figure 4.13a shows that the $lip1\_n3$ value is less than 0.5, where the minimum (≤ 0.1) is found in the northern coast of Australia, the western coast of

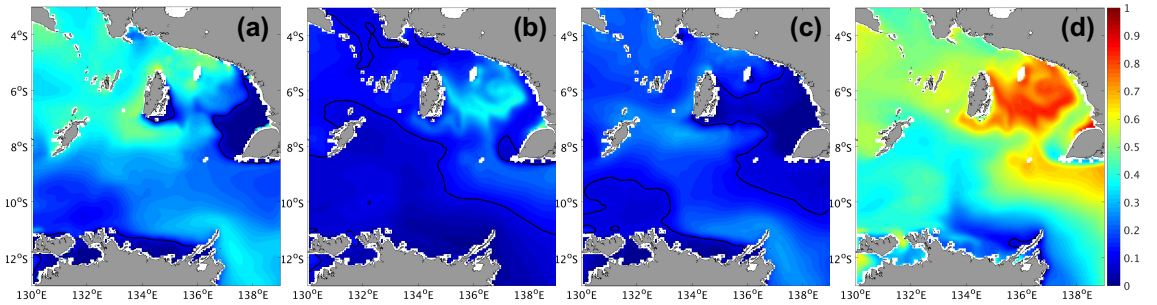

Figure 4.13: The annual mean of the limiting factor of (a) nitrate for diatoms ($lip1\_n3$); (b) ammonium for diatoms ($lip1\_n4$); (c) nitrate for non-diatoms ($lip2\_n3$); (d) ammonium for non-diatoms ($lip2\_n4$) at the surface in region B (Figure 3.5). Black contours indicate the value of 0.1. The limiting factors of nitrate and ammonium are described in Equations 3.20–3.23.

Papua, and the eastern Aru Islands. It appears that these regions with minimum $lip1\_n3$ values also exhibit the negative $S(p)$ values in the sensitivity runs c and d in Figure 4.10.

Furthermore, Figure 4.13c shows that the nitrate limitation factor for non-diatoms ($lip2\_n3$) is generally lower than for diatoms. By contrast, the ammonium limitation factor for non-diatoms ($lip2\_n4$) is high, as shown in Figure 4.13d. As described in Section 3.2.3.1, the half-saturation constant of ammonium uptake by non-diatoms is lower than for nitrate. Hence, the non-diatoms take up ammonium preferably. Also, a small ammonium concentration can still support the non-diatoms growth during nutrient-depleted conditions. The results indicate that nitrogen is more limiting to diatoms growth than non-diatoms. In other words, diatoms take up less nitrogen in nitrogen-depleted conditions, and diatoms growth is more likely suppressed than for non-diatoms.

According to Figure 4.13, the northern coast of Australia, the western coast of Papua, and the eastern Aru Islands exhibit a strong nitrate limitation for diatoms, indicated by low $lip1\_n3$ values. In these particular regions, when Q_{10} increases by 10% (sensitivity run c), the rate of diatoms growth increases, and diatoms consume more nutrients (nitrate and ammonium). As a result, nutrients decrease rapidly, and this condition leads to a reduction of diatom concentration. A low diatom concentration suggests a low NPP Redfield. For this reason, the annual mean NPP Redfield from the sensitivity run c is also lower. It is the opposite for most areas in the Arafura and Banda Seas, which show a higher NPP Redfield from the sensitivity run c, resulting in positive $S(p)$ values (Equation 4.2). However, in the area with a strong nutrient limitation, the annual mean NPP Redfield is lower, which means the numerator of Equation 4.2 is negative, while the denominator is positive. Therefore, it produces negative $S(p)$ values, which oppose $S(p)$ values in most Arafura and Banda Seas areas.

As for non-diatoms, when Q_{10} for phytoplankton increases by 10% (sensitivity run c), the rate of non-diatom growth also increases. Due to a higher growth rate, non-diatoms consume more nutrients. As a result, nitrate concentration decreases

because it is being consumed immediately by both diatoms and non-diatoms. However, non-diatoms maintain their growth by consuming ammonium instead because the ammonium limitation for non-diatoms is weak, as suggested by high $lip2\_n4$ values in Figure 4.13. This condition leads to a higher NPP Redfield for non-diatoms in sensitivity run *c*.

5 Nutrient dynamics in the Arafura Sea

5.1 Arafura Sea circulation

The circulation in the Arafura Sea is strongly influenced by monsoonal winds (*Zijlstra et al.*, 1990; *Gordon and Susanto*, 2001; *Aldrian and Susanto*, 2003; *Kämpf*, 2015). The monsoonal winds primarily affect the circulation in the upper layer. For example, Figure 5.1 shows the surface current in January and July representing the NW and SE monsoons, respectively. In January, the surface current is predominantly flowing eastward with a magnitude less than 0.4 m s^{-1} (Figure 5.1). The surface current follows the wind direction that is blowing southeast (Figure 2.2). Moreover, the surface current in the Sahul Shelf (< 50 m region) is much smaller, less than 0.1 m s^{-1}.

In January, the eastward current is found at the surface layer and penetrates to the deeper layer, as shown in Figure 5.2. Figure 5.2 shows a positive zonal current (eastward) in most regions along the continental slope of section 01. However, some westward current cells (negative value) are found at the slope near the bottom layer. These westward current cells are quite weak, with a magnitude less than 0.1 m s^{-1}.

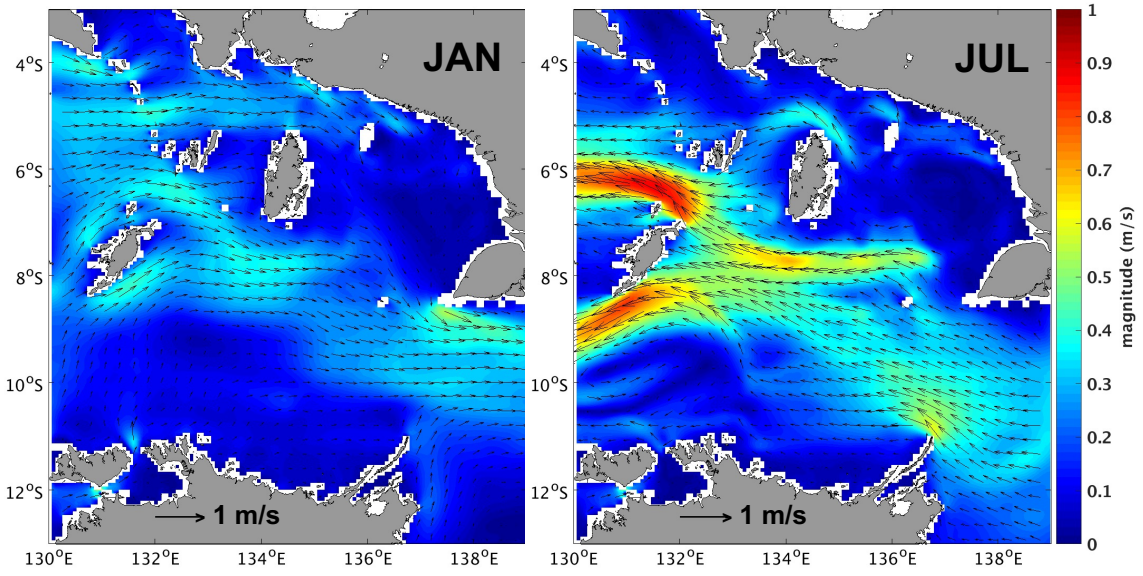

Figure 5.1: Spatial distribution of the simulated surface current in January (left) and July (right) 2014 in the Arafura Sea (see region B in Figure 3.5).

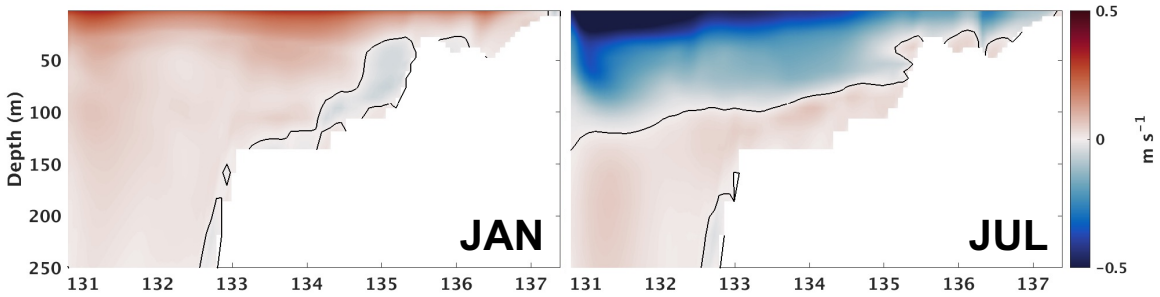

Figure 5.2: Vertical distribution of the simulated zonal velocity along section 01 in January (left) and July (right) 2014. Black contours indicate the transition from negative to positive velocities. Location of section 01 is shown in Figure 3.5.

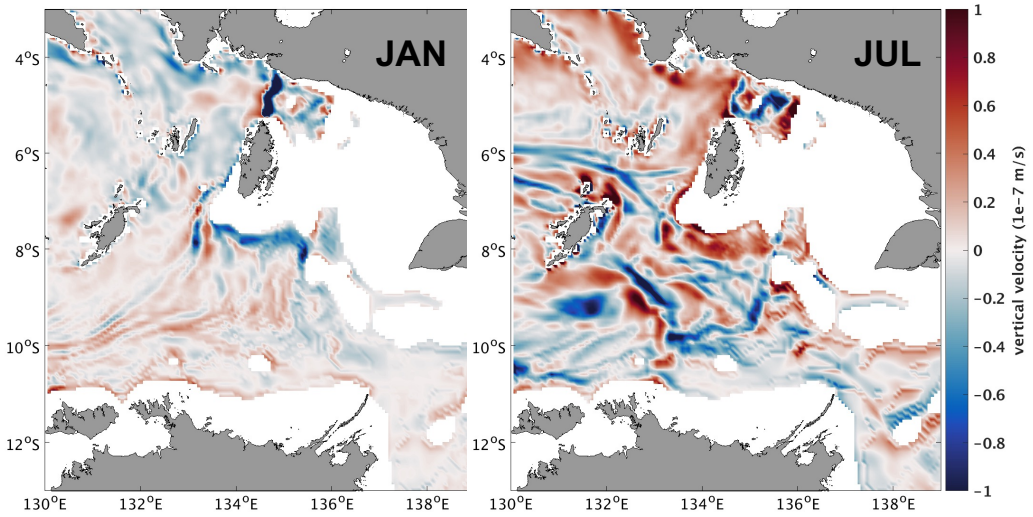

Figure 5.3: Spatial distribution of the simulated vertical velocity at 47.5 m in January (left) and July (right) 2014 in the Arafura Sea (see region B in Figure 3.5).

In January, the southeastward current, directed onshore, along the northern coast of Papua (Figure 5.1) induces the downwelling. It is indicated by the negative vertical velocity (w) (Figure 5.3). Moreover, the downwelling is also developed in the west of the Aru Islands due to onshore eastward surface current (Figures 5.1 and 5.3). In addition, the downwelling is also found north of section 01. However, unlike the northern part, the vertical velocity (w) in the southern Arafura Sea is predominantly positive.

Compared to January, the surface current in July is generally stronger and predominantly flowing westward (Figure 5.1). The stronger surface current in July is associated with a stronger wind during the SE monsoon (*Zijlstra et al.*, 1990). Figure 5.1 shows that the surface current in the Sahul Shelf is relatively weak with a magnitude less than 0.1 m s^{-1}, similar to January. In addition, on the northern coast of Papua (5°–6° S), the offshore current directed westward is also found with a relatively small magnitude around 0.2–0.3 m s^{-1}. Such offshore current transports the surface water away from the coast and drives Ekman suction, lifting the deeper water mass upward. Therefore, an upwelling occurs around this area, as indicated by positive vertical velocity (Figure 5.3).

The more pronounced westward current in July is found along section 01, driving a stronger upwelling along this region (Figures 5.1, 5.2, and 5.3). The westward current along section 01 at the surface layer is around 0.7 m s^{-1}. This westward current flows through the north and south of Tanimbar Islands to the Banda Sea with a stronger surface current magnitude up to 0.9 m s^{-1}.

As shown in Figure 5.2, the westward zonal current (negative) is found up to 150 m depth. This westward current transports the water mass westward and generates the horizontal pressure gradient in a west-east direction. The horizontal pressure gradient drives the overturning circulation directed to the east (positive value). The latter is referred to as the undercurrent, as previously demonstrated by *Kämpf* (2015). It is related to the upward movement along section 01 that brings the nutrient from the deeper layer to the euphotic zone in the upper 50 m (Figure 5.3).

Furthermore, the vertical velocity distribution in July shows the dipole structure of up- and downwelling areas, especially in the southern Arafura Sea (Figure 5.3). Previous studies showed that the topography variations mainly cause the dipole structure (*Song and Chao*, 2004; *Su and Pohlmann*, 2009). However, in the northern Arafura Sea and Aru Basin, such a dipole structure is less pronounced where it dominates by the upwelling.

Overall, the circulation in the Arafura Sea shows a distinct seasonal variation, following the monsoonal winds. The horizontal current is directed westward during the SE monsoon, and its magnitude is mainly stronger than during the NW monsoon. Moreover, in the SE monsoon, the eastward undercurrent up to 150 m depth is generated. In addition, the vertical velocities in the northern Arafura Sea and the eastern Banda Sea are predominantly positive, indicating upwelling regions. On the other hand, the southern Arafura Sea shows a dipole structure with up- and downwelling regions.

5.2 Spatial and seasonal variation of nutrients

5.2.1 Spatial distribution of nutrients

1) Nitrate

In general, Figure 5.4 shows that surface nitrate concentration is relatively low in both seasons. The surface nitrate concentration in January is depleted over the Arafura Sea and the eastern Banda Sea, less than 1 mmol N m^{-3}. Similar to January, the surface nitrate concentration in July over the southern Arafura Sea is also low. However, the northern Arafura Sea shows a higher surface nitrate concentration. The surface nitrate concentration is up to 5 mmol N m^{-3} mainly in the west of the Aru Islands and the northern coast of Papua (5°–6° S and 135°–136° E). The higher nitrate concentration in these regions is expected due to upwelling, indicated by predominantly positive vertical velocities (Figure 5.3).

The distribution of nitrate at the surface is also affected by the river run-off.

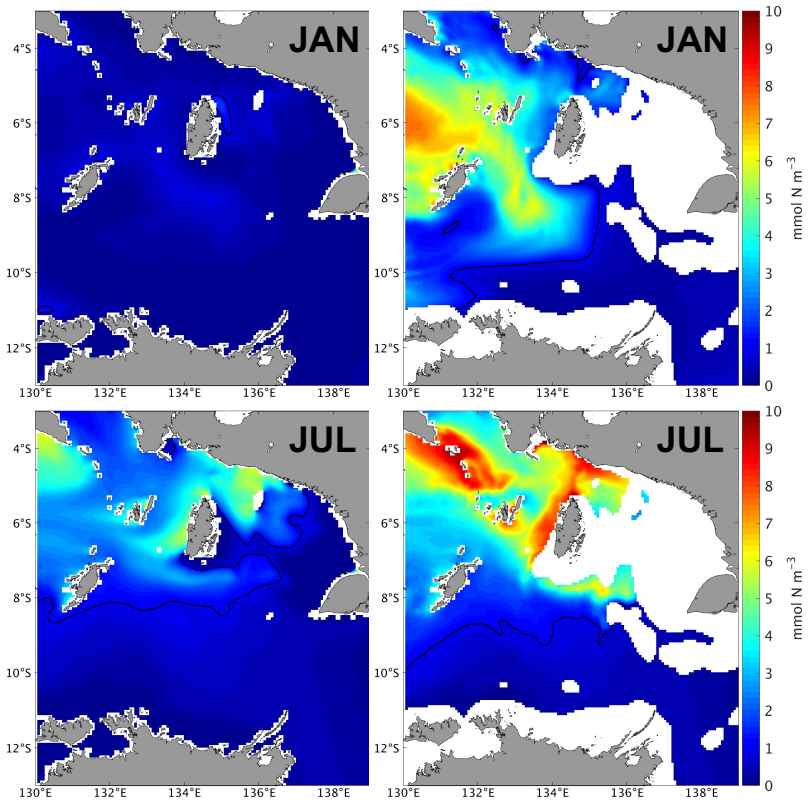

Figure 5.4: Spatial distribution of the simulated nitrate concentration in January (top panel) and July (bottom panel) 2014 at the surface (right) and 47.5 m depth (left) in the Arafura Sea (see region B in Figure 3.5). Black contours indicate 1 mmol N m^{-3}.

River influence is pronounced particularly on the southern coast of Papua (6°–8° S 137°–138° E). It is because the southern coast of Papua receives freshwater discharges from Digul and adjacent rivers. Figure 5.4 shows that the nitrate concentration is high at the Digul River mouth but depleted offshore. It is expected that the depleted nitrate is related to high stratification in this region. The freshwater discharges from Digul and the adjacent rivers decrease salinity and density significantly (see Appendix D). The river input reduces the salinity on the southern coast of Papua to less than 25 PSU and density to less than 1010 kg m^{-3}, which is almost similar to freshwater properties (see Appendix D). Subsequently, a highly stratified water column is developed, and it weakens the vertical movement. The stratification on the southern coast of Papua prevents the vertical intrusion of nitrate into the upper layer. Consequently, the surface nitrate concentration is constantly low in both seasons, as it is consumed by phytoplankton and has no supply.

Figure 5.4 shows the nitrate concentration at 47.5 m, which is generally higher than at the surface. In January, the nitrate concentration in the eastern Banda Sea reaches up to 7 mmol N m^{-3}. Figure 5.4 also reveals the horizontal intrusion of high-nitrate water from the eastern Banda Sea to the southern Arafura Sea (see area 7°–9° S 132°–134° E). It is expected that the eastward current brings this high-nitrate water from the eastern Banda Sea. As shown in the previous Section 5.1, the eastward current in January penetrates deeper.

In July, the horizontal intrusion of high-nitrate water in the southern Arafura Sea is less pronounced. A high nitrate concentration of up to 9 mmol N m^{-3} is found in the west of the Aru Islands and the northern coast of Papua. The higher nitrate concentration in these regions is more likely due to upwelling, indicated by dominant positive w (Figure 5.3). In addition, the nitrate concentration in the southern Arafura Sea at 47.5 m is low, less than 1 mmol N m^{-3}, similar to the surface concentration.

2) Phosphate

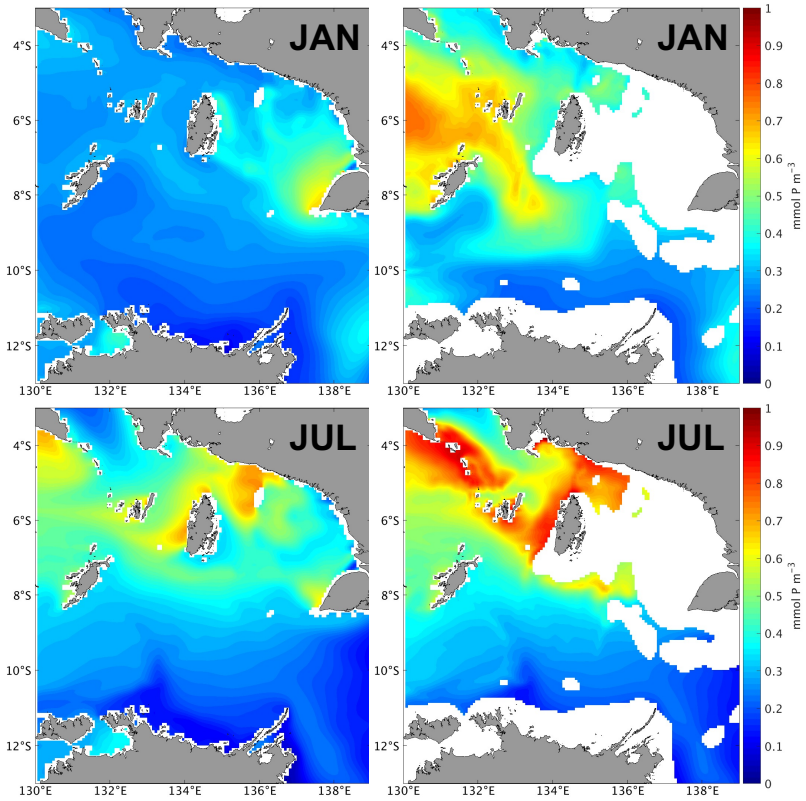

Figure 5.5: Spatial distribution of the simulated phosphate concentration in January (top panel) and July (bottom panel) 2014 at the surface (right) and 47.5 m depth (left) in the Arafura Sea (see region B in Figure 3.5).

Figure 5.5 shows the spatial distribution of phosphate at the surface and 47.5 m depth. In January, the surface phosphate concentration is higher around the Sahul Shelf, especially near the Digul River mouth. The surface phosphate concentration reaches up to 0.6 mmol P m^{-3}, which is more likely due to riverine input. Moreover, in July, the surface phosphate concentration increases, particularly in the west of the Aru Islands and the northern coast of Papua (Figure 5.5). Similar to nitrate, the high surface phosphate concentration in these regions is expected due to vertical advection. However, unlike nitrate, the surface phosphate concentration in the Sahul Shelf is not depleted. Overall, the result suggests that the nitrate to phosphate ratio does not comply with the Redfield ratio (16:1 for N:P). This indicates that the Sahul Shelf / the northern Arafura Sea is nitrate-limited.

In addition to the surface concentration, Figure 5.5 shows the phosphate concentration at 47.5 m depth. In January, similar to nitrate, the phosphate

concentration in the eastern Banda Sea is also higher, reaching up to 0.8 mmol P m^{-3}. Figure 5.5 also shows the horizontal intrusion of high-phosphate water from the eastern Banda to the southern Arafura Sea. The eastward current is expected to transport this high-phosphate water. Similar to January, the phosphate concentration in July at 47.5 m is also higher than at the surface. The higher phosphate concentration is found in the Aru Basin, the northern coast of Papua, and the southeast of Maluku Island. The higher phosphate concentration is due to upwelling, indicated by dominant positive vertical advection in July (Figure 5.3).

5.2.2 Seasonal variation of nutrients

As previously described in Section 5.1, a strong westward current is found along the continental shelf (section 01), penetrating up to 150 m. Consequently, the undercurrent is formed and expected to bring water upward. Section 01 could be a vital region where the exchange between high-nutrient water of the Banda Sea and the Arafura Sea occurs. Therefore, it is essential to investigate vertical movement, indicated by the vertical velocity, and its implication on the nutrient supply along section 01.

Figure 5.6 left shows the zonal-vertical distribution of the simulated vertical velocity (w) in January and July 2014, which represents the northwest (NW) and southeast (SE) monsoons, respectively. The positive value indicates the upwelling, and the negative value indicates the downwelling. In general, both seasons show the dipole structure of up- and downwelling areas. Figure 5.6 left shows that such dipole structures are found along the cross-shelf area.

Moreover, the magnitude of w is stronger in July than in January and is dominated by upwelling (positive w). A relatively high w in July is found in the upper 50–70 m depth. The dominant positive vertical velocity in July is associated with the vertical intrusion of nitrate-rich water onto the shelf, as shown in Figure 5.6 right. The zonal section from 134° to 137.5° E in January exhibits mostly depleted nitrate concentrations (< 5 mmol N m^{-3}). However, in July, this area receives nitrate from the deeper layer in the eastern part. The water mass is lifted through the narrow slope near 133° E. As a result, the nitrate concentration within 50 and 150 m depth along section 134°–137.5° E increases up to 15 mmol N m^{-3}, where it is three times higher than in January.

Figure 5.7 shows the seasonal variations of nitrate and phosphate profiles over the water column at station B2. For example, from January to March, the nitrate concentration over the water column is relatively low (< 5 mmol N m^{-3}), indicated by the blue color in Figure 5.7. In April, the water with higher nitrate and phosphate concentrations starts to penetrate from the deeper layer.

From April to early June, the nitrate and phosphate concentrations, particularly below 70 m, increase and further penetrate into the upper 70 m depth (Figure 5.7). From mid-June to August, the nutrient concentration below 70 m

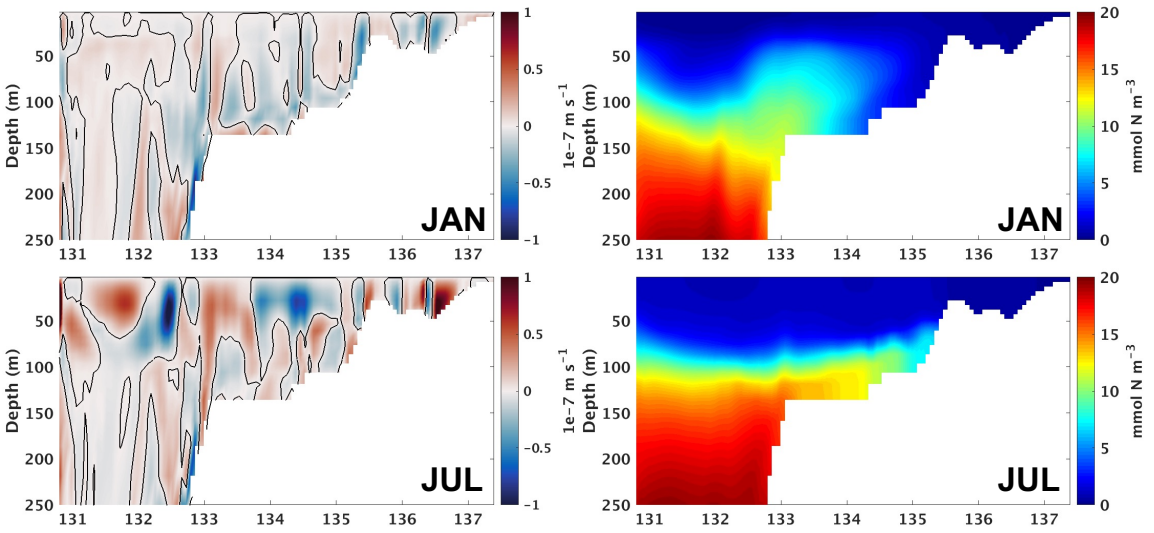

Figure 5.6: Vertical distribution of the simulated vertical velocity w (left) and nitrate concentration (right) along section 01 in January and July 2014. Black contours in the left figure indicate the transition from negative to positive velocities. Location of section 01 is shown in Figure 3.5.

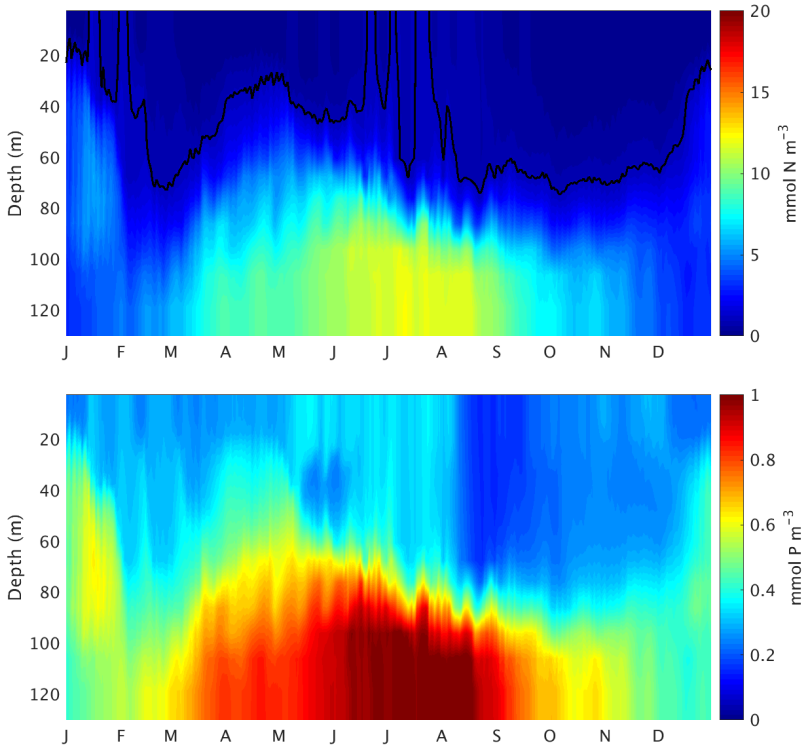

Figure 5.7: Time series of depth profiles of the simulated nitrate (top panel) and phosphate (bottom panel) at station B2 (Figure 3.5). Black contours in the upper figure indicate 1 mmol N m^{-3}.

continuously increases, indicating a permanent nutrient supply from the deeper layer. However, during the same period, the nutrient concentration in the upper 70 m further decreases. In the upper layers, nitrate is especially exhausted by phytoplankton production.

Overall, the simulation reveals that the nutrient (nitrate and phosphate) concentrations at the surface are generally lower in January than in July. The southern Arafura Sea has a poor nutrient concentration during both seasons, from the surface to deeper layers, indicating an oligotrophic region. However, the Arafura Sea receives nutrient input during the NW monsoon via the horizontal intrusion of high-nutrient water from the eastern Banda Sea. Furthermore, during the SE monsoon, the upper layer is enriched with nutrients via vertical intrusion. Such vertical intrusion is associated with the dominant upward velocity during this period.

5.3 Transport of nutrients

5.3.1 Vertical flux of nutrients

In general, nutrient concentration over the entire water column is affected by physical transport, i.e., advection and mixing. In particular, the vertical advective flow and turbulent mixing transport nutrient-rich water to the upper layer. However, while the vertical flux is essential in enriching the euphotic zone, no previous studies in the Arafura Sea addressed such aspects. Therefore, the following section will discuss the magnitude of nutrient fluxes in the vertical direction and its seasonal variation in further detail.

The calculation of nutrient fluxes focuses on the two vital regions associated with the upwelling and Chl-a blooms. The first region is the Sahul Shelf (northern Arafura Sea), specifically near the western coast of Papua, where the Chl-a blooms are mainly observed during the SE monsoon. The first region is represented by station B1 (Figure 3.5). The second region is a continental slope (section 01), a pathway for the Banda Sea water masses. The second region is represented by station B2 (Figure 3.5).

Station B1 in the Sahul Shelf is a shallow region with low nitrate concentrations. The vertical profiles of nitrate concentration at station B1 are relatively homogenous from the surface to the bottom layer in both seasons (Figure 5.8). The vertical profile indicates that the water column at station B1 is relatively well-mixed. Moreover, the simulated nitrate concentration is higher and more varying in July than in January. Due to a homogenous profile, the nitrate fluxes will be calculated for the near-surface (upper 10 m), where phytoplankton production mainly occurs.

Figure 5.9 shows that the advective vertical flux to the near-surface layer at station B1 is mainly positive or upward. The advective vertical flux is relatively weak from January to May, with a dominant downward flux in February–March. By contrast, the advective vertical flux is mainly upward from June onwards, except from mid-August to mid-September. The upward vertical flux reaches the maximum in December with a magnitude up to 1.5 mmol N m^{-2} d^{-1}.

Similar to the advective flux, the vertical turbulent (mixing) flux to the

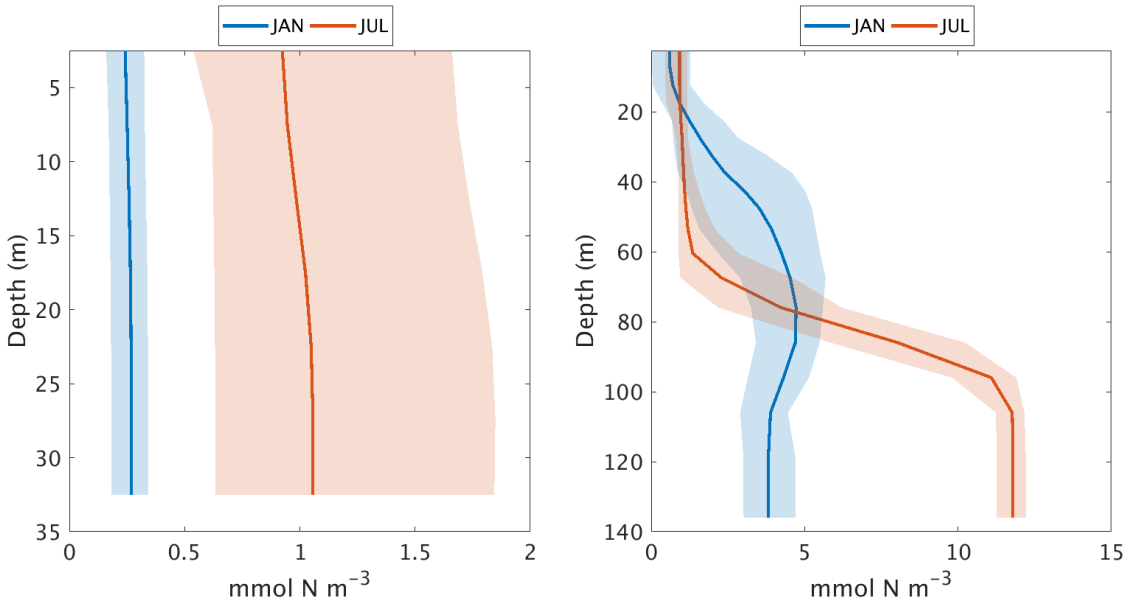

Figure 5.8: Vertical profiles of the simulated nitrate in January and July at stations B1 (left) and B2 (right) (Figure 3.5). The shaded plot indicates the model range, calculated from a one-month statistic for the respective month.

near-surface layer at station B1 is mainly upward. The mixing flux is weak from January to May and relatively strong from June onwards. The results indicate that both advective and mixing play a role as nitrate sources. The near-surface layer at station B1 receives the nitrate via both advective and mixing fluxes, with similar magnitudes.

Compared to station B1, the simulated nitrate profiles at station B2 are more stratified. Figure 5.8 shows that the nitrate concentration in January is about 0.6 mmol N m^{-3} at the surface layer and increasing to about 5 mmol N m^{-3} at 80 m. Below 80 m to the bottom, the nitrate concentration slowly decreases to 4 mmol N m^{-3}. The increase of nitrate concentration at 80 m depth is expected due to nitrate intrusion from the eastern Banda Sea (Figure 5.4). Furthermore, in July, the nitrate concentration increases. Figure 5.8 shows that nitrate is homogenous from the surface to around 60 m, indicating a mixed layer. Nitrate concentration within the mixed layer is around 1 mmol N m^{-3}. Within 60 m to 100 m layers, nitrate rapidly increases, indicating a nitracline layer. From 100 m to the bottom, the nitrate profile is relatively constant, with a concentration of about 12 mmol N m^{-3}.

The nitracline layer at station B2 plays a role as a barrier between the mixed and deeper layers, often inhibiting vertical fluxes. Since phytoplankton is mainly distributed within the euphotic zone in the mixed layer, it is important to investigate the nutrient fluxes across the nitracline layer. Therefore, the calculation of the nitrate fluxes at station B2 focuses on the layer above the nitracline.

In general, the vertical advective flux of nitrate across the nitracline layer at station B2 is larger than the mixing flux. Figure 5.10 shows that the advective downward flux of nitrate in January (NW monsoon) is more dominant than the

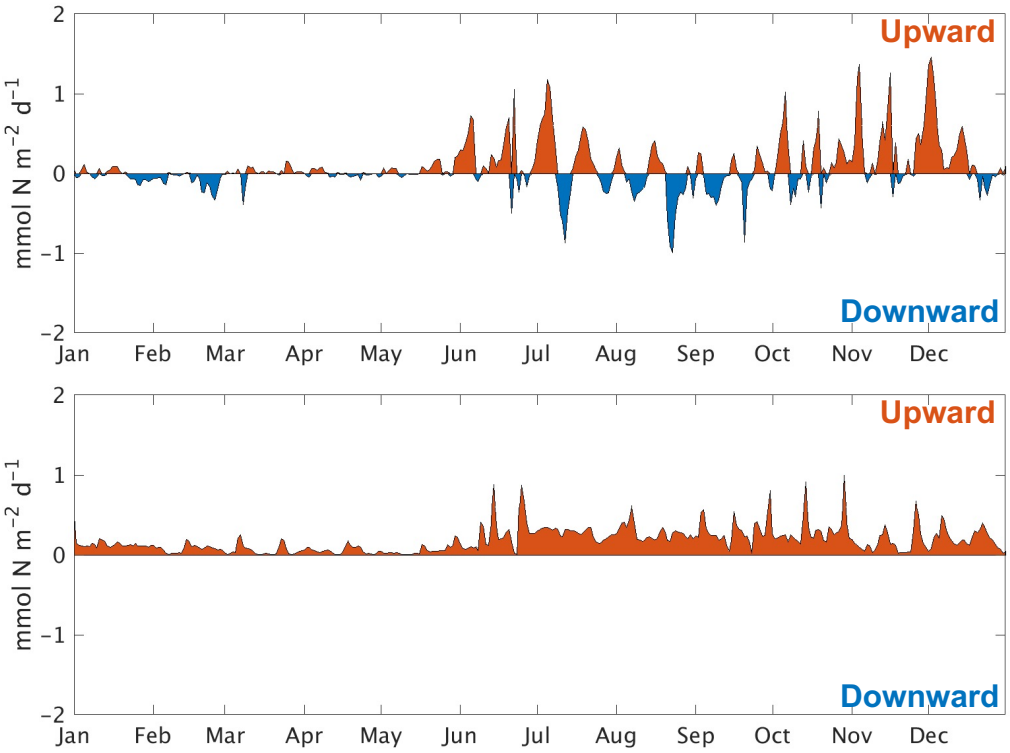

Figure 5.9: Advective (top panel) and turbulent (bottom panel) vertical fluxes of nitrate at station B1 across 10 m depth horizon (see station B1 in Figure 3.5). The plots represent the nitrate fluxes between the deep and the near-surface layers.

upward flux. From March to April, the advective flux decreases to less than 1 mmol N m^{-2} d^{-1}. It is similar to the overall magnitude of vertical mixing flux (Figure 5.10). Moreover, from April to June, the upward advective flux is more dominant and reaches up to around 6 mmol N m^{-2} d^{-1}. In July, the downward advective flux is more dominant with a value up to -3 mmol N m^{-2} d^{-1}. By contrast, the advective vertical flux in August is mainly upward, which coincides with a maximum upward mixing flux (Figure 5.10). Furthermore, from September to December, both advective and mixing fluxes are low.

Overall, the simulation results confirm that the advective vertical flux is the dominant mechanism in transporting nutrients to the upper layer at station B2. The high upward advective flux occurs during the SE monsoon, associated with the upwelling. On the other hand, the advective flux is dominantly downward in the NW monsoon, which is associated with downwelling.

5.3.2 Horizontal transport

The above section has shown the roles of vertical fluxes in supplying nutrients in the Arafura Sea. In addition to vertical transport, it is also essential to consider horizontal transport, specifically the horizontal transport of nutrients to the northern Arafura Sea, where the high Chl-a concentration is primarily observed. Therefore, the meridional (south–north) transport of nutrients across section 01 is

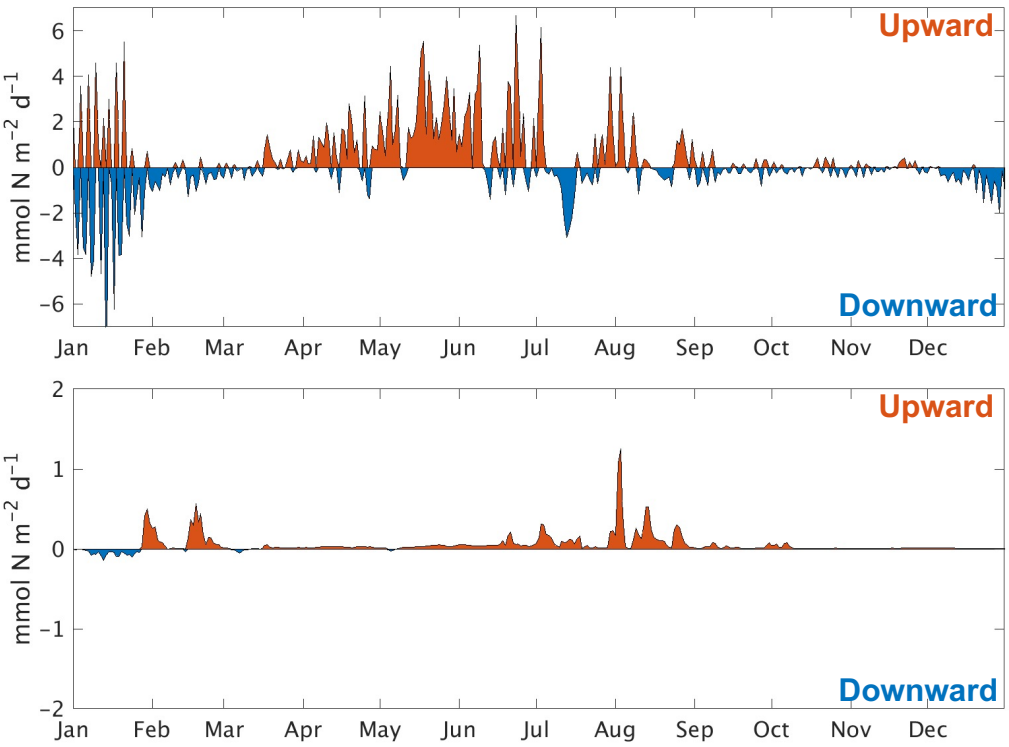

Figure 5.10: Advective (top panel) and turbulent (bottom panel) vertical fluxes of nitrate at station B2 across 64 m depth horizon (see station B2 in Figure 3.5). The plots represent the nitrate fluxes between the above and below nitracline layers.

calculated. The meridional transport is differentiated between the layer above and below the nitracline. The northward (positive) transport indicates that the northern Arafura Sea / Sahul Shelf receives nutrient input. Meanwhile, the southward (negative) transport suggests that the northern Arafura Sea loses the nutrients.

Figure 5.11 shows the seasonal variations of the horizontal transport for nitrate across section 01, above and below the nitracline. During the NW monsoon (December–February), the nitrate transport above the nitracline is dominantly southward, ranging from 0.05 to 0.7 Gmol N d^{-1}. The maximum of the southward transport is found in mid-January, which is associated with the horizontal intrusions of high nutrient water from the eastern Banda Sea (see Section 5.2.1). During the first transition monsoon (March–May), both the northward and southward transports are found with similar magnitudes. Moreover, from June to mid-November, nitrate transport is dominantly northward. In addition, the northward transport reaches up to 0.3 Gmol N d^{-1} in July (Figure 5.11).

The horizontal transport below the nitracline shows a different seasonal variation with the layer above the nitracline (Figure 5.11). Unlike the layer above, the layer below the nitracline has two periods with dominant northward nitrate transport. The first period with the dominant northward transport occurs from February to mid-May. During this period, the northward transport reaches up to 1.4 Gmol N d^{-1}. The second period with the dominant northward transport is from July to September with a smaller magnitude.

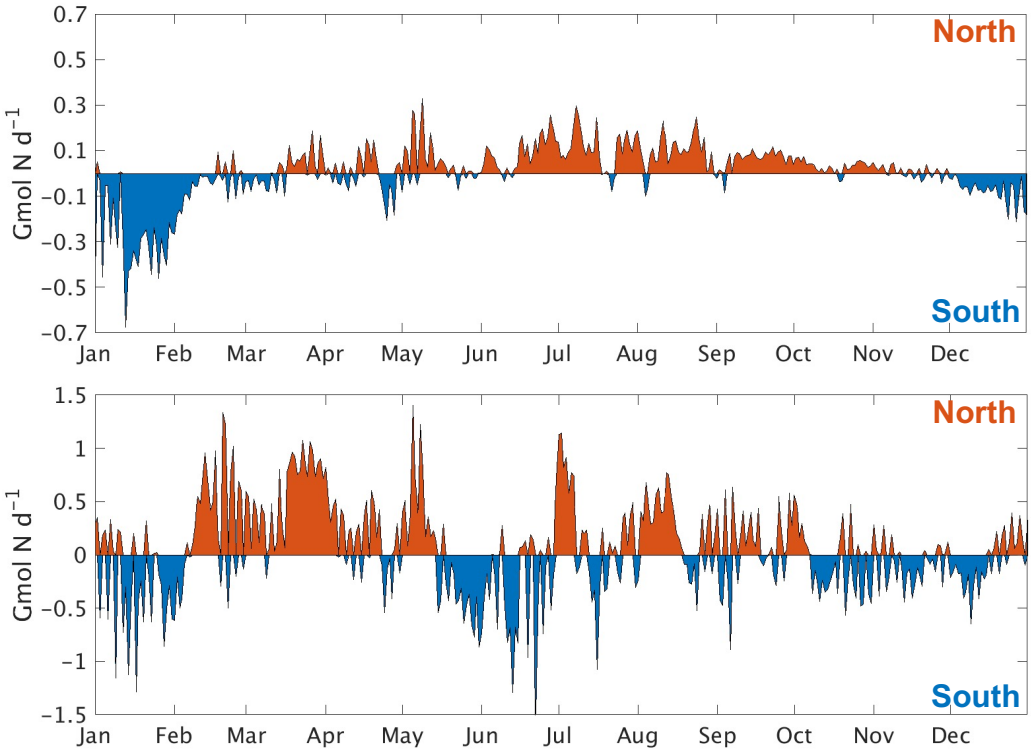

Figure 5.11: Meridional transport of nitrate across section 01 integrated over the upper 64 m (top panel) and from 64 m to the bottom (bottom panel). The top and bottom figures represent the transport above and below nitracline layers, respectively. Section 01 is shown in Figure 3.5.

Additionally, the layer below the nitracline also shows two periods with dominant southward transport. The first period with the dominant southward transport occurs from mid-May to June. The southward nitrate transport reaches the highest magnitude of -1.5 Gmol N d^{-1} at the end of June. It is expected that the southward transport during this period mainly occurs in the western part of section 01 (around 131°–133° E). The western part of section 01 is located at the south of the Tanimbar Islands, where the westward current is deflected southward (see Section 5.1). The second period with dominant southward transport is found from October to December/January.

5.4 Nutrients budget

The previous Section 5.3 showed the contribution of hydrodynamic processes on nutrient transport, i.e., advection and mixing. The results show that the near-surface layer in the northern Arafura Sea (station B1) receives the nutrients via vertical advection and mixing with similar magnitudes. By contrast, the upper layer in the continental slope area (station B2) mainly receives the nutrients via vertical advection. However, besides hydrodynamic processes, it is also essential to consider other processes contributing to nutrient supply in the Arafura Sea. Therefore, the budget plot of nutrients is presented to show the complete picture of

contributing processes.

Like previous Section 5.3, the calculation of nutrient budget at station B1 divides into two parts, which are the near-surface and deeper layers. For example, the cumulative nitrate budget from January 1 to December 31, 2014, is shown in Figure 5.12. Generally, in the near-surface layer, the nitrate concentration is relatively low from January to May. During this period, vertical mixing increases nitrate concentration, although it is immediately consumed by phytoplankton, especially diatoms. In this layer, vertical mixing is the dominant source of nitrate, while other nitrate sources such as atmospheric nitrogen deposition and nitrification are comparatively low.

Table 5.1: Processes affecting nitrate concentration.

Process	Description
adv_n3n	nitrate concentration change due to vertical advection
adh_n3n	nitrate concentration change due to lateral advection
mxv_n3n	nitrate concentration change due to vertical mixing
mxh_n3n	nitrate concentration change due to lateral mixing
$n4n\_n3n$	nitrification
$n3n\_p1n$	nitrate uptake by diatoms
$n3n\_p2n$	nitrate uptake by non-diatoms
atm_n3n	nitrate concentration change due to atmospheric deposition

In early June, the nitrate concentration in the near-surface layer rapidly increases, associated with the beginning of the SE monsoon. During this period, the increase of nitrate concentration is due to vertical mixing and advection (Figure 5.12). From July to September, the nitrate concentration fluctuates, but its trend decreases. During this period, the near-surface layer receives nitrate continuously by vertical mixing, but it is consumed by phytoplankton. As shown in Figure 5.12, the increase in nitrate concentration is followed by an increase in phytoplankton uptake.

From mid-September to November, the nitrate concentration fluctuates over a period of two weeks. For example, from mid-September to early October, the nitrate concentration increases by about 100 mmol N m^{-2} and reaches its peak. Afterward, the nitrate concentration decreases by a similar magnitude from early October to mid-October, reaching a minimum. A similar fluctuation occurs until November (Figure 5.12). These oscillations are due to the 24h averages of hydrodynamic forcing for ECOHAM input (see Section 3.2.2). Since two M2 tidal components have a period of more than 24 hours (∼24h 50 min), the 24h averaging produces a beat frequency, represented by an oscillation in the nitrate budget plot. In principle, these beat frequencies can be removed by averaging the hydrodynamic forcing over two M2 tidal periods. Such a process would smooth the plot curves, but problems with a daily nutrient budget might arise, as the budget is no longer closed.

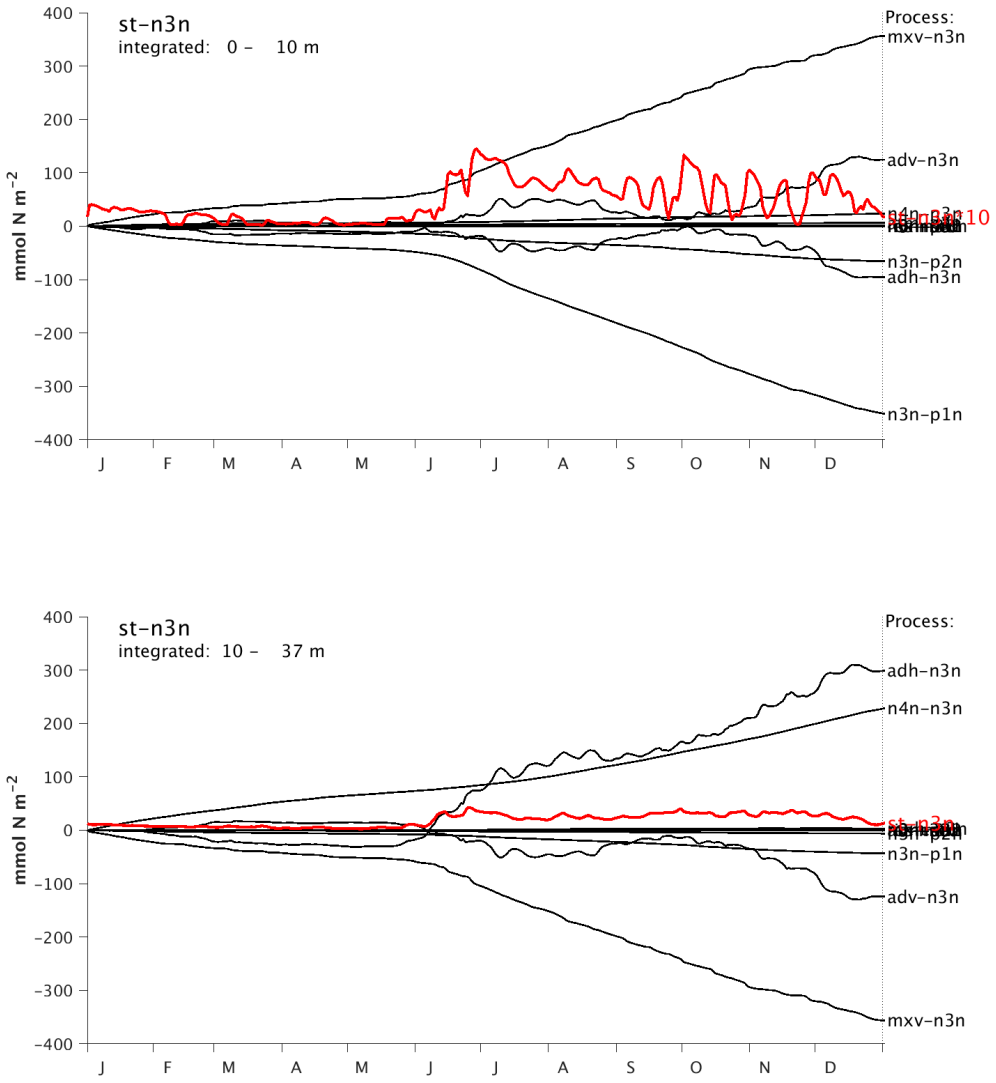

Figure 5.12: Time series of nitrate budget at station B1 (Figure 3.5). The top and bottom figures represent the nitrate budget at the near-surface and deeper layers, respectively. In the top figure, the nitrate concentration (st_n3n) indicated by a red line is reduced by a factor of ten. The description of each process is shown by Table 5.1.

In addition to the near-surface layer, Figure 5.12 also shows the nitrate budget in the deeper layer. From January to May, nitrification and vertical advection supply nitrate, while horizontal advection and vertical mixing reduce nitrate concentration. During this period, the loss of nitrate exceeds the supply. Hence, the nitrate concentration is constantly low. However, in June, the nitrate concentration rapidly increases due to horizontal advection. Additionally, nitrification also supplies nitrate continuously until December.

After increasing in June, the nitrate concentration in the deeper layer of station B1 is relatively constant until December. This is because the nitrate supply by horizontal advection and nitrification compensates for the nitrate loss by vertical

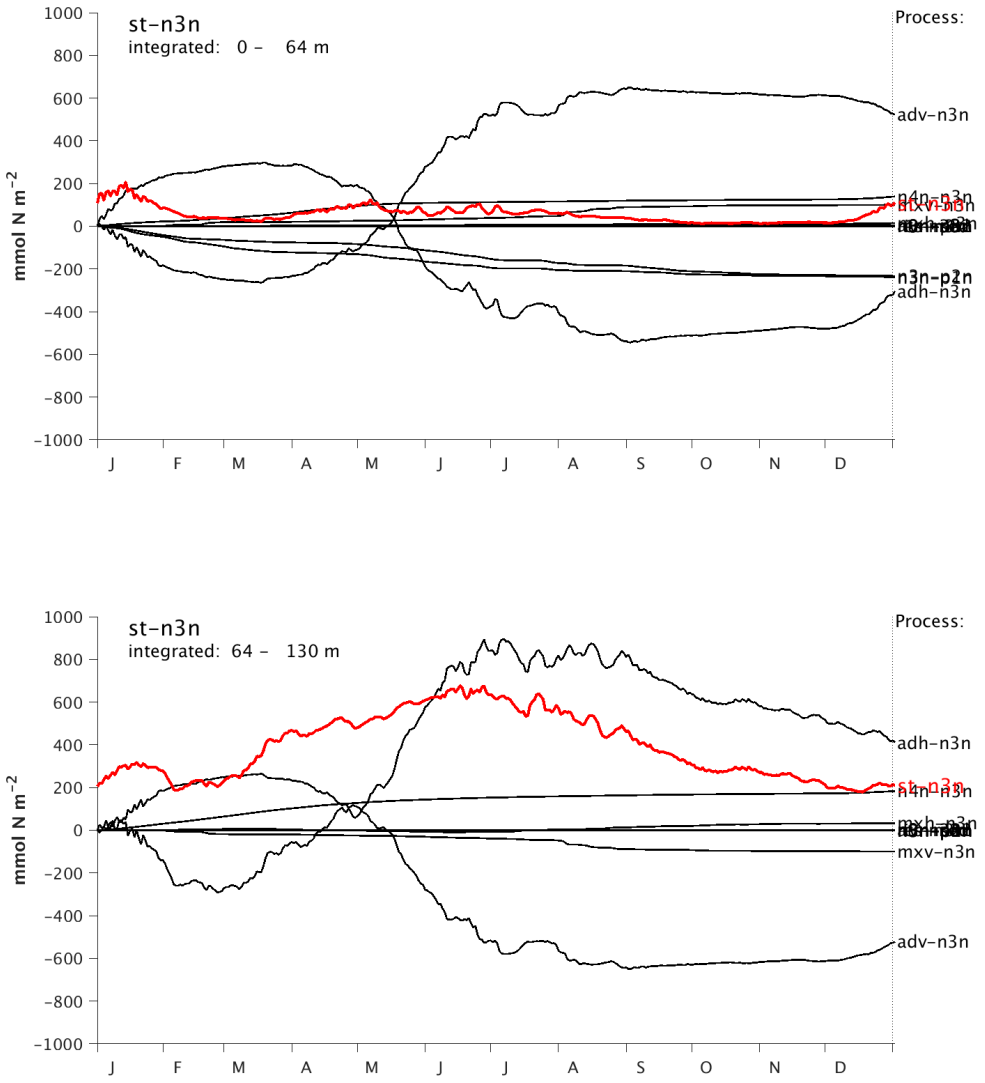

Figure 5.13: Time series of nitrate budget at station B2 (Figure 3.5). The top and bottom figures represent the nitrate budget above and below nitracline layers, respectively. The nitrate concentration (st_n3n) indicated by a red line. The description of each process is shown by Table 5.1.

advection and mixing. Furthermore, the nitrate loss by phytoplankton uptake in the deeper layer is significantly smaller than in the near-surface layer (Figure 5.12).

Overall, the nitrate budget in the near-surface and deeper layers at station B1 show different dominant processes. The dominant nitrate source in the near-surface layer is vertical mixing, while in the deeper layer, the nitrate source is mainly from horizontal advection and nitrification. On the other hand, the primary nitrate loss in the near-surface and deeper layers is due to phytoplankton uptake and vertical mixing. The simulation results also indicate a relatively sustained nitrate supply in the near-surface layer from June to December.

In addition to the nitrate budget at station B1, the nitrate budget at station B2

is also presented (Figure 5.13). Like in the previous Section 5.3, the nitrate budget is divided into the layer above and below the nitracline. In general, the nitrate budget above and below nitracline layers shows a seasonal variation. For example, the nitrate concentration increases in the layer above the nitracline due to horizontal advection from the first of the year to mid-January. During this two-week period, the horizontal advection transports a higher nitrate water mass from the eastern Banda Sea (see Section 5.2.1). However, from mid-January to mid-March, the nitrate concentration decreases due to phytoplankton uptake and vertical advection.

Furthermore, from mid-March to early May, the nitrate concentration in the layer above the nitracline increases. It is due to nitrate supply via vertical advection and nitrification during this period. The rate of nitrate supply via vertical advection remains increasing until the end of June, indicated by a steeper gradient of adv_n3n (Figure 5.13). Simultaneously, horizontal advection reduces the nitrate concentration by about the same amount as vertical advection. Nevertheless, the nitrate supply via vertical advection is higher by about 30 mmol N m^{-2}, so that the nitrate concentration increases.

The nitrate concentration in the layer above the nitracline fluctuates from May to the end of July, but the trend is relatively constant. During this period, the nitrate supply via vertical advection compensates for nitrate loss via horizontal advection and phytoplankton uptake. Moreover, the nitrate concentration decreases from August to September due to phytoplankton uptake. Unlike station B1, the magnitude of nitrate uptake by diatoms and non-diatoms at station B2 is almost similar (Figure 5.13). Furthermore, the nitrate concentration increases again in December. During this period, the horizontal advection supplies nitrate while phytoplankton uptake is almost absent.

Below the nitracline, the nitrate concentration shows an even stronger seasonal cycle, with a peak in mid-June. In the layer below the nitracline, the hydrodynamic processes mainly regulate the nitrate budget. For example, in January, the nitrate concentration decreases due to horizontal advection. During this period, nitrate is transported southward by horizontal advection (see Section 5.2.1). Furthermore, from February to mid-June, horizontal advection supplies nitrate so that nitrate concentration increases. Simultaneously, vertical advection reduces the nitrate concentration by about the same amount as horizontal advection provides nitrate. Nevertheless, the contribution of horizontal advection is higher by about 100 mmol N m^{-2}, so that the nitrate concentration increases.

From mid-June to the end of August, the nitrate input via the horizontal advection fluctuates, but the trend is relatively constant. In the same period, the nitrate loss via vertical advection and mixing increases. As a result, the nitrate concentration decreases. Moreover, from August to November, the nitrate concentration constantly decreases due to horizontal advection. It is expected that the westward current transports nitrate at station B2 to the west during this period. Furthermore, the nitrate loss due to phytoplankton uptake in the layer below the nitracline is almost absent. It is clearly shown by the nitrate budget

below 64 m in Figure 5.13 (bottom panel).

Overall, the dominant sources of nitrate in the layer above and below the nitracline are vertical and horizontal advection, respectively. Moreover, the primary nitrate loss in the layer above the nitracline is due to horizontal advection and phytoplankton uptake. In the layer above the nitracline, the magnitudes of nitrate uptake by diatoms and non-diatoms are similar. By contrast, in the layer below the nitracline, the nitrate loss by phytoplankton uptake is absent. In this layer, nitrate loss is primarily due to vertical advection and mixing.

6 Phytoplankton dynamics in the Arafura Sea

6.1 Spatial distribution of phytoplankton

In general, phytoplankton distribution is regulated by physical conditions in the water, such as light and temperature. For this reason, phytoplankton is primarily distributed in the upper layer, within the euphotic zone where light is available for phytoplankton growth. In addition to light and temperature, nutrients also affect the phytoplankton distribution. However, although light is abundant in the upper layer, this layer is often exhausted of nutrients. Hence, the physical mechanism that transports the nutrients to the upper layer, such as upwelling or vertical mixing, is essential. Additionally, river run-off also plays a role in providing nutrients. Subsequently, high phytoplankton concentration is often found in upwelling regions and near river mouths.

In this section, the spatial distribution of phytoplankton will be discussed. The concentration of phytoplankton is expressed by the nitrogen element within phytoplankton. Nitrogen is chosen for consistency of the unit used for the discussion of nutrient and phytoplankton dynamics.

Figure 6.1 shows the spatial distribution of diatoms at the surface in two different seasons. In both seasons, diatoms are mainly distributed in the northern Arafura Sea, while the southern part encompasses low diatom concentrations. The low diatom concentrations in the southern Arafura Sea are associated with the depleted nutrient concentrations in this region. However, at the Digul River mouth, high diatom concentrations are constantly found in January and July. It is related to a continuous supply of nutrients from the river. In January, the diatom concentration in the Sahul Shelf, except at the Digul River, is about 0.9 mmol N m^{-3}.

In July, the diatom concentrations in the northern Arafura Sea (Sahul Shelf), Aru Basin, and the eastern Banda Sea increase. The highest diatom concentration is found mainly on the northern coast of Papua, exceeding 2 mmol N m^{-3}. The high diatom concentration in July is associated with nutrient input to the surface by upwelling during this period.

In addition to diatom, the distribution of non-diatom at the surface is also presented. Figure 6.2 shows that non-diatom concentrations are higher than diatom concentrations in most areas. Similar to diatom, the non-diatom concentrations in

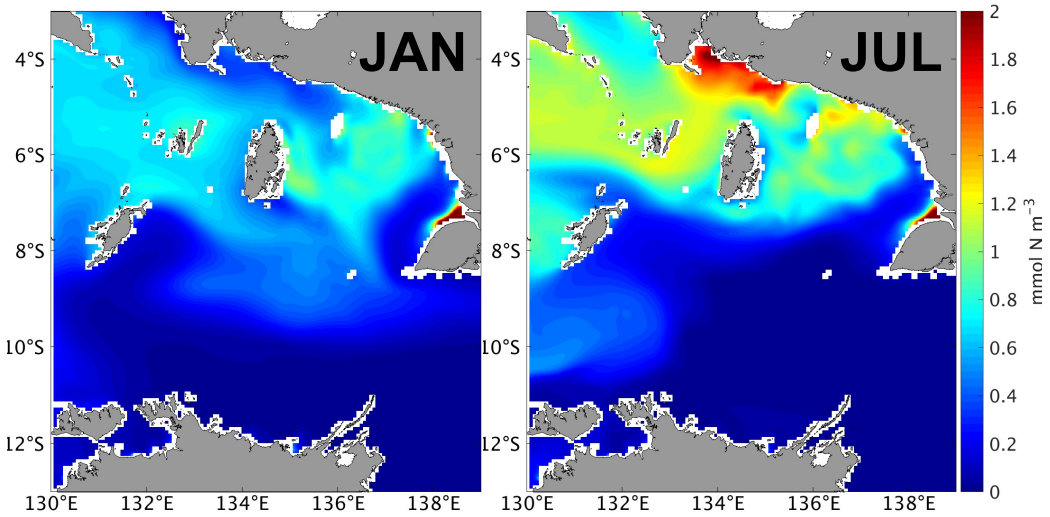

Figure 6.1: Spatial distribution of diatoms at the surface in January (left) and July (right) 2014 in the Arafura Sea (see Region B in Figure 3.5).

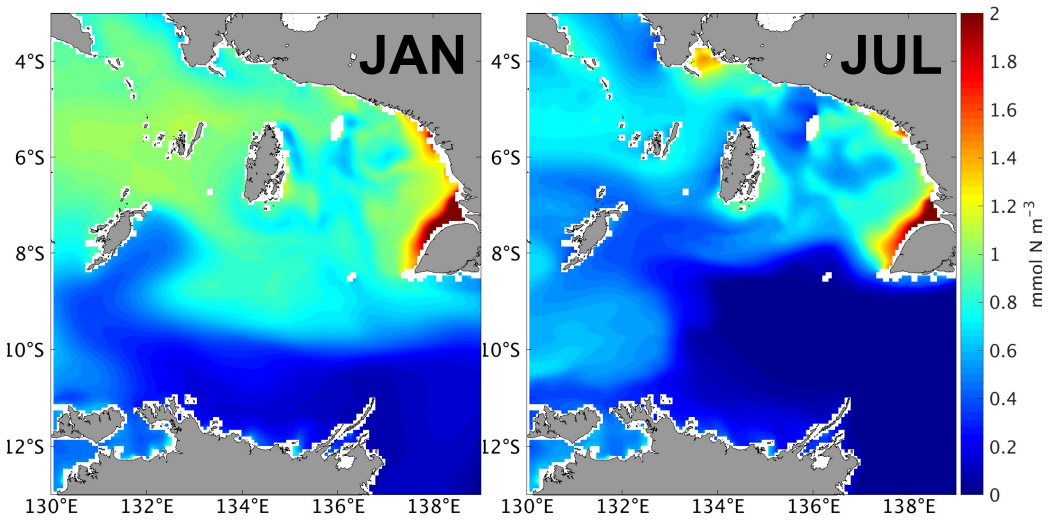

Figure 6.2: Spatial distribution of non-diatoms at the surface in January (left) and July (right) 2014 in the Arafura Sea (see Region B in Figure 3.5).

the southern Arafura Sea are low, associated with low nutrient concentrations in this region. By contrast, non-diatom concentrations on the southern coast of Papua and near the Digul River mouth are constantly high (> 2 mmol N m^{-3}) in both seasons (Figure 6.2), due to riverine nutrient input.

In January, non-diatom concentrations are slightly elevated in the Arafura Sea and the eastern Banda Sea, with a concentration around 1.1 mmol N m^{-3}. By contrast, in July, the non-diatom concentrations are generally lower than in January, especially in the northern Arafura Sea, the Aru Basin, and the eastern Banda Sea. In these regions, non-diatom concentrations decrease to less than 0.7 mmol N m^{-3}. However, on the northern coast of Papua, there is a small area with a higher non-diatom concentration, around 1.4 mmol N m^{-3}.

While the Aru Basin and the eastern Banda Sea show a substantial decrease in

non-diatom concentrations in July, the Sahul Shelf shows small concentrations change. In July, non-diatom concentration in the Sahul Shelf, especially on the southern coast of Papua, is similar to January. The non-diatom concentration in the Sahul Shelf is indeed lower but less significant compared to the Aru Basin and the eastern Banda Sea (Figure 6.2).

Overall, the phytoplankton distribution varies between the eastern Banda Sea and the northern and southern parts of the Arafura Sea. For example, the distribution of diatoms at the surface in the northern Arafura Sea and the eastern Banda Sea is generally in line with nutrient distribution, especially nitrate (compare Figures 5.4 and 6.1). However, unlike diatom, the concentrations of non-diatom in these regions show an inverse pattern, i.e., higher in January than in July. When the surface nitrate concentrations increase during the upwelling season in July, diatom concentrations increase. During this period, diatoms often dominate the phytoplankton species. However, when the upwelling is absent such as in January, the surface nitrate concentrations decrease, followed by the decrease of diatom concentrations. During the nitrate-depleted condition, non-diatom concentration increases and is often higher than for diatoms.

The phytoplankton species shift (succession) from diatoms to non-diatoms (like flagellates), which is found in the northern Arafura Sea and the eastern Banda Sea, is typically found in upwelling regions. *Fawcett and Ward* (2011) suggested that diatom is the dominant phytoplankton species during the early stage of upwelling due to its ability to respond rapidly to a newly nitrate input. In the freshly upwelled water, compared with the Redfield ratio, diatoms consume nitrogen at a higher rate than phosphorus (*Wasmund et al.*, 2014). Diatoms increase the specific nitrate uptake rate, allowing for the consumption of a large fraction of the available nutrients, stimulating faster growth (*Fawcett and Ward*, 2011). As a result, a higher growth rate allows diatoms to surpass other phytoplankton groups and consume more limiting nutrients (*Fawcett and Ward*, 2011).

Previous studies also suggested that the succession of the phytoplankton corresponds to the vertical stability of the water column (*Pitcher et al.*, 1991; *Wasmund et al.*, 2014). In the early stage of upwelling, the turbulence increases, and the upper water column is enriched with nutrients. During this period, a higher level of turbulence prevents diatoms from sinking due to their large size among other phytoplankton groups (*Huisman and Sommeijer*, 2002; *Fawcett and Ward*, 2011). As the upwelling relaxes, the water column is more stratified, and nutrients are depleted (*Pitcher et al.*, 1991). Many field observations in the Benguela upwelling system showed that during this period, a predominantly flagellate species is found (*Pitcher et al.*, 1991). As nutrients are depleted during this period, the increase of flagellates might result from the nutrient uptake via motility (*Pitcher et al.*, 1991).

By contrast, the southern Arafura Sea and the Sahul Shelf show different phytoplankton patterns. In these regions, nitrate concentrations are low and often lower than phosphate (see Section 5.2.1). Moreover, the seasonal variation of nitrate

concentrations at the surface in these regions is less pronounced. Therefore, the variation of phytoplankton concentration between January and July is also less significant.

6.2 Limitation factors

Generally, phytoplankton growth is influenced by nutrients, light, and temperature. Nutrient and light determine the phytoplankton growth, in which their absence would stop phytoplankton growth. On the other hand, the temperature rather changes the rate of phytoplankton growth to be faster or slower. In the following section, the time series of each limitation factor is presented to investigate its seasonal variation.

Figure 6.3 shows the monthly time series of nitrogen limitation for diatoms and non-diatoms at station B1. The nitrogen limitation factor ranges from 0 to 1, with 0 indicating no growth and 1 indicating no limitation. The small factor is associated with low nutrient availability, which limits phytoplankton growth and vice versa. Generally, the nitrogen limitation factor for diatoms is smaller than for non-diatoms and shows a seasonal variation. The nitrogen limitation factor for diatoms (non-diatoms) reaches its peak in July (August), indicating the weakest nitrogen limitation. The weakest nitrogen limitation relates to high nutrient input via horizontal advection during this period (see Section 5.2.1). Moreover, nitrogen limitation for diatoms is also relatively weak in January.

By contrast, nitrogen limitations for diatoms and non-diatoms are the strongest in April and May, respectively. During this period, the nitrogen is exhausted via phytoplankton uptake. On the other hand, nutrient supplies via advection and mixing are small. A similar mechanism occurs in November, resulting in the secondary strong nitrogen limitation for diatoms and non-diatoms.

In addition to nitrogen limitation, Figure 6.3b also shows the ratio of phosphorus limitation to nitrogen. A ratio higher than 1 implies that phytoplankton is nitrogen-limited, and a ratio less than 1 indicates that phytoplankton is phosphorus-limited. Figure 6.3b shows that diatoms are nitrogen-limited for the whole year, with the highest ratio in April. It suggests that during this period, nitrogen is depleted, while phosphate is abundant. In addition, diatoms are also not limited by silica because silica is relatively abundant throughout the year (Figure 6.3c). Unlike diatoms, the ratio of phosphorus limitation to nitrogen for non-diatoms is approaching 1, with a deviation less than 0.2. Throughout the year, non-diatoms are mostly nitrogen-limited. However, from July to September, non-diatoms are slightly phosphate-limited.

Figure 6.4 shows the monthly time series of nitrogen limitation for phytoplankton at station B2. Similar to station B1, the nitrogen limitation factor for diatoms is also smaller than for non-diatoms. Figure 6.4 also shows a seasonal variation with two peaks indicating weak nitrogen limitation. The nitrogen limitation for diatoms reaches the first peak in February and the second peak, with

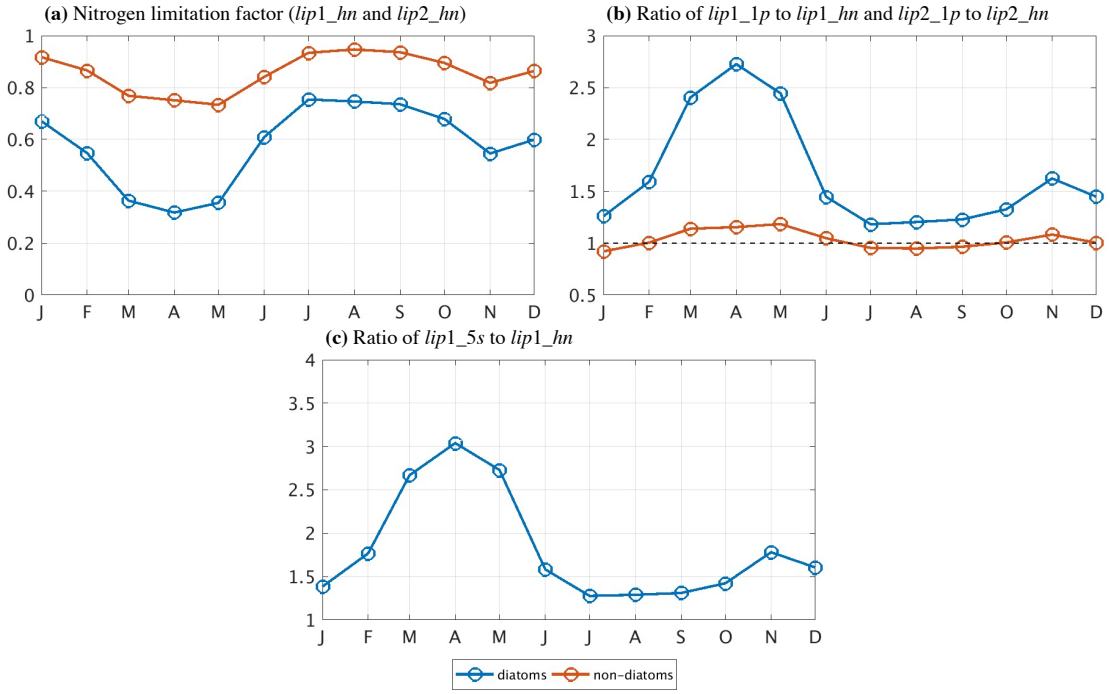

Figure 6.3: Time series of (a) nitrogen limitation factors (Equations 3.24 and 3.25); (b) ratio of phosphorus limitation to nitrogen limitation; (c) ratio of silica limitation to nitrogen limitation (diatoms only) at station B1 (Figure 3.5). Nutrient limitation factors were calculated at the surface.

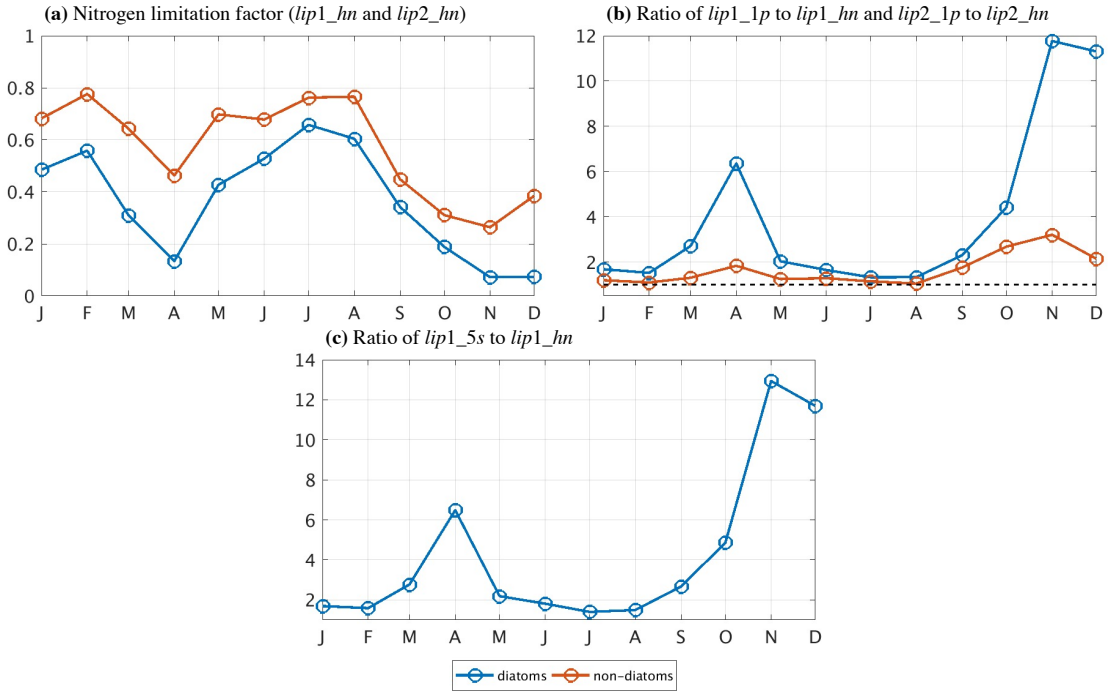

Figure 6.4: Time series of (a) nitrogen limitation factors (Equations 3.24 and 3.25); (b) ratio of phosphorus limitation to nitrogen limitation; (c) ratio of silica limitation to nitrogen limitation (diatoms only) at station B2 (Figure 3.5). Nutrient limitation factors were calculated at the surface.

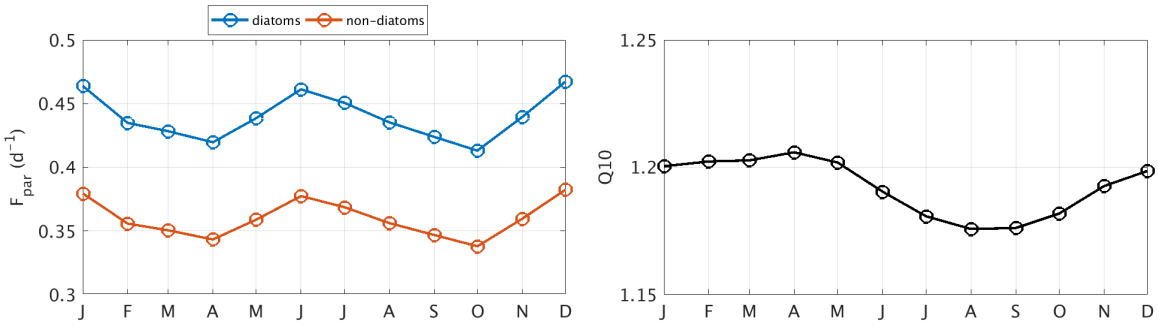

Figure 6.5: Time series of light-dependent growth rate (left) and temperature factor (right) at the surface of station B1 (Figure 3.5).

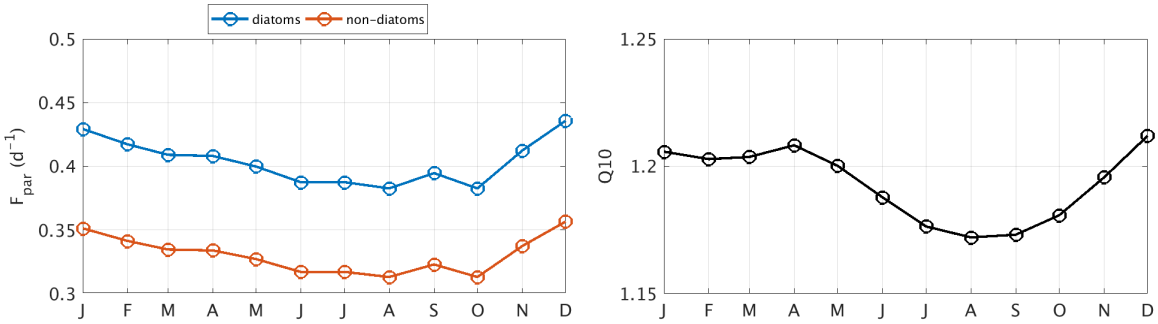

Figure 6.6: Time series of light-dependent growth rate (left) and temperature factor (right) at the surface of station B2 (Figure 3.5).

a higher factor in July. The peak in February is associated with the horizontal intrusion of nitrate from the eastern Banda Sea (see Section 5.2.1). Meanwhile, the peak in July is related to nitrate input via the vertical advection or upwelling. Like diatoms, the nitrogen limitation factor for non-diatoms also has two peaks in February and July–August, with similar values.

The nitrogen limitation for diatoms at station B2 is the strongest in November-December, with a factor less than 0.1. Moreover, the secondary strong nitrogen limitation occurs in April. Like diatoms, nitrogen limitation for non-diatoms is also strong in November and less intense in April. In November, strong nitrogen limitation is because nitrate is exhausted by phytoplankton uptake during the SE monsoon (June-August).

Like station B1, diatoms at station B2 are also nitrogen-limited throughout the year (Figure 6.4). However, compared to station B1, diatoms at station B2 are more nitrogen-limited, as indicated by a higher ratio of phosphorus and silica limitation to nitrogen at station B2 (Figure 6.4b, c). Additionally, unlike station B1, non-diatoms at station B2 are nitrogen-limited over the whole year.

Overall, diatoms and non-diatoms are generally nitrogen-limited at both stations. The nitrogen limitation is strong in April and November. However, the nitrogen limitation is weak in January-February and during the SE monsoon (June-August). The weak nitrogen limitation in January-February at station B2 is mainly related to the horizontal intrusion of high-nitrate water from the eastern

Banda Sea. Meanwhile, the weak nitrogen limitation during the SE monsoon is associated with the vertical advection of high-nitrate water.

In addition to nutrients, another factor limiting the phytoplankton growth is light and temperature. For example, Figure 6.5 shows that the light-dependent growth rate of phytoplankton (Equation 3.10) at the surface of station B1 is relatively high during both the NW and SE monsoons. Moreover, the light-dependent growth rate at the surface is relatively low during transition monsoons in April and October. Unlike station B1, the light-dependent growth rate at station B2 reaches the maximum during the NW monsoon, only in December-January (Figure 6.6). A second maximum cannot be seen. Additionally, the light-dependent growth rate is relatively low during the SE monsoon and the second transition monsoons (June-October).

The low light-dependent growth rate at station B2 during the SE monsoon is related to the pseudo motion of the sun. Since station B2 is located in the southern hemisphere, it receives less sun radiation during the boreal summer in June-October. As a result, the surface temperature factor at station B2 is also low during boreal summer (Figure 6.6). A similar variation of surface temperature factor is also found at station B1, as it is also located in the southern hemisphere (Figure 6.5).

6.3 Processes affecting phytoplankton production

6.3.1 Biological processes

The previous Section 6.2 has explained the seasonal variation of limiting factors in the Arafura Sea. It is expected that the seasonal change in limitation factors reflects the change in phytoplankton growth. The following section elucidates the change in phytoplankton growth and its related biological processes in the Arafura Sea.

The seasonal variation of phytoplankton production integrated over the whole water column at station B1 is shown by Figure 6.7a. In general, diatom production shows a more distinct seasonal variation than for non-diatoms, and its variation follows the pattern of nitrogen limitation (compare Figures 6.3 and 6.7). Furthermore, diatoms mainly modulate the total phytoplankton production, indicated by a similar seasonal variation between diatoms and total phytoplankton production. The annual mean of diatom production is 2.86 mmol N m^{-2} d^{-1}. Unlike diatoms, non-diatom production at station B1 is less varying throughout the year, with a relatively high value in October–November. Nevertheless, as the mean over the year, non-diatom production is higher than for diatom, which is 3.24 mmol N m^{-2} d^{-1}.

Figure 6.7a shows that the total phytoplankton production reaches its minimum in April, coinciding with strong nitrogen limitation (compare Figures 6.3 and 6.7). From April to July, the total production rapidly increases, associating with nutrient input during this period. In July, the total phytoplankton production increases and reaches its maximum in October, around 8 mmol N m^{-2} d^{-1}. From October to

December, the total phytoplankton production slightly declines.

In addition to phytoplankton production, Figure 6.7b also shows zooplankton grazing on phytoplankton. In the ECOHAM setting used in the present study, mesozooplankton consume diatoms while microzooplankton consumes non-diatoms. The simulation result shows that at station B1, the amount of microzooplankton grazing on non-diatoms is mainly higher than mesozooplankton grazing on diatoms.

The simulation result also shows that the mesozooplankton grazing on diatoms has a similar variation to the total phytoplankton production (Figure 6.7). The low mesozooplankton grazing on diatoms occurs in April, coinciding with low diatom production. Meanwhile, the zooplankton (microzooplankton and mesozooplankton) grazing peaks occur in August, one month after the peak of diatom production, and in December. Furthermore, the increase of zooplankton grazing in November-December resulted in decline in phytoplankton production during this period. Based on these results, station B1 shows bottom-up control in July–August and top-down control in November–December within the zooplankton-phytoplankton system.

Zooplankton grazing is one of the external factors for phytoplankton loss. Another factor that is worth considering is the internal factor, which is the phytoplankton biological losses. The latter comprises mortality and exudation. Figure 6.7c shows the difference between the production and biological losses, which is referred to as the net phytoplankton growth. The positive value indicates that the phytoplankton production is larger than biological losses and vice versa. Generally, the net growth is positive throughout the year for both diatom and non-diatom. The net growth of diatoms is at a minimum in May, one month after the minimum of diatom production. From May to September, the net growth of diatoms increases and reaches the maximum in September. Meanwhile, the peak of non-diatom net growth occurs one month later, in October.

By contrast, the phytoplankton production at station B2 shows an inverse pattern compared to station B1 (Figure 6.8). At station B2, non-diatom production is higher than for diatom, with lower production in SE than NW monsoon. Figure 6.8a shows that phytoplankton production has two peaks in January and May. In January, the first peak of phytoplankton production is related to nutrient supply via horizontal intrusion from the Banda Sea (compare Figures 5.4 and 6.8). From January to April, the phytoplankton production decreases due to zooplankton grazing. However, from April to May, phytoplankton production increases due to the vertical flux of nitrate. The vertical nitrate input continuously increases until the end of June (compare Figures 5.10 and 6.8).

Although nitrate is continuously supplied, the total phytoplankton production declines from May to July by about 4 mmol N m^{-2} d^{-1}. The total phytoplankton production remains below 2 mmol N m^{-2} d^{-1} until November. It is expected that a decline of phytoplankton production during this period is due to depleted nutrients and strong grazing pressure. As shown in Figure 6.8, the variation of zooplankton

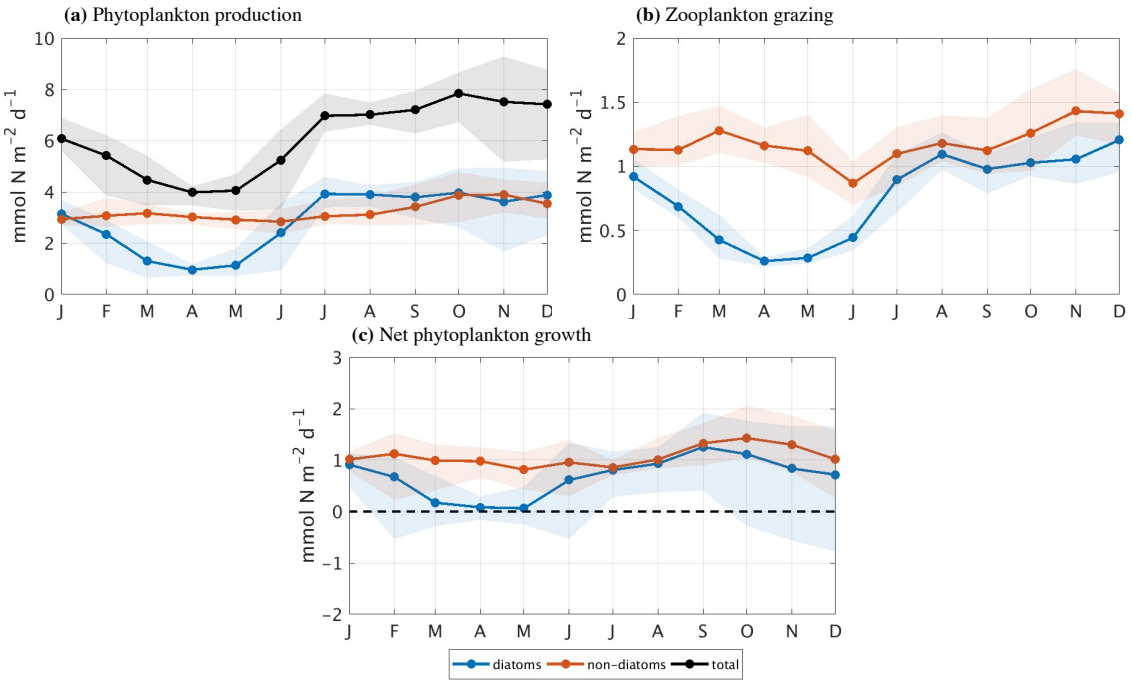

Figure 6.7: Time series of (a) phytoplankton production; (b) zooplankton grazing (mesozooplankton upon diatoms and microzooplankton upon non-diatoms); (c) net phytoplankton growth (production minus biological losses) at station B1 (Figure 3.5). The shaded plot indicates a one-month range. All values were integrated over the whole water column (37 m).

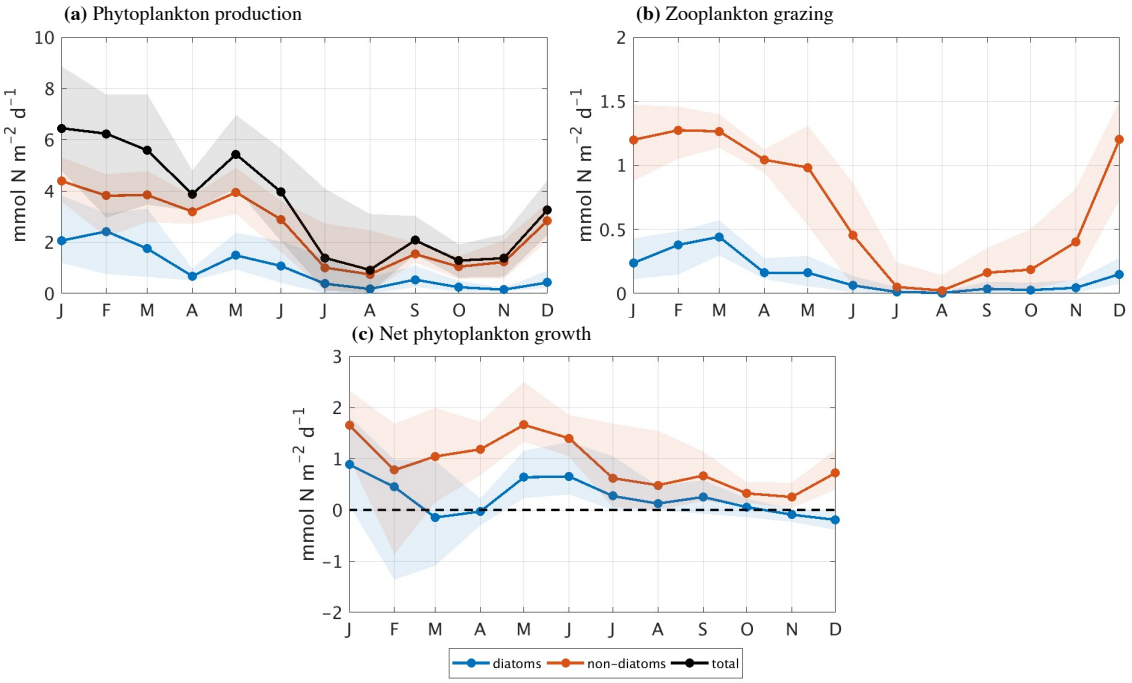

Figure 6.8: Time series of (a) phytoplankton production; (b) zooplankton grazing (mesozooplankton upon diatoms and microzooplankton upon non-diatoms); (c) net phytoplankton growth (production minus biological losses) at station B2 (Figure 3.5). The shaded plot indicates a one-month range. All values were integrated over the whole water column (130 m).

grazing is similar to phytoplankton production. For example, the microzooplankton grazing on non-diatoms is higher during the NW monsoon.

In addition to grazing pressure, Figure 6.8 also shows that the net growth of phytoplankton is lower during the SE monsoon. The net growth of non-diatoms is positive throughout the year, with two peaks in January and May, coinciding with the maximum of non-diatom production. However, unlike non-diatoms, the net growth of diatoms is negative in March and from November to December. The negative net growth for diatoms indicates the decline of diatom concentration during these periods.

Overall, the simulation shows that the phytoplankton production and growth at station B2 are mainly regulated by nitrogen availability rather than grazing pressure. The results indicate that weak nitrogen limitation coincides with high phytoplankton production and vice versa. Additionally, the dominance of non-diatoms at station B2 is related to nitrate availability. As nitrate in the near-surface layer at station B2 is low, diatom production declines. However, non-diatoms thrive and can produce over the year, as they effectively take up ammonium, whereby this condition stimulates zooplankton growth.

6.3.2 Hydrodynamic processes

In addition to biological processes, it is also important to consider hydrodynamic processes that change phytoplankton concentration locally. In ECOHAM, the hydrodynamic processes involve advection and mixing in lateral/horizontal and vertical directions. Note that the horizontal mixing component is not presented because it is two orders of magnitude smaller than other hydrodynamic components. Hence, horizontal mixing is not considered in the following discussion.

This section presents the hydrodynamic fluxes of nitrogen as an element within diatom and non-diatom (Figures 6.9 and 6.10). As previously mentioned in Section 6.1, nitrogen is chosen for consistency of the unit used for the discussion of nutrient and phytoplankton dynamics. The hydrodynamic fluxes are calculated for the upper 10 m, representing the fluxes of the near-surface layer. Positive values indicate the fluxes to the near-surface layer, increasing phytoplankton concentration in the upper 10 m. By contrast, negative values indicate a decrease of phytoplankton concentration due to hydrodynamic processes in the upper 10 m.

Figure 6.9 shows that phytoplankton concentration change due to vertical advection almost compensates for the change due to horizontal advection. For example, the horizontal advection fluxes are positive in January and February, indicating that phytoplankton concentration should increase due to horizontal advection (Figure 6.9a). By contrast, the vertical advection fluxes are negative during the same period, with similar magnitudes as shown in Figure 6.9b. During the beginning of the SE monsoon, vertical advection flux is positive. However, during the same period, the horizontal flux of phytoplankton concentration is

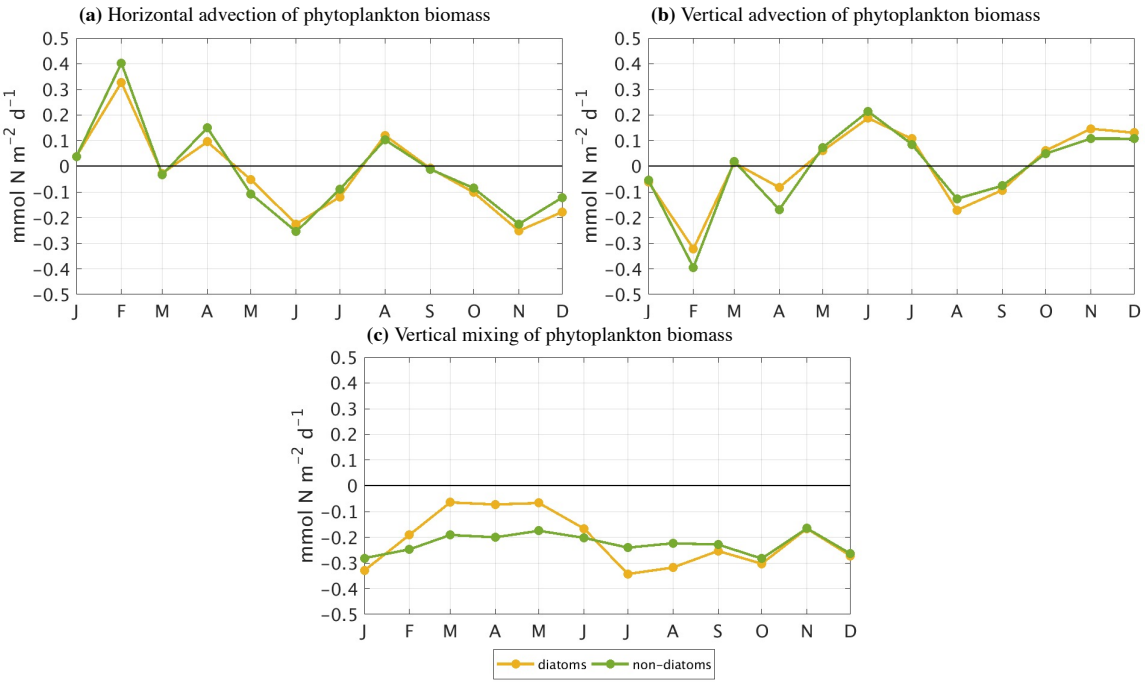

Figure 6.9: Time series of (a) horizontal advection; (b) vertical advection; (c) vertical mixing components for diatoms and non-diatoms concentration at station B1 (Figure 3.5). All values were calculated for the upper 10 m.

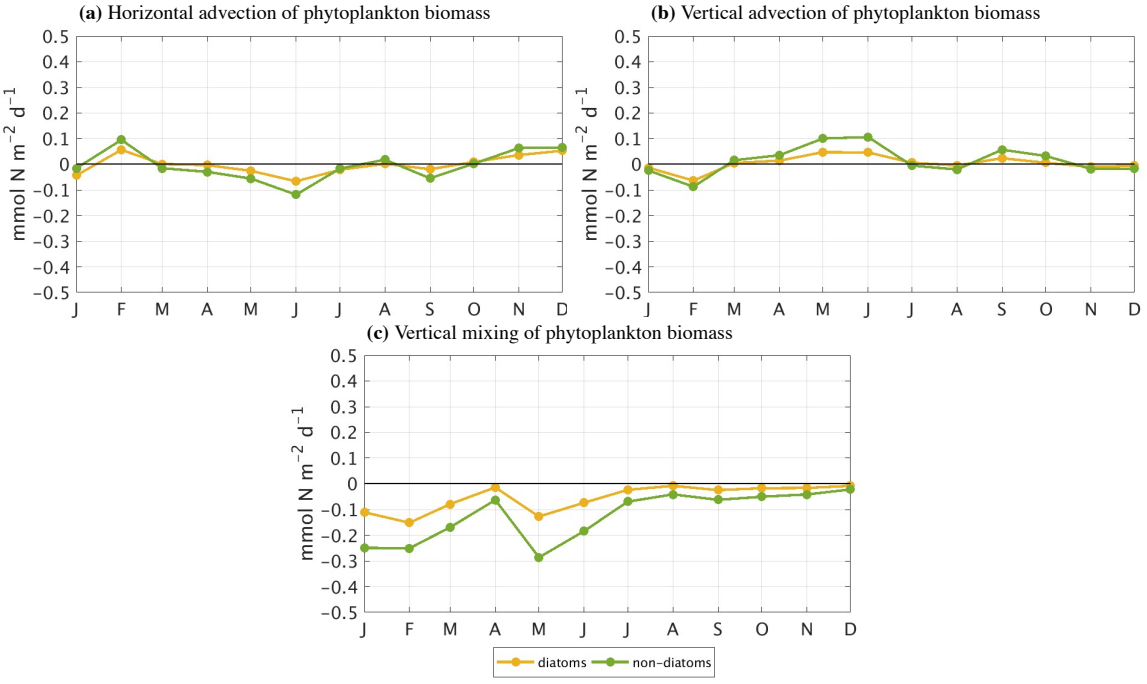

Figure 6.10: Time series of (a) horizontal advection; (b) vertical advection; (c) vertical mixing components for diatoms and non-diatoms concentration at station B2 (Figure 3.5). All values were calculated for the upper 10 m.

negative. Furthermore, unlike advection, the vertical mixing terms are negative throughout the year. The diatom concentration change due to mixing is relatively large in July–September and small in March-May.

The hydrodynamic fluxes of the near-surface layer at station B2 are generally lower than at station B1 (Figure 6.10). Like station B1, the change of phytoplankton concentration due to horizontal advection is almost compensated by the vertical advection. For example, at station B2, two periods of positive vertical advection fluxes coincide with negative horizontal advection fluxes in March–July and September–October. Moreover, like station B1, the vertical mixing at station B2 is also negative over the whole year. The magnitude of vertical mixing of non-diatoms is generally higher than the magnitude related to diatoms, which reaches its maximum in May.

Overall, the total of hydrodynamic fluxes, the sum of the advection (horizontal + vertical) and mixing, are smaller than the biological fluxes (see Section 6.3.1). The annual mean of total hydrodynamic fluxes at station B1 for diatoms and non-diatoms are 0.75 and 0.82 mmol N m^{-2} d^{-1}, respectively. These hydrodynamic fluxes are even smaller at station B2, which are 0.20 and 0.42 mmol N m^{-2} d^{-1} for diatoms and non-diatoms, respectively. These numbers are lower than the value range in biological processes. Therefore, in terms of magnitude, the contribution of hydrodynamic processes to phytoplankton concentration is significantly lower than the biological processes.

6.4 Vertical distribution of phytoplankton

The combined effect of nutrient and light limitations in the whole water column controls the vertical distribution of phytoplankton. Light is often not limiting phytoplankton in the euphotic zone, particularly in relatively clear waters. In this layer, the distribution of phytoplankton mainly depends on nutrients. Hence, phytoplankton concentration is relatively high in the euphotic zone and decreasing with depth, as shown in Figures 6.11 and 6.12.

Figure 6.11b shows that diatom concentration at station B1 is higher than for non-diatom in the whole water column. Diatom (non-diatom) concentration is also higher by about 1 mmol N m^{-3} (0.5 mmol N m^{-3}) in July than in January. The result is in good agreement with previous studies that showed a higher phytoplankton abundance during the SE monsoon (*Gieskes et al.*, 1988; *Adnan*, 1990; *Wetsteyn et al.*, 1990; *Ilahude et al.*, 1990). Moreover, 6.11b also shows that diatom concentration in July is about 0.97 mmol N m^{-3} at the surface and slightly decreasing to 0.9 mmol N m^{-3} in the bottom layer. Similar to diatom, non-diatom concentration in July also decreases with depth, which is about 0.78 mmol N m^{-3} at the surface to 0.7 mmol N m^{-3} in the bottom layer.

The concentration of Chl-a at station B1 is also higher in July than in January, as shown in Figure 6.11a. However, unlike phytoplankton concentration, the Chl-a increases with depth. The increasing Chl-a associates with the chlorophyll to carbon ratio (Chl:C). As light reduces with depth, phytoplankton adapts by increasing its cellular photosynthetic pigment, which is Chl-a. By contrast, the

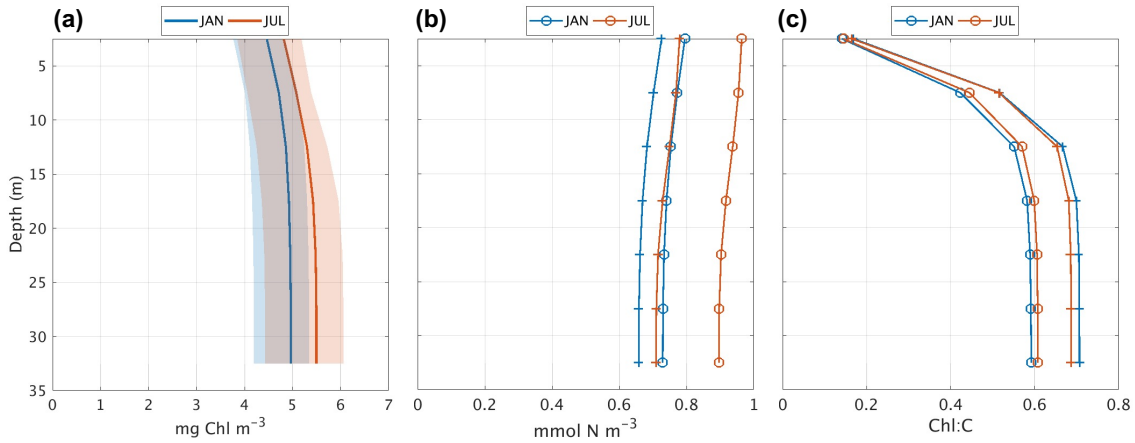

Figure 6.11: Vertical profile of (a) Chl-a (shaded plot indicates a one-month range); (b) phytoplankton concentration; (c) Chl-a to carbon ratio (Chl:C) at station B1 (Figure 3.5) in January (blue) and July (red) 2014. The lines with a circle (∘) and a plus (+) markers in Figures (b) and (c) indicate diatoms and non-diatoms, respectively.

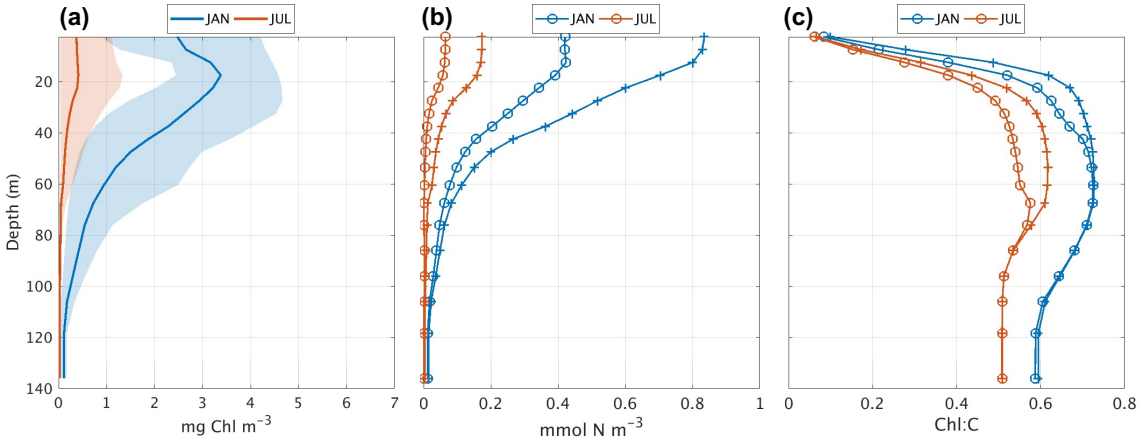

Figure 6.12: Vertical profile of (a) Chl-a (shaded plot indicates a one-month range); (b) phytoplankton concentration; (c) Chl-a to carbon ratio (Chl:C) at station B2 (Figure 3.5) in January (blue) and July (red) 2014. The lines with a circle (∘) and a plus (+) markers in Figures (b) and (c) indicate diatoms and non-diatoms, respectively.

same pigment concentration decreases under high light conditions; for example, at the surface (*Dubinsky and Stambler*, 2009). Such a mechanism is known as photoacclimation (*Moore et al.*, 2006; *Dubinsky and Stambler*, 2009). Figure 6.11c shows that the chlorophyll to carbon ratio of non-diatoms is higher than for diatoms, and the ratio rapidly increases from the surface to 15 m. From 15 m to the bottom layer, the Chl:C ratio is constant.

The difference in the Chl:C ratio between diatoms and non-diatoms is highly influenced by environmental factors, such as light, temperature, and nutrients (*Chan*, 1980; *Cloern et al.*, 1995). Both diatoms and non-diatoms at station B1 are exposed to the same temperature conditions. Hence, the Chl:C ratio difference is modulated by either the light or nutrient limitation for diatoms and non-diatoms (Equation 3.35). In the present study, the Chl:C ratio is based on the empirical approach from *Cloern et al.* (1995) where the presence of chlorophyll causes

self-shading and reduces light availability. In the same light condition, as non-diatom concentration is lower than for diatoms, the self-shading of non-diatoms is also low. Hence, non-diatoms increase the chlorophyll pigment because they receive more light than diatoms. Additionally, the Chl:C difference between diatoms and non-diatoms is also influenced by nutrients. As previously described in Section 6.2, nutrient (nitrogen and phosphorus) limitation is weaker for non-diatoms than diatoms. According to Equation 3.35, for the same nutrient conditions, non-diatoms will have a higher nutrient limitation factor (lim_nps), and thus a higher Chl:C ratio.

In addition to station B1, the vertical phytoplankton distribution at station B2 is also presented (Figure 6.12). Like station B1, the phytoplankton concentration at station B2 decreases with depth (Figure 6.12b). However, in contrast to station B1, the phytoplankton concentration is higher in January than in July. Additionally, the non-diatom concentration is also higher than for diatom. Such seasonal variation has previously been described in Section 6.3.1, which showed a low phytoplankton production and net growth during the SE monsoon. Figure 6.12b also shows that non-diatom concentration in January is about 0.84 mmol N m^{-3} at the surface and decreases to less than 0.1 mmol N m^{-3} at 80 m. Moreover, non-diatom concentration is lower in July, which is less than 0.2 mmol N m^{-3} in the whole water column.

In line with higher phytoplankton concentration, the Chl-a concentration at station B2 is also higher in January than in July. Figure 6.12a also shows a DCM, up to 3.4 mg Chl m^{-3}, in 18 m. By contrast, the DCM is absent in July, where the Chl-a concentration in the whole water column is less than 0.5 mg Chl m^{-3}. Additionally, the Chl:C ratio for both diatoms and non-diatoms in both seasons rapidly increases from the surface to around 20 m (Figure 6.12c). Such a rapid increase of the Chl:C ratio within this depth interval is due to photoacclimation.

Figure 6.12c shows that the Chl:C ratio for diatoms and non-diatoms in both seasons at station B2 slowly increases from 20 to 60 m. Within this depth interval, phytoplankton concentration rapidly decreases due to less light. Phytoplankton increases the chlorophyll pigment to adapt with less light, but it is less significant than in the upper 20 m. Furthermore, from 60 m to the bottom layer, the Chl:C ratio decreases. Within this depth interval, phytoplankton concentration significantly decreases. As no more light is available to support growth, the chlorophyll cells of phytoplankton also decrease.

7 Final discussion

1) How do advection and mixing affect the nutrient supply in the Arafura Sea?

The advection and mixing affect nutrient supply differently between the shallow region in the northern part (Sahul Shelf) and the continental slope of the Arafura Sea. In the Sahul Shelf, nitrate concentration is higher in July than in January, which agrees with previous studies (*Gieskes et al.*, 1988; *Adnan*, 1990; *Ilahude et al.*, 1990; *Wetsteyn et al.*, 1990; *Condie*, 2011). Nitrate concentration is relatively homogenous from the surface to the bottom layer, indicating a well-mixed water column. In the Sahul Shelf, vertical mixing is the primary process that transports nitrate to the near-surface layer (the upper 10 m). The nitrate input via vertical advection is weak from January to May and relatively strong from June onwards (the SE monsoon). The strong vertical mixing during the SE monsoon has also been previously described by *Zijlstra et al.* (1990).

In the continental slope area of the Arafura Sea, in the south of the Tanimbar Islands, advection is the primary process that supplies nitrate. The simulation reveals the horizontal intrusion of nitrate-rich water from the eastern Banda Sea in the layer above the nitracline during the NW monsoon. However, this nitrate-rich water is mostly transported downward due to a relatively strong downward vertical advection during this period. It represents downwelling that is mainly observed during the NW monsoon, as previously described by previous studies (*Wyrtki*, 1961; *Zijlstra et al.*, 1990; *Gordon and Susanto*, 2001). On the other hand, the vertical advection is upward, supplying nitrate to the layer above the nitracline during the SE monsoon. It represents the upwelling that typically occurs during the SE monsoon in the Arafura Sea, as suggested by previous studies (*Wyrtki*, 1961; *Zijlstra et al.*, 1990; *Gordon and Susanto*, 2001; *Condie*, 2011; *Kämpf*, 2015).

Additionally, the predominantly northward nitrate transport is found along the continental slope during the SE monsoon. This indicates the nutrient enrichment of the northern Arafura Sea (Sahul Shelf) during this period via vertical and horizontal advection. This result complements previous studies by *Zijlstra et al.* (1990), which only address the vertical advection as the nitrate source during the SE monsoon.

2) Which processes control the nutrient budget in the Arafura Sea?

In the Sahul Shelf, the nitrate budget in the near-surface layer is mainly regulated by vertical mixing, advection, and phytoplankton uptake. The vertical advection and mixing are the primary sources of nitrate, while nitrate supply via

atmospheric deposition is significantly low. In the near-surface layer, the primary loss of nitrate is due to phytoplankton uptake, mainly diatoms. Those processes, which regulate nitrate concentration, elevate during the SE monsoon. Moreover, the deeper layer receives nitrate mainly via horizontal advection and nitrification. Like the near-surface layer, those processes also increase during the SE monsoon. Additionally, the nitrate concentration in a deeper layer mainly decreases due to vertical advection. In this layer, the nitrate uptake by phytoplankton is significantly lower than in the near-surface layer.

The primary processes that control the nutrient budget in the continental slope of the Arafura Sea are advection and mixing. Compared with the Sahul Shelf, the nutrient budget in the continental slope shows a stronger seasonal variation. For instance, during the NW monsoon, the dominant source of nitrate in the layer above the nitracline (the upper 64 m) is horizontal advection. By contrast, during the SE monsoon, the primary source of nitrate to the layer above the nitracline is vertical advection. In both seasons, phytoplankton uptake plays a role in reducing nitrate concentration in the layer above the nitracline. Unlike the Sahul Shelf, the nitrate uptake by diatoms and non-diatoms in the continental slope area has similar magnitudes.

Advection and mixing also regulate the nitrate budget in the layer below the nitracline ($>$ 64 m depth). However, the layer below the nitracline shows a different dominant process and stronger seasonality than the layer above the nitracline. For example, during the SE monsoon, the nitrate concentration increases due to horizontal advection. The increase in nitrate concentration is expected due to the eastward undercurrent, which transports nitrate-rich water from a subsurface layer of the eastern Banda Sea. This undercurrent mechanism was previously suggested by *Kämpf* (2015).

3) What are the controlling factors for phytoplankton growth in the Arafura Sea?

The simulation shows that diatom concentration in the SE monsoon is mainly higher than for non-diatoms in the Sahul Shelf, which agrees with *Adnan* (1990) and *Condie* (2011). This is related to higher net growth (production minus biological losses) in the SE monsoon. The higher phytoplankton growth is primarily stimulated by the increase of nutrient supply during the SE monsoon, as indicated by weak nutrient limitations. As phytoplankton production increases in May-July, it is followed by the increase of zooplankton grazing, suggesting bottom-up control during this period. However, phytoplankton production decreases in October-December. During this period, the zooplankton grazing is relatively high, indicating top-down control in the zooplankton-phytoplankton system.

In the continental slope area, phytoplankton growth is strongly regulated by nitrogen availability. In this region, nitrate concentration in the near-surface layer is deficient. This condition indicates a strong nitrate limitation for phytoplankton, which agrees with the study by *Zevenboom and Wetsteyn* (1990). Such a nitrate

limitation is stronger for diatom than non-diatom, leading to a decline in diatom production. On the other hand, non-diatoms thrive by consuming ammonium more effectively, as indicated by weak ammonium limitation for non-diatoms. Therefore, non-diatom production is maintained throughout the year.

8 Conclusion

This study has investigated the mechanisms of nutrient supply and controlling factors of phytoplankton growth in the Arafura Sea using a three-dimensional ECOHAM biogeochemical model. The modeling study reveals different mechanisms of nutrient supply between the shallow region (Sahul Shelf) and the continental slope of the Arafura Sea. In the Sahul Shelf, nitrate is primarily transported to the near-surface layer by vertical mixing, and it is stronger during the southeast (SE) monsoon, as also confirmed by the nitrate budget analysis. On the other hand, the primary nitrate source is different between the layer above and below the nitracline in the continental slope area. During the northwest (NW) monsoon, the horizontal intrusion of nitrate-rich water masses from the eastern Banda Sea is found in the layer above the nitracline. However, this nitrate-rich water mass is mainly transported downward due to downwelling. As a result, nitrate concentration initially increases for one month in January, but it declines a few months later. Again, the nitrate budget analysis also confirms this. Furthermore, during the SE monsoon, the eastward undercurrent transports nitrate-rich water from the subsurface layer of the Banda Sea. This nitrate-rich water is transported to the layer above the nitracline via vertical advection or upwelling, confirmed by nitrate budget analysis.

Generally, the phytoplankton growth in the Sahul Shelf and continental slope area of the Arafura Sea is strongly regulated by nitrogen limitation. The seasonal variation of phytoplankton production and zooplankton grazing suggests the bottom-up control during the peak of upwelling (June-August) and top-down control in October-December. In the continental slope area, low nitrate concentration leads to a strong nitrate limitation for diatoms. Meanwhile, non-diatoms develop by taking up ammonium effectively.

Altogether, this modeling study contributes to a better understanding of nutrient and phytoplankton dynamics in the Arafura Sea. Indeed, this study has limitations that focus on a seasonal time scale. Additionally, study limitations also arise from the assumption used in the numerical model. Nevertheless, the result of this study is helpful for further research regarding the nutrient and phytoplankton dynamics, particularly in a longer time scale for a climate-related study.

Appendices

A River input derived from WGHM

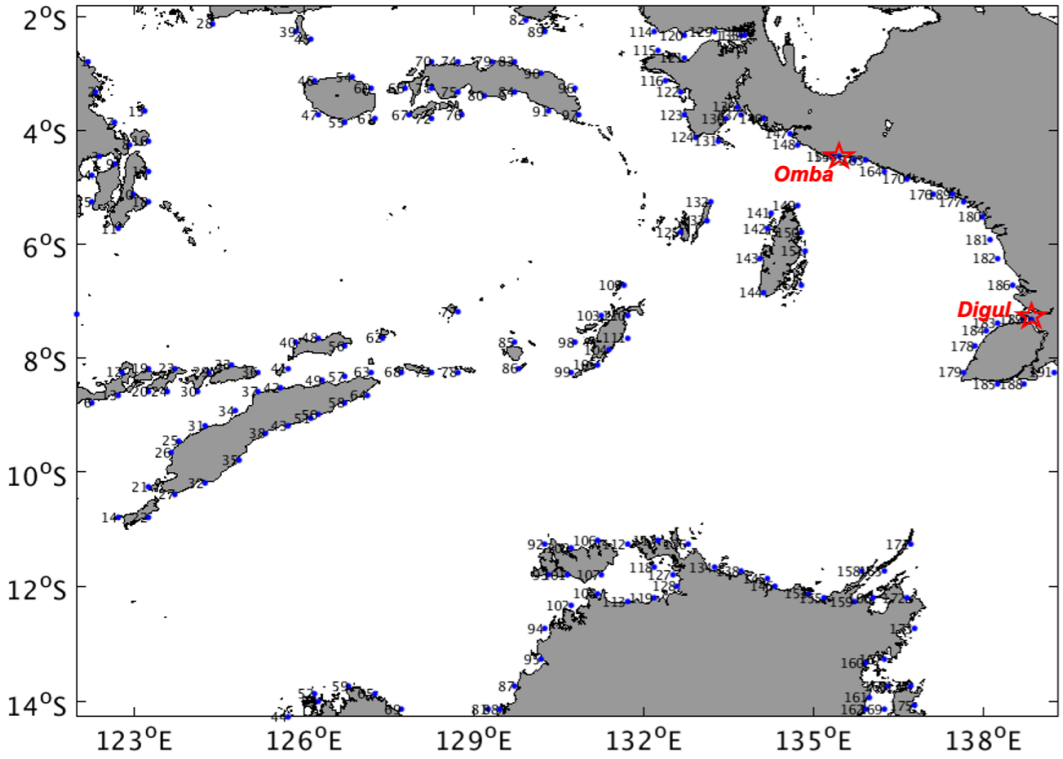

Figure A.1: Location of the river mouth that indicated by the blue dots (•). The locations of Omba and Digul Rivers are indicated by the red stars.

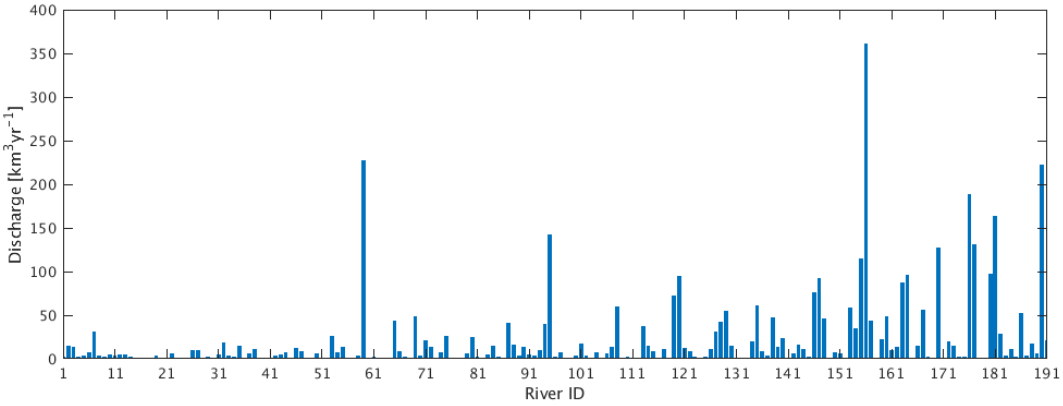

Figure A.2: Mean freshwater discharge of each river from the period of 1990–2014.

B ECOHAM state variables and equations

ECOHAM consists of 31 prognostic state variables, 6 derived state variables, and 5 prognostic benthic state variables. The complete list of pelagic state variables is given by Table B.1.

Table B.1: List of ECOHAM state variables (*Große et al.*, 2018).

No	Var code	Variable description	Unit
pelagic state variables: prognostic			
1	xix	Passive tracer	m^{-3}
2	alk	Alkalinity	meq m^{-3}
3	dic	Dissolved inorganic carbon (DIC)	mmol C m^{-3}
4	$n3n$	Nitrate NO_3^-	mmol N m^{-3}
5	$n4n$	Ammonium NH_4^+	mmol N m^{-3}
6	$n1p$	Phosphate PO_4^{3-}	mmol P m^{-3}
7	$n5s$	Silicate $SiOx$	mmol Si m^{-3}
8	$p1c$	Diatom-C	mmol C m^{-3}
9	$p1n$	Diatom-N	mmol N m^{-3}
10	$p1p$	Diatom-P	mmol P m^{-3}
11	$p1s$	Diatom-Si	mmol Si m^{-3}
12	$p2c$	Non-diatom-C	mmol C m^{-3}
13	$p2n$	Non-diatom-N	mmol N m^{-3}
14	$p2p$	Non-diatom-P	mmol P m^{-3}
15	psk	Non-diatom-$CaCO_3$	mmol C m^{-3}
16	$z1c$	Microzooplankton-C	mmol C m^{-3}
17	$z2c$	Mesozooplankton-C	mmol C m^{-3}
18	bac	Bacteria-C	mmol C m^{-3}
19	$d1c$	Detritus-C (slowly sinking)	mmol C m^{-3}
20	$d1n$	Detritus-N (slowly sinking)	mmol N m^{-3}
21	$d1p$	Detritus-P (slowly sinking)	mmol P m^{-3}
22	$d2c$	Detritus-C (fast sinking)	mmol C m^{-3}
23	$d2n$	Detritus-N (fast sinking)	mmol N m^{-3}

24	*d2p*	Detritus-P (fast sinking)	mmol P m^{-3}
25	*d2s*	Detritus-Si (fast sinking)	mmol Si m^{-3}
26	*d2k*	Detritus skeleton-$CaCO_3$ (fast sinking)	mmol C m^{-3}
27	*soc*	Semi-labile dissolved organic matter	mmol C m^{-3}
28	*doc*	Labile dissolved organic carbon (DOC)	mmol C m^{-3}
29	*don*	Labile dissolved organic nitrogen (DON)	mmol N m^{-3}
30	*dop*	Labile dissolved organic phosphorus (DOP)	mmol P m^{-3}
31	*o2o*	Dissolved oxygen (O_2)	mmol O_2 m^{-3}
pelagic state variables: derived			
1	*ban*	Bacteria-N	mmol N m^{-3}
2	*bap*	Bacteria-P	mmol P m^{-3}
3	*z1n*	Microzooplankton-N	mmol N m^{-3}
4	*z1p*	Microzooplankton-P	mmol P m^{-3}
5	*z2n*	Mesozooplankton-N	mmol N m^{-3}
6	*z2p*	Mesozooplankton-P	mmol P m^{-3}
benthic state variables: prognostic			
1	*sd_poc*	Benthic particulate organic matter C	mmol C m^{-3}
2	*sd_pon*	Benthic particulate organic matter N	mmol N m^{-3}
3	*sd_pop*	Benthic particulate organic matter P	mmol P m^{-3}
4	*sd_pos*	Benthic particulate organic matter SiO_x	mmol Si m^{-3}
5	*sd_pok*	Benthic particulate organic matter $CaCO_3$	mmol C m^{-3}

Table B.2: ECOHAM equations. The SOURCES indicates by blue text and SINKS indicates by red text (further details in *Lorkowski et al.* (2012) and *Große et al.* (2018)).

State variable	Conservation equation
Diatoms-C	$\frac{\partial p1c}{\partial t} = dic\_p1c - p1c\_z1c - p1c\_z2c - p1c\_d1c - p1c\_d2c - p1c\_doc - p1c\_soc$
Diatoms-N	$\frac{\partial p1n}{\partial t} = n3n\_p1n + n4n\_p1n - p1n\_z1n - p1n\_z2n - p1n\_d1n - p1n\_d2n - p1n\_don$
Diatoms-P	$\frac{\partial p1p}{\partial t} = n1p\_p1p - p1p\_z1p - p1p\_z2p - p1p\_d1p - p1p\_d2p - p1p\_dop$
Diatoms-Si	$\frac{\partial p1s}{\partial t} = n5s\_p1s - p1s\_d2s$
Non-Diatoms-C	$\frac{\partial p2c}{\partial t} = dic\_p2c - p2c\_z1c - p2c\_z2c - p2c\_d1c - p2c\_d2c - p2c\_doc - p2c\_soc$
Non-Diatoms-N	$\frac{\partial p2n}{\partial t} = n3n\_p2n + n4n\_p2n - p2n\_z1n - p2n\_z2n - p2n\_d1n - p2n\_d2n - p2n\_don$
Non-Diatoms-P	$\frac{\partial p2p}{\partial t} = n1p\_p2p - p2p\_z1p - p2p\_z2p - p2p\_d1p - p2p\_d2p - p2p\_dop$
Non-Diatoms-$CaCO_3$	$\frac{\partial psk}{\partial t} = dic\_psk - psk\_z1c - psk\_z2c - psk\_d2k$
Microzooplankton-C	$\frac{\partial z1c}{\partial t} = p1c\_z1c + p2c\_z1c + bac\_z1c + d1c\_z1c - z1c\_z2c - z1c\_d1c - z1c\_d2c - z1c\_doc - z1c\_dic$
Microzooplankton-N	$\frac{\partial z1n}{\partial t} = p1n\_z1n + p2n\_z1n + ban\_z1n + d1n\_z1n - z1n\_z2n - z1n\_d1n - z1c\_d2n - z1c\_don - z1c\_n4n$
Microzooplankton-P	$\frac{\partial z1p}{\partial t} = p1p\_z1p + p2p\_z1p + bap\_z1p + d1p\_z1p - z1p\_z2p - z1p\_d1p - z1p\_d2p - z1c\_dop - z1p\_n1p$
Mesozooplankton-C	$\frac{\partial z2c}{\partial t} = p1c\_z2c + p2c\_z2c + bac\_z2c + d1c\_z2c + z1c\_z2c - z2c\_d1c - z2c\_d2c - z2c\_doc - z2c\_dic$
Mesozooplankton-N	$\frac{\partial z2n}{\partial t} = p1n\_z2n + p2n\_z2n + ban\_z2n + d1n\_z2n + z1n\_z2n - z2n\_d1n - z2n\_d2n - z2n\_don - z2c\_n4n$
Mesozooplankton-P	$\frac{\partial z2p}{\partial t} = p1p\_z2p + p2p\_z2p + bap\_z2p + d1p\_z2p + z1p\_z2p - z2p\_d1p - z2p\_d2p - z2p\_dop - z2p\_n1p$
Detritus-C, slowly sinking	$\frac{\partial d1c}{\partial t} = p1c\_d1c + p2c\_d1c + z1c\_d1c + z2c\_d1c - d1c\_z1c - d1c\_z2c - d1c\_doc - sink(d1c)$
Detritus-N, slowly sinking	$\frac{\partial d1n}{\partial t} = p1n\_d1n + p2n\_d1n + z1n\_d1n + z2n\_d1n - d1n\_z1n - d1n\_z2n - d1n\_don - sink(d1n)$

Detritus-P, slowly sinking	$\frac{\partial d1p}{\partial t} = p1p\_d1p + p2p\_d1p + z1p\_d1p + z2p\_d1p - d1p\_z1p - d1p\_z2p - d1p\_dop - sink(d1p)$
Detritus-C, fast sinking	$\frac{\partial d2c}{\partial t} = p1c\_d2c + p2c\_d2c + z1c\_d2c + z2c\_d2c - d2c\_doc - sink(d2c)$
Detritus-N, fast sinking	$\frac{\partial d2n}{\partial t} = p1n\_d2n + p2n\_d2n + z1n\_d2n + z2n\_d2n - d2n\_don - sink(d2n)$
Detritus-P, fast sinking	$\frac{\partial d2p}{\partial t} = p1p\_d2p + p2p\_d2p + z1p\_d2p + z2p\_d2p - d2p\_dop - sink(d2p)$
Detritus-Si, fast sinking	$\frac{\partial d2s}{\partial t} = p1s\_d2s - d2s\_n5s - sink(d2s)$
Detritus-$CaCO_3$, fast sinking	$\frac{\partial d2k}{\partial t} = psk\_d2k - d2k\_dic - sink(d2k)$
Labile dissolved organic C (LDOC)	$\frac{\partial doc}{\partial t} = p1c\_doc + p2c\_doc + z1c\_doc + z2c\_doc + d1c\_doc + d2c\_doc - doc\_bac + soc\_doc$
Semi-labile dissolved organic C (SDOC)	$\frac{\partial soc}{\partial t} = p1c\_soc + p2c\_soc - soc\_doc$
Labile dissolved organic N (LDON)	$\frac{\partial don}{\partial t} = p1n\_don + p2c\_don + z1n\_don + z2c\_don + d1n\_don + d2n\_don - don\_ban$
Labile dissolved organic P (LDOP)	$\frac{\partial dop}{\partial t} = p1p\_dop + p2p\_dop + z1p\_dop + z2p\_dop + d1p\_dop + d2p\_dop - dop\_bap$
Bacteria-C	$\frac{\partial bac}{\partial t} = doc\_bac - bac\_z1c - bac\_z2c - bac\_dic$
Bacteria-N	$\frac{\partial ban}{\partial t} = don\_ban + n4n\_ban - ban\_z1n - bac\_z2n - ban\_n4n$
Bacteria-P	$\frac{\partial bap}{\partial t} = dop\_bap + n1p\_bap - bap\_z1p - bap\_z2p - bap\_n1p$
Ammonium (NH_4^+)	$\frac{\partial n4n}{\partial t} = ban\_n4n + z1n\_n4n + z2n\_n4n - n4n\_n3n - n4n\_p1n - n4n\_p2n - n4n\_ban + sed\_n4n + atm\_n4n$
Nitrate (NO_3^-)	$\frac{\partial n3n}{\partial t} = n4n\_n3n - n3n\_nn2 - n3n\_p1n - n3n\_p2n - n3n\_brm + atm\_n3n$
Phosphate (PO_4^{3-})	$\frac{\partial n1p}{\partial t} = bap\_n1p + z1p\_n1p + z2p\_n1p - n1p\_p1p - n1p\_p2p - n1p\_bap + sed\_n1p$
Slicate (SiO_x)	$\frac{\partial n5s}{\partial t} = d2s\_n5s - n5s\_p1s + sed\_n5s$

Dissolved inorganic C (DIC)	$\frac{\partial dic}{\partial t} = bac\_dic + z1c\_dic + z2c\_dic + d2k\_dic - dic\_p1c - dic\_p2c - dic\_psk + sed\_dic + sed\_o3c + air\_o2c$
Oxygen (O_2)	$\frac{\partial o2o}{\partial t} = p1c\_o2o + p2c\_o2o - o2o\_z1c - o2o\_z2c - o2o\_bac - o2o\_n4n - o2o\_brm + air\_o2o$
Total alkalinity	$\frac{\partial alk}{\partial t} = 2.(d2k\_dic + psk\_dic - dic\_psk - n4n\_n3n + sed\_o3c) + n3n\_p1n + n3n\_p2n + z1n\_n4n + z2n\_n4n + ban\_n4n - n4n\_p1n - n4n\_p2n - n4n\_ban - atm\_n3n + atm\_n4n + sed\_n4n + n1p\_p1p + n1p\_p2p + n1p\_bap - z1p\_n1p - z2p\_n1p - bap\_n1p - sed\_n1p$
Benthic organic C	$\frac{\partial sd_p oc}{\partial t} = (p1c\_sed + p2c\_sed + d1c\_sed + d2c\_sed - sed\_dic).dz(k0)$
Benthic organic N	$\frac{\partial sd_p on}{\partial t} = (p1n\_sed + p2n\_sed + d1n\_sed + d2n\_sed - sed\_n4n - sed_n n2).dz(k0)$
Benthic organic P	$\frac{\partial sd_p op}{\partial t} = (p1p\_sed + p2p\_sed + d1p\_sed + d2p\_sed - sed\_n1p).dz(k0)$
Benthic opal	$\frac{\partial sd_p os}{\partial t} = (p1s\_sed + d2s\_sed - sed\_n5s).dz(k0)$
Benthic $CaCO_3$	$\frac{\partial sd_p ok}{\partial t} = (d2k\_sed - sed\_o3c).dz(k0)$

C The light extinction coefficient for water

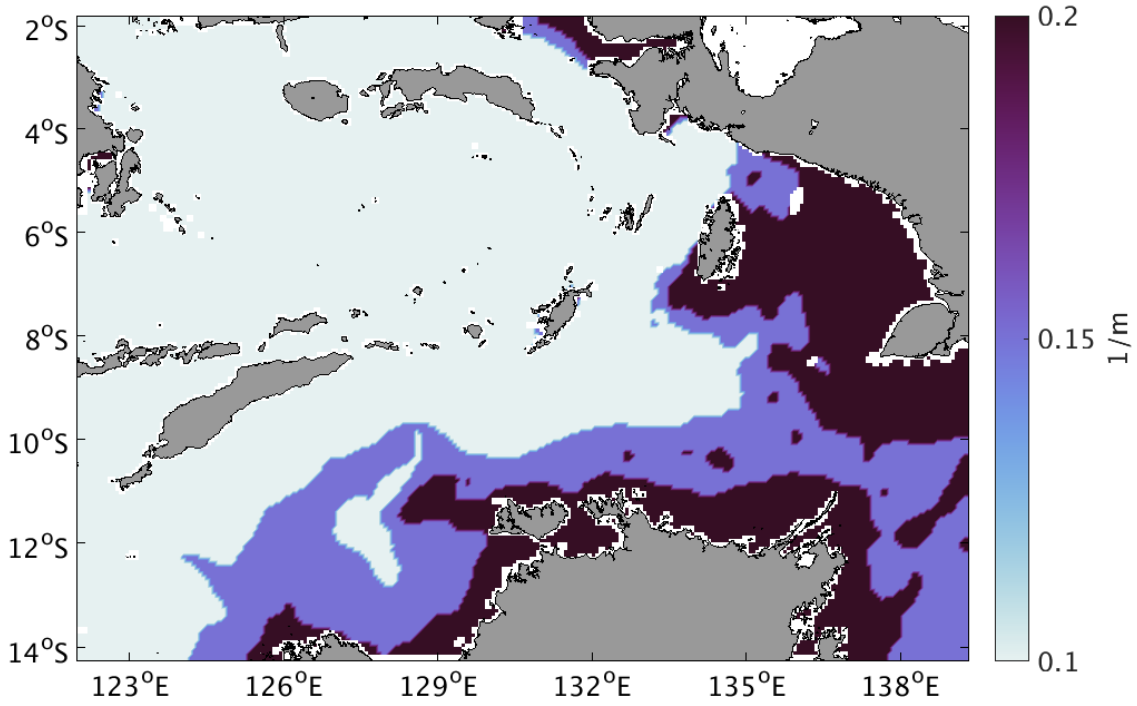

Figure C.1: The spatially varying light extinction coefficient for water.

D Temperature, salinity, and density

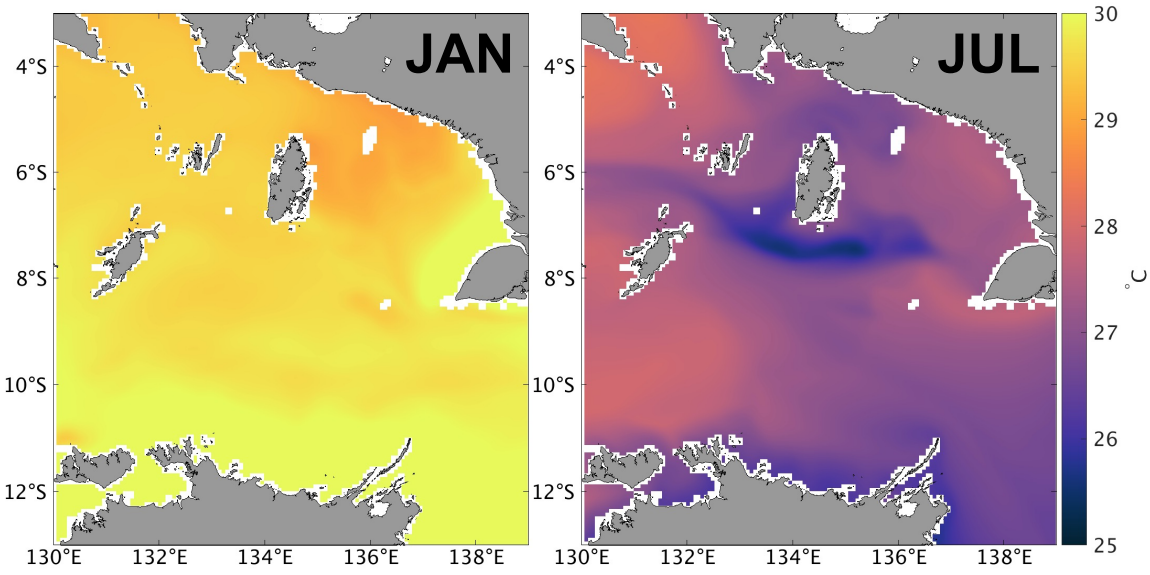

Figure D.1: Distribution of SST in January (left) and July (right) 2014 (see Region B in Figure 3.5).

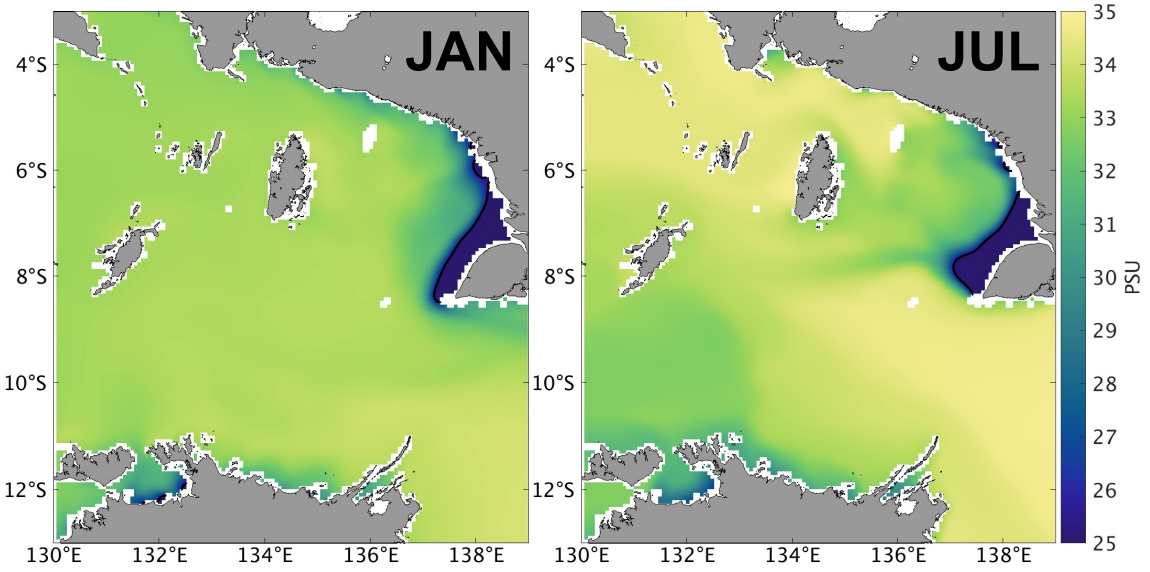

Figure D.2: Distribution of surface salinity in January (left) and July (right) 2014 (see Region B in Figure 3.5). Black contours indicate salinity = 25 PSU.

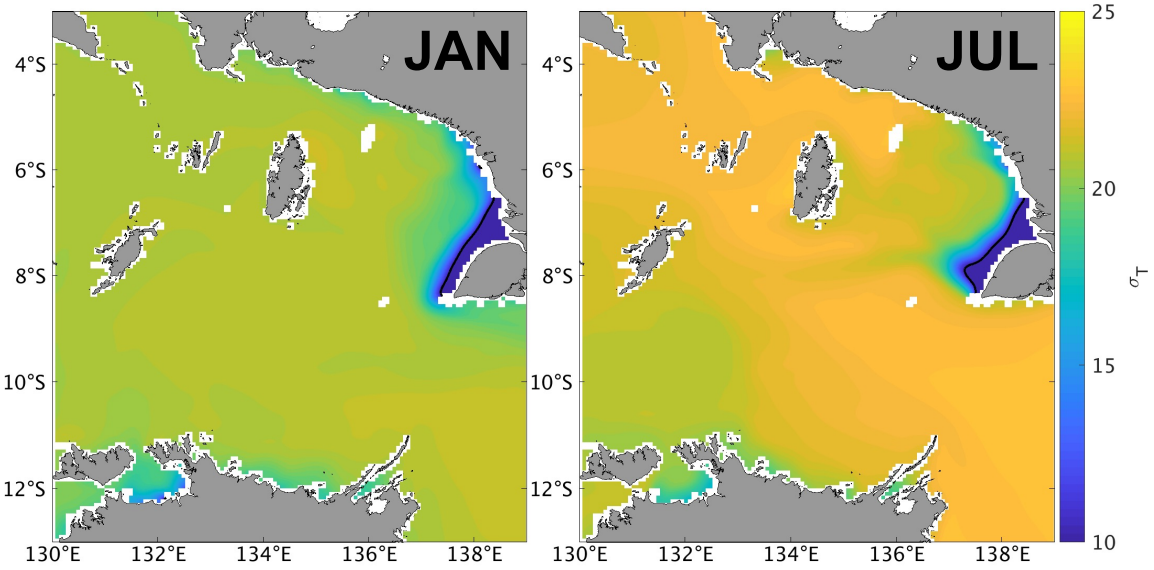

Figure D.3: Distribution of sigma density ($\sigma_T = \rho - 1000$ kg m^{-3}) at the surface in January (left) and July (right) 2014 (see Region B in Figure 3.5). Black contours indicate $\sigma_T = 10$.

Bibliography

Abbas, M. M., A. M. Melesse, L. J. Scinto, and J. S. Rehage (2019), Satellite estimation of chlorophyll-a using Moderate Resolution Imaging Spectroradiometer (MODIS) sensor in shallow coastal water bodies: Validation and improvement, *Water*, *11*(8), doi:10.3390/w11081621.

Adnan, Q. (1990), Monsoonal differences in net-phytoplankton in the Arafura Sea, *Netherlands Journal of Sea Research*, *25*(4), 523–526, doi:10.1016/0077-7579(90)90075-R.

Aldrian, E., and R. D. Susanto (2003), Identification of three dominant rainfall regions within Indonesia and their relationship to sea surface temperature, *International Journal of Climatology*, *23*(12), 1435–1452, doi:10.1002/joc.950.

Aldrian, E., L. D. Gates, and F. H. Widodo (2007), Seasonal variability of Indonesian rainfall in ECHAM4 simulations and in the reanalyses: The role of ENSO, *Theoretical and Applied Climatology*, *87*(1-4), 41–59, doi:10.1007/s00704-006-0218-8.

Alford, M. H., M. C. Gregg, and M. Ilyas (1999), Diapycnal mixing in the Banda Sea: Results of the first microstructure measurements in the Indonesian Throughflow, *Geophysical Research Letters*, *26*(17), 2741–2744, doi:10.1029/1999GL002337.

Alongi, D., K. Edyvane, M. do Ceu Guterres, W. Pranowo, W. Wirasantosa, and R. Wasson (2011), Biophysical profile of the Arafura and Timor Seas, *Tech. rep.*

Alongi, D. M., S. Wirasantosa, T. Wagey, and L. A. Trott (2012), Early diagenetic processes in relation to river discharge and coastal upwelling in the Aru Sea, Indonesia, *Marine Chemistry*, *140–141*, 10–23, doi:10.1016/j.marchem.2012.06.002.

Alongi, D. M., M. da Silva, R. J. Wasson, and S. Wirasantosa (2013a), Sediment discharge and export of fluvial carbon and nutrients into the Arafura and Timor Seas: A regional synthesis, *Marine Geology*, *343*, 146–158, doi:10.1016/j.margeo.2013.07.004.

Alongi, D. M., R. Brinkman, L. A. Trott, F. da Silva, F. Pereira, and T. Wagey (2013b), Enhanced benthic response to upwelling of the Indonesian Throughflow onto the southern shelf of Timor-Leste, Timor Sea, *Journal of Geophysical Research: Biogeosciences*, *118*(1), 158–170, doi:10.1029/2012JG002150.

Armstrong, R. A. (2006), Optimality-based modeling of nitrogen allocation and photoacclimation in photosynthesis, *Deep Sea Research Part II: Topical Studies in Oceanography*, *53*(5), 513–531, doi:10.1016/j.dsr2.2006.01.020.

Baars, M., A. Sutomo, S. Oosterhuis, and O. Arinardi (1990), Zooplankton abundance

in the eastern Banda Sea and northern Arafura Sea during and after the upwelling season, August 1984 and February 1985, *Netherlands Journal of Sea Research*, *25*(4), 527–543, doi:10.1016/0077-7579(90)90076-S.

Bach, L. T., A. J. Paul, T. Boxhammer, E. von der Esch, M. Graco, K. G. Schulz, E. Achterberg, P. Aguayo, J. Arístegui, P. Ayón, I. Baños, A. Bernales, A. S. Boegeholz, F. Chavez, G. Chavez, S.-M. Chen, K. Doering, A. Filella, M. Fischer, P. Grasse, M. Haunost, J. Hennke, N. Hernández-Hernández, M. Hopwood, M. Igarza, V. Kalter, L. Kittu, P. Kohnert, J. Ledesma, C. Lieberum, S. Lischka, C. Löscher, A. Ludwig, U. Mendoza, J. Meyer, J. Meyer, F. Minutolo, J. Ortiz Cortes, J. Piiparinen, C. Sforna, K. Spilling, S. Sanchez, C. Spisla, M. Sswat, M. Zavala Moreira, and U. Riebesell (2020), Factors controlling plankton community production, export flux, and particulate matter stoichiometry in the coastal upwelling system off Peru, *Biogeosciences*, *17*(19), 4831–4852, doi: 10.5194/bg-17-4831-2020.

Backhaus, J. O. (1983), A semi-implicit scheme for the shallow water equations for application to shelf sea modelling, *Continental Shelf Research*, *2*, 243–254, doi: 10.1016/0278-4343(82)90020-6.

Backhaus, J. O. (1985), A three-dimensional model for the simulation of shelf sea dynamics, *Deutsche Hydrografische Zeitschrift*, *38*(4), 165–187.

Baker, K. S., and R. Frouin (1987), Relation between photosynthetically available radiation and total insolation at the ocean surface under clear skies, *Limnology and Oceanography*, *32*(6), 1370–1377, doi:10.4319/lo.1987.32.6.1370.

Basit, A. (2020), Upwelling and related processes in the Banda and northern Arafura Seas, Ph.D. thesis, University of Hamburg.

Bjørrisen, P. K. (1988), Phytoplankton exudation of organic matter: Why do healthy cells do it?, *Limnology and Oceanography*, *33*(1), 151–154, doi:10.4319/lo.1988.33.1.0151.

Boyer, T. P., O. K. Baranova, C. Coleman, H. E. Garcia, A. Grodsky, R. A. Locarnini, A. V. Mishonov, C. R. Paver, J. R. Reagan, D. Seidov, et al. (2018), NOAA Atlas NESDIS 87, *World Ocean Database*.

Burford, M., and P. Rothlisberg (1999), Factors limiting phytoplankton production in a tropical continental shelf ecosystem, *Estuarine, Coastal and Shelf Science*, *48*(5), 541–549, doi:10.1006/ecss.1999.0471.

Burger, J. M., C. L. Moloney, D. R. Walker, R. G. Parrott, and S. E. Fawcett (2020), Drivers of short-term variability in phytoplankton production in an embayment of the southern Benguela upwelling system, *Journal of Marine Systems*, *208*, 103341, doi:10.1016/j.jmarsys.2020.103341.

Butenschön, M., J. Clark, J. N. Aldridge, J. I. Allen, Y. Artioli, J. Blackford, J. Bruggeman, P. Cazenave, S. Ciavatta, S. Kay, G. Lessin, S. van Leeuwen, J. van der Molen, L. de Mora, L. Polimene, S. Sailley, N. Stephens, and R. Torres (2016), ERSEM 15.06: a generic model for marine biogeochemistry and the

ecosystem dynamics of the lower trophic levels, *Geoscientific Model Development*, *9*(4), 1293–1339, doi:10.5194/gmd-9-1293-2016.

Caldwell, P. C., M. A. Merrifield, and P. R. Thompson (2015), Sea level measured by tide gauges from global oceans — the Joint Archive for Sea Level holdings (NCEI Accession 0019568), Version 5.5, *NOAA National Centers for Environmental Information*, doi:10.7289/V5V40S7W.

Carruthers, T. J., B. J. Longstaff, W. C. Dennison, E. G. Abal, and K. Aioi (2001), Chapter 19 - Measurement of light penetration in relation to seagrass, in *Global Seagrass Research Methods*, edited by F. T. Short and R. G. Coles, p. 369–392, Elsevier Science, Amsterdam, doi:10.1016/B978-044450891-1/50020-7.

Chan, A. T. (1980), Comparative physiological study of marine diatoms and dinoflagellates in relation to irradiance and cell size ii. relationship between photosynthesis, growth, and carbon/chlorophyll a ratio, *Journal of Phycology*, *16*(3), 428–432, doi:10.1111/j.1529-8817.1980.tb03056.x.

Chen, Y.-L. L., H.-Y. Chen, G.-C. Gong, Y.-H. Lin, S. Jan, and M. Takahashi (2004), Phytoplankton production during a summer coastal upwelling in the East China Sea, *Continental Shelf Research*, *24*(12), 1321–1338, doi:10.1016/j.csr.2004.04.002.

Cloern, J. E., C. Grenz, and L. Vidergar-Lucas (1995), An empirical model of the phytoplankton chlorophyll : carbon ratio-the conversion factor between productivity and growth rate, *Limnology and Oceanography*, *40*(7), 1313–1321, doi:10.4319/lo.1995.40.7.1313.

Condie, S. A. (2011), Modeling seasonal circulation, upwelling and tidal mixing in the Arafura and Timor Seas, *Continental Shelf Research*, *31*, 1427–1436, doi:10.1016/j.csr.2011.06.005.

Condie, S. A., and J. R. Dunn (2006), Seasonal characteristics of the surface mixed layer in the Australasian region: Implications for primary production regimes and biogeography, *Marine and Freshwater Research*, *57*(6), 569–590, doi:10.1071/MF06009.

Cullen, J. J., R. Geider, J. Ishizaka, D. Kiefer, J. Marra, E. Sakshaug, and J. Raven (1993), Towards a general description of phytoplankton growth for biogeochemical models, in *Towards a Model of Ocean Biogeochemical Processes*, p. 153–176, Springer.

Darecki, M., and D. Stramski (2004), An evaluation of MODIS and SeaWiFS bio-optical algorithms in the Baltic Sea, *Remote Sensing of Environment*, *89*(3), 326–350, doi:10.1016/j.rse.2003.10.012.

Droop, M. R. (1973), Some thoughts on nutrient limitation in algae, *Journal of Phycology*, *9*(3), 264–272.

Dubinsky, Z., and N. Stambler (2009), Photoacclimation processes in phytoplankton: mechanisms, consequences, and applications, *Aquatic Microbial Ecology*, *56*(2-3), 163–176, doi:10.3354/ame01345.

Duce, R. A., J. LaRoche, K. Altieri, K. R. Arrigo, A. R. Baker, D. G. Capone,

S. Cornell, F. Dentener, J. Galloway, R. S. Ganeshram, R. J. Geider, T. Jickells, M. M. Kuypers, R. Langlois, P. S. Liss, S. M. Liu, J. J. Middelburg, C. M. Moore, S. Nickovic, A. Oschlies, T. Pedersen, J. Prospero, R. Schlitzer, S. Seitzinger, L. L. Sorensen, M. Uematsu, O. Ulloa, M. Voss, B. Ward, and L. Zamora (2008), Impacts of atmospheric anthropogenic nitrogen on the open ocean, *Science*, *320*(5878), 893–897, doi:10.1126/science.1150369.

Egbert, G. D., and S. Y. Erofeeva (2002), Efficient inverse modeling of barotropic ocean tides, *Journal of Atmospheric and Oceanic Technology*, *19*, 183–204, doi:10.1175/1520-0426(2002)019⟨0183:EIMOBO⟩2.0.CO;2.

Estrada, M. (1985), *Deep phytoplankton and chlorophyll maxima in the Western Mediterranean*, p. 247–277, Springer US, Boston, MA, doi:10.1007/978-1-4899-2248-9_12.

Estrada, M., and C. Marrasé (1987), Phytoplankton biomass and productivity off the Namibian Coast, *South African Journal of Marine Science*, *5*(1), 347–356, doi:10.2989/025776187784522234.

Falkowski, P. G., Z. Dubinsky, and K. Wyman (1985), Growth-irradiance relationships in phytoplankton, *Limnology and Oceanography*, *30*(2), 311–321, doi:10.4319/lo.1985.30.2.0311.

Fasham, M. J. R., H. W. Ducklow, and S. M. McKelvie (1990), A nitrogen-based model of plankton dynamics in the oceanic mixed layer, *Journal of Marine Research*, *48*, 591–639, doi:10.1357/002224090784984678.

Fawcett, S., and B. Ward (2011), Phytoplankton succession and nitrogen utilization during the development of an upwelling bloom, *Marine Ecology Progress Series*, *428*, 13–31, doi:10.3354/meps09070.

Ffield, A., and A. L. Gordon (1996), Tidal mixing signatures in the Indonesian Seas, *Journal of Physical Oceanography*, *26*(9), 1924–1937, doi:10.1175/1520-0485(1996)026⟨1924:TMSITI⟩2.0.CO;2.

Fowler, D., C. Flechard, U. Skiba, M. Coyle, and J. N. Cape (1998), The atmospheric budget of oxidized nitrogen and its role in ozone formation and deposition, *The New Phytologist*, *139*, 11–23, doi:10.1046/j.1469-8137.1998.00167.x.

Garcia, H., K. Weathers, C. Paver, I. Smolyar, T. Boyer, R. Locarnini, M. Zweng, A. Mishonov, O. Baranova, D. Seidov, et al. (2018), World Ocean Atlas 2018 volume 4: Dissolved Inorganic Nutrients (phosphate, nitrate and nitrate+ nitrite, silicate), *NOAA Atlas NESDIS*, *84*, 35 pp.

Gieskes, W., G. Kraay, A. Nontji, D. Setiapermana, and Sutomo (1988), Monsoonal alternation of a mixed and a layered structure in the phytoplankton of the euphotic zone of the Banda Sea (Indonesia): A mathematical analysis of algal pigment fingerprints, *Netherlands Journal of Sea Research*, *22*(2), 123–137, doi:10.1016/0077-7579(88)90016-6.

Glibert, P. (1988), Primary productivity and pelagic nitrogen cycling, in *Nitrogen cycling in coastal marine environments*, p. 3–31, John Wiley & Sons Chichester,

UK.

Goldman, J. C. (1977), Temperature effects on phytoplankton growth in continuous culture, *Limnology and Oceanography*, *22*(5), 932–936, doi:10.4319/lo.1977.22.5.0932.

Goldman, J. C., J. J. McCarthy, and D. G. Peavey (1979), Growth rate influence on the chemical composition of phytoplankton in oceanic waters, *Nature*, *279*(5710), 210–215, doi:10.1038/279210a0.

Gordon, A., J. Sprintall, H. V. Aken], D. Susanto, S. Wijffels, R. Molcard, A. Ffield, W. Pranowo, and S. Wirasantosa (2010), The Indonesian throughflow during 2004–2006 as observed by the INSTANT program, *Dynamics of Atmospheres and Oceans*, *50*(2), 115–128, doi:10.1016/j.dynatmoce.2009.12.002, modeling and Observing the indonesian Throughflow.

Gordon, A. L., and R. A. Fine (1996), Pathways of water between the Pacific and Indian oceans in the Indonesian seas, *Letters to Nature*, *379*, 146–149, doi:10.1038/379146a0.

Gordon, A. L., and R. D. Susanto (2001), Banda Sea surface-layer divergence, *Ocean Dynamics*, *52*(1), 2–10, doi:10.1007/s10236-001-8172-6.

Große, F., M. Kreus, H.-J. Lenhart, J. Pätsch, and T. Pohlmann (2017), A novel modeling approach to quantify the influence of nitrogen inputs on the oxygen dynamics of the North Sea, *Frontiers in Marine Science*, *4*, 383, doi:10.3389/fmars.2017.00383.

Große, F., M. Kreus, H. Lenhart, I. Lorkowski, and J. Pätsch (2018), *ECOHAM5 user guide*, University of Hamburg.

Haney, J. D., and G. A. Jackson (1996), Modeling phytoplankton growth rates, *Journal of Plankton Research*, *18*(1), 63–85, doi:10.1093/plankt/18.1.63.

Hegglin, M., D. Kinnison, and J.-F. Lamarque (2016), CCMI nitrogen surface fluxes in support of CMIP6 - version 2.0, doi:10.22033/ESGF/input4MIPs.1125.

Hense, I. (2018), Lecture notes version 1.6 in Introduction to Marine Ecosystem Modelling, Institute for Hydrobiology and Fisheries Science, University of Hamburg.

Hernández-Carrasco, I., V. Rossi, E. Hernández-García, V. Garçon, and C. López (2014), The reduction of plankton biomass induced by mesoscale stirring: A modeling study in the Benguela upwelling, *Deep Sea Research Part I: Oceanographic Research Papers*, *83*, 65–80, doi:10.1016/j.dsr.2013.09.003.

Holt, J., J. Harle, R. Proctor, S. Michel, M. Ashworth, C. Batstone, I. Allen, R. Holmes, T. Smyth, K. Haines, D. Bretherton, and G. Smith (2009), Modelling the global coastal ocean, *Philosophical Transactions of the Royal Society A: Mathematical, Physical and Engineering Sciences*, *367*(1890), 939–951, doi:10.1098/rsta.2008.0210.

Huisman, J., and B. Sommeijer (2002), Maximal sustainable sinking velocity

of phytoplankton, *Marine Ecology Progress Series*, *244*, 39–48, doi:10.3354/meps244039.

Hunger, M., and P. Döll (2008), Value of river discharge data for global-scale hydrological modeling, *Hydrology and Earth System Sciences*, *12*, 841–861, doi:10.5194/hess-12-841-2008.

Ilahude, A., Komar, and Mardanis (1990), On the hydrology and productivity of the northern Arafura Sea, *Netherlands Journal of Sea Research*, *25*(4), 573–583, doi:10.1016/0077-7579(90)90079-V.

Ittekkot, V. (1988), Global trends in the nature of organic matter in river suspensions, *Nature*, *332*(6163), 436–438, doi:10.1038/332436a0.

Johnson, K. A., and R. S. Goody (2011), The original Michaelis constant: Translation of the 1913 Michaelis–Menten paper, *Biochemistry*, *50*(39), 8264–8269, doi:10.1021/bi201284u.

Kalnay, E., et al. (1996), The NCEP/NCAR 40-year reanalysis project, *Bulletin of the American Meteorological Society*, *77*, 437–470, doi:10.1175/1520-0477(1996)077⟨0437:TNYRP⟩2.0.CO;2.

Kida, S., and K. J. Richards (2009), Seasonal sea surface temperature variability in the Indonesian Seas, *Journal of Geophysical Research: Oceans*, *114*(C6), doi:10.1029/2008JC005150.

Kinkade, C., J. Marra, C. Langdon, C. Knudson, and A. G. Ilahudet (1997), Monsoonal differences in phytoplankton biomass and production in the Indonesian Seas: Tracing vertical mixing using temperature, *Deep Sea Research Part I: Oceanographic Research Papers*, *44*(4), 581–592, doi:10.1016/S0967-0637(97)00002-2.

Kiørboe, T., K. Andersen, and H. Dam (1990), Coagulation efficiency and aggregate formation in marine phytoplankton, *Marine Biology*, *107*(2), 235–245, doi:10.1007/BF01319822.

Kirk, J. T. (1994), *Light and photosynthesis in aquatic ecosystems*, Cambridge university press.

Kriest, I., and G. T. Evans (1999), Representing phytoplankton aggregates in biogeochemical models, *Deep Sea Research Part I: Oceanographic Research Papers*, *46*(11), 1841–1859, doi:10.1016/S0967-0637(99)00032-1.

Kämpf, J. (2015), Undercurrent-driven upwelling in the northwestern Arafura Sea, *Geophysical Research Letters*, *42*, 9362–68, doi:10.1002/2015GL066163.

Kämpf, J. (2016), On the majestic seasonal upwelling system of the Arafura Sea, *Journal of Geophysical Research: Oceans*, *121*, 1218–1228, doi:10.1002/2015JC011197.

Kühn, W., and G. Radach (1997), A one-dimensional physical–biological model study of the pelagic nitrogen cycling during the spring bloom in the northern North Sea (FLEX '76), *Journal of Marine Research*, *55*, 687–734, doi:10.1357/

0022240973224229.

Lah, N. Z. A., M. N. M. Reba, and E. Siswanto (2014), An improved MODIS standard chlorophyll-a algorithm for Malacca Straits Water, *IOP Conference Series: Earth and Environmental Science*, *18*, 012113, doi:10.1088/1755-1315/18/1/012113.

Lalli, C., and T. R. Parsons (1997), *Biological oceanography: an introduction*, Elsevier.

Lee, Z., A. Weidemann, J. Kindle, R. Arnone, K. L. Carder, and C. Davis (2007), Euphotic zone depth: Its derivation and implication to ocean-color remote sensing, *Journal of Geophysical Research: Oceans*, *112*(C3), doi:10.1029/2006JC003802.

Li, G., Q. Lin, G. Ni, P. Shen, Y. Fan, L. Huang, and Y. Tan (2012), Vertical patterns of early summer chlorophyll a concentration in the Indian Ocean with special reference to the variation of deep chlorophyll maximum, *Journal of Marine Biology*, *2012*, doi:10.1155/2012/801248.

Liang, L., H. Xue, and Y. Shu (2019), The Indonesian Throughflow and the circulation in the Banda Sea: A modeling study, *Journal of Geophysical Research: Oceans*, *124*(5), 3089–3106, doi:10.1029/2018JC014926.

Liu, F. (2016), Assessment of the effect of SPM variations on the phytoplankton dynamics in the Bohai Sea, Ph.D. thesis, University of Hamburg.

Lorkowski, I., J. Pätsch, A. Moll, and W. Kühn (2012), Interannual variability of carbon fluxes in the North Sea from 1970 to 2006: Competing effects of abiotic and biotic drivers on the gas-exchange of CO2, *Estuarine, Coastal and Shelf Science*, *100*, 38–57, doi:10.1016/j.ecss.2011.11.037.

Luhtala, H., H. Tolvanen, and R. Kalliola (2013), Annual spatio-temporal variation of the euphotic depth in the SW-Finnish archipelago, Baltic Sea, *Oceanologia*, *55*(2), 359–373, doi:10.5697/oc.55-2.359.

Ma, L., W. Xiao, E. A. Laws, X. Bai, K.-P. Chiang, X. Liu, J. Chen, and B. Huang (2021), Responses of phytoplankton communities to the effect of internal wave-powered upwelling, *Limnology and Oceanography*, *66*(4), 1083–1098, doi:10.1002/lno.11666.

Mackey, K. R. M., G. L. van Dijken, S. Mazloom, A. M. Erhardt, J. Ryan, K. R. Arrigo, and A. Paytan (2010), Influence of atmospheric nutrients on primary productivity in a coastal upwelling region, *Global Biogeochemical Cycles*, *24*(4), doi:10.1029/2009GB003737.

Manzer, C. R., T. P. Connolly, E. McPhee-Shaw, and G. J. Smith (2019), Physical factors influencing phytoplankton abundance in southern Monterey Bay, *Continental Shelf Research*, *180*, 1–13, doi:10.1016/j.csr.2019.04.007.

Marsland, S. J., H. Haak, J. H. Jungclaus, M. Latif, and F. Röske (2003), The Max Planck Institute global ocean/sea ice model with orthogonal curvilinear coordinates, *Ocean Modell.*, *5*, 91–127, doi:10.1016/S1463-5003(02)00015-X.

Mayer, B., and P. E. Damm (2012), The Makassar Strait throughflow and its jet,

Journal of Geophysical Research: Oceans, *117*(C7), doi:10.1029/2011JC007809.

Mayer, B., T. Rixen, and T. Pohlmann (2018), The spatial and temporal variability of air-sea CO2 fluxes and the effect of net coral reef calcification in the Indonesian seas: A numerical sensitivity study, *Frontiers in Marine Science*, *5*, 116, doi:10.3389/fmars.2018.00116.

Mayorga, E., S. P. Seitzinger, J. A. Harrison, E. Dumont, A. H. Beusen, A. F. Bouwman, B. M. Fekete, C. Kroeze, and G. V. Drecht (2010), Global nutrient export from WaterSheds 2 (NEWS 2): Model development and implementation, *Environmental Modelling and Software*, *25*, 837–853, doi:10.1016/j.envsoft.2010.01.007.

McCave, I. (1984), Size spectra and aggregation of suspended particles in the deep ocean, *Deep Sea Research Part A. Oceanographic Research Papers*, *31*(4), 329–352, doi:10.1016/0198-0149(84)90088-8.

McCree, K. (1972), Test of current definitions of photosynthetically active radiation against leaf photosynthesis data, *Agricultural Meteorology*, *10*, 443–453, doi:10.1016/0002-1571(72)90045-3.

Mignot, A., H. Claustre, J. Uitz, A. Poteau, F. D'Ortenzio, and X. Xing (2014), Understanding the seasonal dynamics of phytoplankton biomass and the deep chlorophyll maximum in oligotrophic environments: A Bio-Argo float investigation, *Global Biogeochemical Cycles*, *28*(8), 856–876, doi:10.1002/2013GB004781.

Milliman, J. D., K. L. Farnsworth, and C. S. Albertin (1999), Flux and fate of fluvial sediments leaving large islands in the East Indies, *Journal of Sea Research*, *41*(1), 97–107, doi:10.1016/S1385-1101(98)00040-9.

Moll, A. (1998), Regional distribution of primary production in the North Sea simulated by a three-dimensional model, *Journal of Marine Systems*, *16*, 151–170, doi:10.1016/S0924-7963(97)00104-8.

Moore, C. M., D. J. Suggett, A. E. Hickman, Y.-N. Kim, J. F. Tweddle, J. Sharples, R. J. Geider, and P. M. Holligan (2006), Phytoplankton photoacclimation and photoadaptation in response to environmental gradients in a shelf sea, *Limnology and Oceanography*, *51*(2), 936–949, doi:10.4319/lo.2006.51.2.0936.

Morel, A., and L. Prieur (1977), Analysis of variations in ocean color, *Limnology and oceanography*, *22*(4), 709–722, doi:10.4319/lo.1977.22.4.0709.

NASA Goddard Space Flight Center, O. B. P. G. (2014), MODIS Ocean Color Data, NASA OB.DAAC, Greenbelt, MD, USA.

Ning, X., F. Chai, H. Xue, Y. Cai, C. Liu, and J. Shi (2004), Physical-biological oceanographic coupling influencing phytoplankton and primary production in the South China Sea, *Journal of Geophysical Research: Oceans*, *109*(C10), doi:10.1029/2004JC002365.

Pei, S., T. Shinoda, J. Steffen, and H. Seo (2021), Substantial sea surface temperature cooling in the Banda Sea associated with the Madden-Julian Oscillation in the boreal winter of 2015, *Journal of Geophysical Research: Oceans*, *126*(6),

e2021JC017226, doi:10.1029/2021JC017226.

Pitcher, G., D. Walker, B. Mitchell-Innes, and C. Moloney (1991), Short-term variability during an anchor station study in the southern Benguela upwelling system: Phytoplankton dynamics, *Progress in Oceanography*, *28*(1), 39–64, doi:10.1016/0079-6611(91)90020-M.

Pohlmann, T. (1996), Predicting the thermocline in a circulation model of the North Sea, part 1: Model description, calibration and verification, *Continental Shelf Research*, *16*, 131–146, doi:10.1016/0278-4343(95)90885-S.

Prowe, A., H. Thomas, J. Pätsch, W. Kühn, Y. Bozec, L.-S. Schiettecatte, A. V. Borges, and H. J. de Baar (2009), Mechanisms controlling the air–sea CO2 flux in the North Sea, *Continental Shelf Research*, *29*(15), 1801–1808, doi:10.1016/j.csr.2009.06.003.

Putri, M. R. (2005), Study of ocean climate variability (1959-2002) in the eastern Indian Ocean, Java Sea, and Sunda Strait using the HAMburg Shelf Ocean Model, Ph.D. thesis, University of Hamburg.

Pätsch, J., and W. Kühn (2008), Nitrogen and carbon cycling in the North Sea and exchange with the North Atlantic—A model study. Part I. Nitrogen budget and fluxes, *Continental Shelf Research*, *28*(6), 767–787, doi:10.1016/j.csr.2007.12.013.

Pätsch, J., W. Kühn, G. Radach, J. Santana Casiano, M. Gonzalez Davila, S. Neuer, T. Freudenthal, and O. Llinas (2001), Interannual variability of carbon fluxes at the North Atlantic Station ESTOC, *Deep Sea Research Part II: Topical Studies in Oceanography*, *49*(1), 253–288, doi:10.1016/S0967-0645(01)00103-5.

Pätsch, J., W. Kühn, and K. D. Six (2018), Interannual sedimentary effluxes of alkalinity in the southern North Sea model results compared with summer observations, *Biogeosciences*, *15*, 3293–3309, doi:10.5194/bg-15-3293-2018.

Riemann, B., P. Simonsen, and L. Stensgaard (1989), The carbon and chlorophyll content of phytoplankton from various nutrient regimes, *Journal of Plankton Research*, *11*(5), 1037–1045, doi:10.1093/plankt/11.5.1037.

Robertson, R., and A. Ffield (2008), Baroclinic tides in the Indonesian seas: Tidal fields and comparisons to observations, *Journal of Geophysical Research: Oceans*, *113*(C7), doi:10.1029/2007JC004677.

Rothlisberg, P. C., P. C. Pollard, P. D. Nichols, D. J. W. Moriarty, A. M. G. Forbes, C. J. Jackson, and D. Vaudrey (1994), Phytoplankton community structure and productivity in relation to the hydrological regime of the Gulf of Carpentaria, Australia, in summer, *Marine and Freshwater Research*, *45*(3), 265–282, doi:10.1071/MF9940265.

Salamena, G. G., J. C. Whinney, S. F. Heron, and P. V. Ridd (2021), Internal tidal waves and deep-water renewal in a tropical fjord: Lessons from Ambon Bay, eastern Indonesia, *Estuarine, Coastal and Shelf Science*, *253*, 107291, doi:10.1016/j.ecss.2021.107291.

Salciccioli, J., Y. Crutain, M. Komorowski, and D. Marshall (2016), *Sensitivity*

analysis and model validation, pp. 263–271, doi:10.1007/978-3-319-43742-2_17.

Sathyendranath, S., et al. (2000), Remote sensing of ocean colour in coastal, and other optically-complex, waters, *Tech. rep.*

Sellar, A. A., J. Walton, C. G. Jones, R. Wood, N. L. Abraham, M. Andrejczuk, M. B. Andrews, T. Andrews, A. T. Archibald, L. de Mora, H. Dyson, M. Elkington, R. Ellis, P. Florek, P. Good, L. Gohar, S. Haddad, S. C. Hardiman, E. Hogan, A. Iwi, C. D. Jones, B. Johnson, D. I. Kelley, J. Kettleborough, J. R. Knight, M. O. Köhler, T. Kuhlbrodt, S. Liddicoat, I. Linova-Pavlova, M. S. Mizielinski, O. Morgenstern, J. Mulcahy, E. Neininger, F. M. O'Connor, R. Petrie, J. Ridley, J.-C. Rioual, M. Roberts, E. Robertson, S. Rumbold, J. Seddon, H. Shepherd, S. Shim, A. Stephens, J. C. Teixiera, Y. Tang, J. Williams, A. Wiltshire, and P. T. Griffiths (2020), Implementation of U.K. Earth System Models for CMIP6, *Journal of Advances in Modeling Earth Systems*, *12*(4), e2019MS001946, doi:10.1029/2019MS001946, e2019MS001946 10.1029/2019MS001946.

Sherman, E., J. K. Moore, F. Primeau, and D. Tanouye (2016), Temperature influence on phytoplankton community growth rates, *Global Biogeochemical Cycles*, *30*(4), 550–559, doi:10.1002/2015GB005272.

Sigman, D. M., and M. P. Hain (2012), The biological productivity of the ocean, *Nature Education Knowledge*, *3*, 1–16.

Soetaert, K., and P. M. Herman (2008), *A practical guide to ecological modelling: using R as a simulation platform*, Springer Science & Business Media.

Song, Y., and Y. Chao (2004), A theoretical study of topographic effects on coastal upwelling and cross-shore exchange, *Ocean Modelling*, *6*(2), 151–176, doi:10.1016/S1463-5003(02)00064-1.

Sprintall, J., S. E. Wijffels, R. Molcard, and I. Jaya (2009), Direct estimates of the Indonesian Throughflow entering the Indian Ocean: 2004–2006, *Journal of Geophysical Research: Oceans*, *114*(C7), doi:10.1029/2008JC005257.

Su, J., and T. Pohlmann (2009), Wind and topography influence on an upwelling system at the eastern Hainan coast, *Journal of Geophysical Research: Oceans*, *114*(C6), doi:10.1029/2008JC005018.

Takahashi, M., and T. Hori (1984), Abundance of picophytoplankton in the subsurface chlorophyll maximum layer in subtropical and tropical waters, *Marine biology*, *79*(2), 177–186, doi:10.1007/BF00951826.

Talley, L. D., and J. Sprintall (2005), Deep expression of the Indonesian Throughflow: Indonesian Intermediate Water in the South Equatorial Current, *Journal of Geophysical Research: Oceans*, *110*(C10), doi:10.1029/2004JC002826.

Tan, C. K., J. Ishizaka, S. Matsumura, F. M. Yusoff, and M. I. H. Mohamed (2006), Seasonal variability of SeaWiFS chlorophyll a in the Malacca Straits in relation to Asian monsoon, *Continental Shelf Research*, *26*(2), 168–178, doi:10.1016/j.csr.2005.09.008.

Thingstad, T. F., and F. Rassoulzadegan (1995), Nutrient limitations, microbial

food webs and 'biological C-pumps': suggested interactions in a P-limited Mediterranean, *Marine Ecology Progress Series*, *117*(1/3), 299–306.

Toggweiler, J. (1993), Carbon overconsumption, *Nature*, *363*(6426), 210–211, doi:10.1038/363210a0.

Tuerena, R. E., R. G. Williams, C. Mahaffey, C. Vic, J. A. M. Green, A. Naveira-Garabato, A. Forryan, and J. Sharples (2019), Internal tides drive nutrient fluxes into the deep chlorophyll maximum over mid-ocean ridges, *Global Biogeochemical Cycles*, *33*(8), 995–1009, doi:10.1029/2019GB006214.

Van Andel, T. H., and J. J. Veevers (1965), Submarine morphology of the Sahul Shelf, northwestern Australia, *Geological Society of America Bulletin*, *76*(6), 695–700, doi:10.1130/0016-7606(1965)76[695:SMOTSS]2.0.CO;2.

Varela, R. A., A. Cruzado, J. Tintore, and E. Garda Ladona (1992), Modelling the deep-chlorophyll maximum: a coupled physical-biological approach, *Journal of Marine Research*, *50*(3), 441–463, doi:10.1357/002224092784797638.

Wang, X. J., M. Behrenfeld, R. Le Borgne, R. Murtugudde, and E. Boss (2009), Regulation of phytoplankton carbon to chlorophyll ratio by light, nutrients and temperature in the Equatorial Pacific Ocean: a basin-scale model, *Biogeosciences*, *6*(3), 391–404, doi:10.5194/bg-6-391-2009.

Wasmund, N., G. Nausch, and A. Hansen (2014), Phytoplankton succession in an isolated upwelled Benguela water body in relation to different initial nutrient conditions, *Journal of Marine Systems*, *140*, 163–174, doi:10.1016/j.jmarsys.2014.03.006, upwelling Ecosystem Succession.

Waworuntu, J. M., R. A. Fine, D. B. Olson, and A. L. Gordon (2000), Recipe for Banda Sea water, *Journal of Marine Research*, *58*, 547–569, doi:10.1357/002224000321511016.

Weston, K., L. Fernand, D. K. Mills, R. Delahunty, and J. Brown (2005), Primary production in the deep chlorophyll maximum of the central North Sea, *Journal of Plankton Research*, *27*(9), 909–922, doi:10.1093/plankt/fbi064.

Wetsteyn, F. J., A. G. Ilahude, and M. A. Baars (1990), Nutrient distribution in the upper 300 m of the eastern Banda Sea and northern Arafura Sea during and after the upwelling season, August 1984 and February 1985, *Netherlands Journal of Sea Research*, *25*, 449–464, doi:10.1016/0077-7579(90)90069-S.

Winarso, G., and Y. Marini (2017), MODIS standard (OC3) chlorophyll-a algorithm evaluation in Indonesian seas, *International Journal of Remote Sensing and Earth Sciences (IJReSES)*, *11*(1), 11–20.

Wirasantosa, S., S. Nurhakim, L. Adrianto, D. Nugroho, and C. dos Santos Silva (2011), ATSEA Thematic Reports on the Arafura and Timor Seas Region. Report prepared for the Arafura Timor Seas Ecosystem Action (ATSEA) Program, *techreport*, Agency for Marine and Fisheries Research and Development, Ministry of Marine Affairs and Fisheries, Indonesia, 263ps.

Wirasatriya, A., R. D. Susanto, K. Kunarso, A. R. Jalil, F. Ramdani, and

A. D. Puryajati (2021), Northwest monsoon upwelling within the Indonesian seas, *International Journal of Remote Sensing*, *42*(14), 5433–5454, doi:10.1080/01431161.2021.1918790.

Wolanski, E. (1993), Water circulation in the Gulf of Carpentaria, *Journal of Marine Systems*, *4*, 401–420, doi:10.1016/0924-7963(93)90024-G.

Wyrtki, K. (1961), *Naga report volume 2 scientific results of marine investigation of the South China Sea and the Gulf of Thailand 1959–1961*, The University of California, California.

Zevenboom, W., and F. J. Wetsteyn (1990), Growth limitation and growth rates of (pico)phytoplankton in the Banda Sea during two different monsoons, *Netherlands Journal of Sea Research*, *25*(4), 465–472, doi:10.1016/0077-7579(90)90070-W.

Zhu, Y., L. Wang, Y. Wang, T. Xu, S. Li, G. Cao, Z. Wei, and T. Qu (2019), Stratified circulation in the Banda Sea and its causal mechanism, *Journal of Geophysical Research: Oceans*, *124*(10), 7030–7045, doi:10.1029/2019JC015279.

Zijlstra, J. J., M. A. Baars, F. J. Tijssen, F. J. Wetsteyn, J. I. Witte, and Hadikusumah (1990), Monsoonal effects on the hydrography of the upper waters (<300 m) of the eastern Banda Sea and northern Arafura Sea, with special reference to vertical transport processes, *Netherlands Journal of Sea Research*, *25*, 431–447, doi:10.1016/0077-7579(90)90068-R.

List of Figures

List of Tables

List of Abbreviations

General abbreviations	
CMIP	Coupled Model Intercomparison Project
CTD	Conductivity, Temperature, and Depth
ECOHAM	Ecosystem Model Hamburg
ERSEM	European Regional Seas Ecosystem Model
ETOPO5	Earth topography five-arcminute grid
GCOMS	Global Coastal Ocean Modelling System
GEBCO	General Bathymetric Chart of the Oceans
GlobalNEWS2	Global Nutrient Export from WaterShed2
HAMSOM	Hamburg Shelf Ocean Model
IHO	International Hydrographic Organization
IOC	Intergovernmental Oceanographic Commission
MODIS	Moderate Resolution Imaging Spectroradiometer
MPI-ESM	Max-Planck Institute Earth System Model
MPI-OM	Max-Planck Institute Ocean Model
NCAR	National Center for Atmospheric Research
NCEP	National Centers for Environmental Prediction
RMSE	Root Mean Square Error
UHSLC	University of Hawaii Sea Level Center
WGHM	WaterGAP Global Hydrology Model
WOD18	World Ocean Database 2018
Abbreviations related to biogeochemical and physical processes	
DCM	deep chlorophyll maximum
DIC/DIN/DIP	dissolved inorganic carbon/nitrogen/phosphorus
DOC/DON/DOP	dissolved organic carbon/nitrogen/phosphorus
ITF	Indonesian throughflow
NPP	net primary production
NW	northwest
PAR	photosynthetic available radiation
POC/PON/POP/POS	particulate organic carbon/nitrogen/phosphorus/silica
SE	southeast
SOC	semi-labile dissolved organic carbon
SSH	sea surface height
SST	sea surface temperature

Acknowledgments

Foremost, I would like to thank my supervisor, **PD Dr. Thomas Pohlmann**. I am especially grateful for the opportunity he gave me to accomplish a PhD. Thank you for the advice and constructive suggestions for my work. Finally, thank you for helping me to broaden my scientific knowledge.

I would like to express my sincere gratitude to my co-supervisor, **Dr. Johannes Pätsch**, for the time and scientific guidance during my study. Thank you for patiently teaching me how to run the ECOHAM and be there whenever I need help. Thank you for your support, advice, and helpful corrections to my PhD project.

I am thankful to **Dr. Rolf Koppelmann** for being my panel chair. Thank you for the advice and fascinating discussions we had during our advisory meetings. I would also like to thank the **SICSS** graduate school for organizing different courses, workshops, and retreats. It was a pleasure to be a part of the SICSS family.

I would also like to thank **Dr. Bernhard Mayer** and **Dr. Abdul Basit** for helping me, especially with the HAMSOM setup and model input data. Many thanks also to **Dr. Susan Kay** from Plymouth Marine Laboratory for providing the biogeochemical dataset.

My sincere gratitude to the **Deutsches Akademischer Austauschdienst (DAAD)** for providing the scholarship that allowed this doctorate to be possible in the first place. I would also like to acknowledge the **Das Deutsche Klimarechenzentrum (DKRZ)** for providing the computational resources and helping me with technical problems with the model.

To my dearest friend, **Ceren**, thank you for your support and encouragement. During your stay in Hamburg, I had a great time. I miss our afternoon routine; drinking tea and eating börek in our favorite bakery. I am very grateful to have you as my office mate. I would also send my gratitude to **Mark** for patiently proofreading my thesis. Thank you for all your helpful suggestions for my writing. Many thanks also to **Lea** for helping with the German translation.

To my beloved **Indonesian Muslim community** in Hamburg, thank you very much. Ever since I set foot in Hamburg, you welcomed me with a warm hug. I am always looking forward to our bi-weekly agenda. I know that no matter how bad my day goes, meeting with you always brightens my day up. Special thanks also to **Betty Na** for helping me during my early days in Hamburg.

My sincere thanks go to **Dr. Mutiara Rachmat Putri**, my supervisor during my bachelor's and master's studies at ITB (Bandung Institute of Technology). You

are my inspiration to study in Germany and the one who motivates me to pursue a PhD. Many thanks also to all members of **the Research Group of Oceanography, ITB**. Thank you for your support from the very beginning, ever since my scholarship application until now.

Lastly, I would like to thank **my family** for their everlasting love and support. To **my husband**, thank you for always believing in me, always comforting me whenever I am feeling down. I am forever grateful to have you by my side through all the highs and lows (those especially) during this journey.

Thank you!

Affirmation on Oath

Deutsch

Hiermit erkläre ich an Eides statt, dass ich die vorliegende Dissertationsschrift selbts verfasst und keine anderen als die angegebenen Quellen und Hilfsmittel benutzt habe.

English

I hereby declare upon oath that I have written the present dissertation independently and have not used further resources and aids than those stated.

Hamburg, 11 October 2021

Suliskania Nurfitri